The Physics of Cellulose Biosynthesis

Polymerization and Self-Organization, from plants to bacteria

Promotoren:	prof.dr. B.M. Mulder hoogleraar Theoretische celfysica
	prof.dr. A.M.C. Emons hoogleraar plantencelbiologie
Promotiecommissie:	prof.dr. R.M. Brown Jr. (University of Texas, Austin, USA) prof.dr. J.-F. Joanny (Institut Curie, Paris, France) dr. D.P. Lowe (Universiteit van Amsterdam) prof.dr. J.M. Molenaar (Wageningen Universiteit)

Dit onderzoek is uitgevoerd binnen de onderzoeksschool EPS (Experimental Plant Sciences).

The Physics of Cellulose Biosynthesis

Polymerization and Self-Organization, from plants to bacteria

Proefschrift

ter verkrijging van de graad van doctor
op gezag van de rector magnificus
van Wageningen Universiteit
Prof.dr. M. J. Kropff
in het openbaar te verdedigen
op vrijdag 26 oktober 2007
des namiddags te 13.30 uur in de Aula

ISBN 978-90-8504-719-3

Ai miei nonni

“Amico mio
permetti una domanda
sai gia’ che io
domani parto per l’Olanda...”

Banalita’, Daniele Silvestri

Contents

1 Prologue

"Why study cellulose, why is it important? "
I think that this question perfectly summarizes what most of you must have thought reading the title of this thesis. And, probably, it is the same thing I wondered the moment I was offered a PhD position on this subject. What I can tell you for sure is that now, after four years of research on this theme, I realize how fundamental is the role of this biopolymer in nature, and how beautiful are the several mysteries still shrouded around it.

The topics I shall discuss in this thesis, though being related, are quite different. For this reason, I have structured the present work so that each chapter has its own introductory section, and can be read independently from the others. As a bonus for the reader, I have decided to start with a discussion on some general aspects of cellulose, setting up a comprehensive framework that allows an easier reading of the following chapters.

Let's start saying that, if you think about it carefully, it is easy to understand that cellulose is all around us: we wear it, eat it, build with it, print on it, burn it. But yet, who even thinks about it, or knows what it is?

2 Introduction

2.1 What is cellulose?

Cellulose is the most abundant macromolecule on earth (1), with an estimated 180 billion tons produced annually. A great deal of the world's economy depends directly upon it: this polysaccharide is the major constituent of cotton (over 94%) and wood (over 50%), which together are the basic resources for all cellulose-based products such as paper, textiles, construction materials, as well as such cellulose derivatives as cellophane and rayon.

Chemically, cellulose appears simple: it is a linear polymer of β-(1,4) glucose, where every two adjacent glucose molecules are linked together in opposite orientations (Fig. 2.1a). Cellobiose, which consists of a pair of glucose residues rotated of 180° with respect to each other, is thus the repeating structural unit of cellulose. The linkage pattern and the flat conformation of the glucan rings confer a ribbon-like shape and semi-rigid properties to the polymer, and this particular molecular structure enables the cellulose molecules to crystallize into rigid rods called microfibrils (CMFs) (Fig. 2.1b). This crystalline, microfibrillar form, allows cellulose to play its structural role in nature.

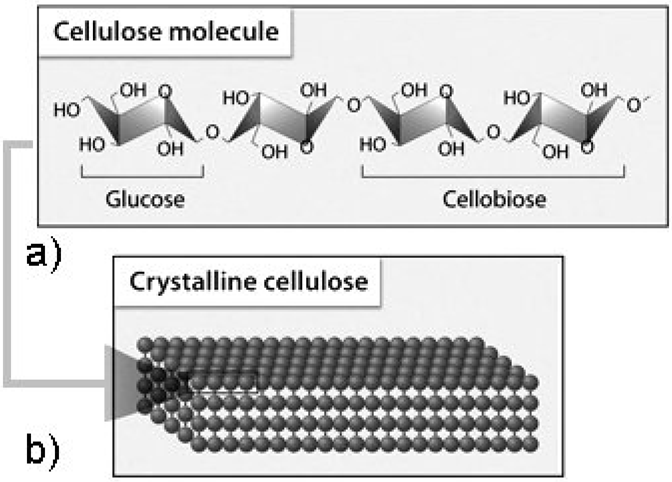

Figure 2.1: a) Chemical structure of a single cellulose chain. b) Crystalline cellulose microfibril (CMF)

Most of the cellulose is made by vascular plants, but its synthesis also occurs in the algae, in the slime mold Dictyostelium, in a number of bacterial species, and in tunicates in the animal kingdom. Photosynthetic microbes, the first in the vast food chain, also represent an important resource for cellulose production in nature: without these organisms all animal life in the oceans would cease to exist. Land plants assemble cellulose from glucose, which is created in the living plant cell through photosynthesis. In the oceans, most of the cellulose is produced by unicellular plankton or algae using the same type of carbon dioxide fixation found in the photosynthesis of vascular plants.

2.2 Different types of cellulose

Cellulose is a remarkable structure, and depending on the sources from which it is obtained, its physical properties, such as the degree of crystallinity and the molecular weight, may be highly variable. There are crystalline and noncrystalline forms of cellulose: the first one is characterized by a tensile strength greater than steel, and it can be found as cellulose I or cellulose II (Fig. 2.2). Both of these two allomorphs can be directly synthesized in nature; however, cellulose I is by far the most prevalent, and no eukaryotic cells are known to abundantly synthesize cellulose II in vivo. Surprisingly, the cellulose I allomorph is a thermodynamically metastable form (2), and can be converted directly to cellulose II with treatment of a high concentration of sodium hydroxide (NaOH), a process called mercerization; however, cellulose II cannot be directly converted to cellulose I.

- Cellulose I
  In nature, and in most of all plants, cellulose is generally produced as crystalline cellulose I (Fig. 2.2a/c and Fig. 2.3b), in which the glucan chains are parallel to each other (3; 4) and are packed side by side to form CMFs that are typically 3nm thick, but which can reach widths of 60nm in certain algae. There are two known suballomorphs of cellulose I: Ia and Ib (5; 6). These two forms differ with respect to their molecular conformation, hydrogen bonding and crystal packing, but can usually coexist together within a given CMF, whose physical properties will be dependent on the ratio of these two suballomorphs. Cellulose from some algae and bacteria is found to be Ia rich, while cellulose from cotton wood is Ib rich (7). The tunicates, the only animal to produce cellulose (8), appear to synthesize almost exclusively cellulose Ib.

- Cellulose II
  A few organisms produce crystalline cellulose II (Fig. 2.2b/d) naturally. This form is generally synthesized by mutants of Acetobacter Xylinum (9), a bacterium that normally produces cellulose I. The glucan chains arrangement in cellulose II has been proposed to be antiparallel (Fig. 2.3c), and this disposition may take place as a result of chain folding during synthesis (9). An additional hydrogen bond per glucan chain residue in cellulose II makes this allomorph be the most thermodynamically stable form. Cellulose I which has undergone mercerization is cellulose II: however, chain folding has not been demonstrated in this type of cellulose II. Understanding the structure of cellulose II derived from mercerized products is one of the remaining issue about cellulose structure to be elucidated.

- Non-crystalline cellulose
  Apart from the crystalline states, cellulose also occurs in non-crystalline states, and

this form has been observed to be present along with the cellulose I crystallites in some CMFs. A new form of derived cellulose, referred to as nematic ordered cellulose (NOC), is obtained by dissolving native cellulose and reprecipitating it in a unique manner to form a distinctive structure (10) highly ordered yet not crystalline: films obtained from this type of cellulose exhibit properties different from conventional cellulose films. In the majority of cases, cellulose modified after synthesis has properties not found in the native cellulose that is obtained from living organisms.

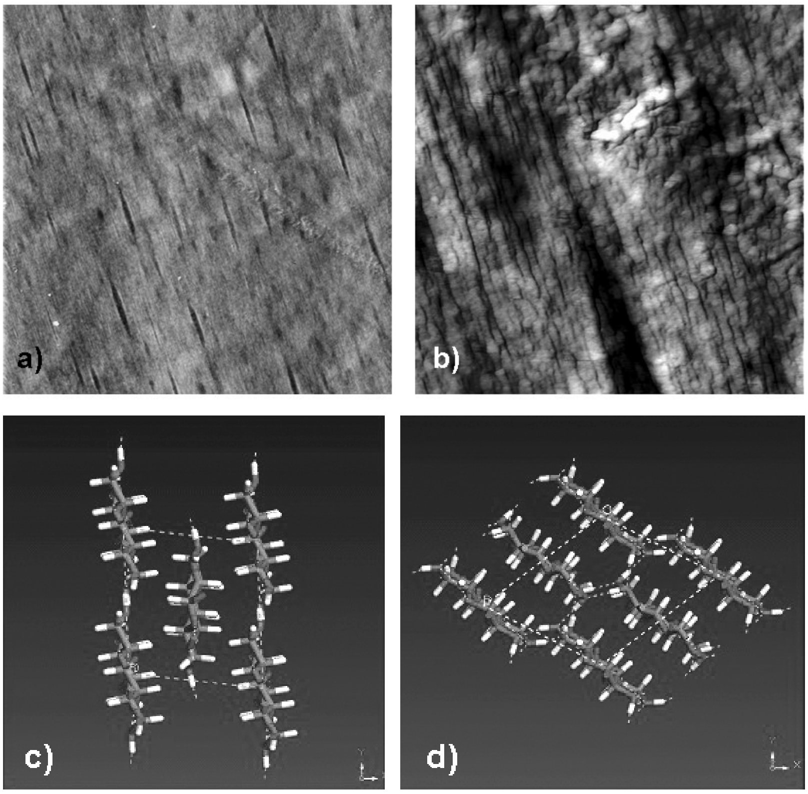

Figure 2.2: Images of (a) cellulose I and (b) cellulose II specimen. Projections of the 3d structure of (c) cellulose Ib and (d) cellulose II

2.3 Biogenesis of Cellulose I

As mentioned in the previous section, the most common natural allomorph of cellulose is cellulose I. Since in this thesis we will be mostly concerned with this type of cellulose, in the following we recall the basic concepts related to the biogenesis of this polymer.

Cellulose I consists of crystalline CMFs in which the glucan chains are parallel and extended. The substrate for cellulose synthesis is UDP-glucose, which is channeled through the cellulose synthase complex (CSC) and transformed into linear chains of glucose residues (see Chapter 4 for details). The CSCs are multiparticulate enzymes, that are usually found in the membranes of cells (plants, algae and bacteria), and which contain a number of catalytic sites each putatively polymerizing a single glucan chain. Surveying all the different type of existing CSCs in nature (see Chapter 3 for details), it is believed that the mechanism of polymerization is conserved in all these enzymes: cellulose is synthesized processively, with the growing end of the glucan chain (the non-reducing end) tightly associated with the catalytic region of the CSC.

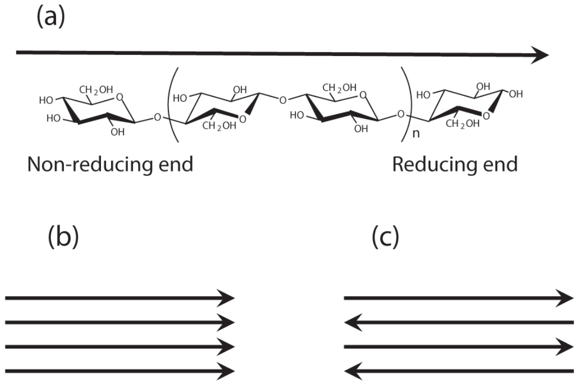

Figure 2.3: b) Parallel and c) antiparallel arrangement of a) cellulose chains

This description indicates that there are two main levels of organization of cellulose (11): first, glucose molecules have to be synthesized and linked into a long chain (polymerization); second, many cellulose polymers coalesce together to form the CMF (crystallization). The size, shape and degree of crystalline perfection is largely due to the geometrical positioning of the catalytic sites within the enzyme complex (see Chapter 3 and Chapter 4 for details). Because of these hierarchical levels of cellulose organization, it is most appropriate to refer to cellulose biogenesis rather than simply biosynthesis.

2.3.1 Polymerization and Crystallization

Recently, a lot of work has been done in order to produce the in vitro synthesis of cellulose I. One of the reasons that have made these experiments so intriguing and so difficult, is that cellulose I is only a metastable state (2): thus, in vitro systems must be mimicking in some way the conditions favoured not only for β-(1,4) linked polymerization, but also for crystallization into a less stable state. Cellulose biogenesis is a hierarchical process, with polymerization and crystallization being two distinct, but not completely separated, events (11), linked in such a way to influence each other: the parallel arrangement of the glucan chains in the CMF requires in fact the newly synthesized polymers to align with each other and lock into a specific crystal structure (cellulose I), otherwise they would fold into the more thermodynamically stable cellulose II, or simply exist as non-crystalline cellulose. The coordinated synthesis of a large number of glucan chains from ordered sites present in the CSC, allows these polymers to be positioned adjacent to each other before they crystallize.

The main proof that polymerization and crystallization are coupled processes in cellulose biogenesis comes from studies on Acetobacter Xylinum: in this cellulose producing bacterium, it has been seen that an optical brightener, Calcofluor White ST (11), inhibits the crystallization preventing the formation of the cellulose CMFs. Interestingly enough, this results in an increase in the rate of cellulose polymerization by an amount that varies between 2 and 4 times the control rate. This could indicate that the time required for the glucan chains to crystallize limits the rate at which polymerization proceeds. In any case, it demonstrates a clear inter-dependence between these two processes.

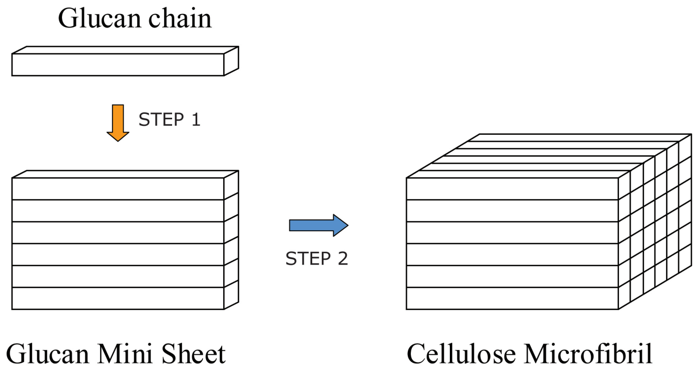

Figure 2.4: Scheme for the two-step crystallization process of the CMF: first, glucan chain coalesce in a monomolecular layer via Van der Waals forces; then the glucan sheets crystallize together through Hydrogen bonding to form a CMF.

Even if crystallization occurs soon after the glucan chains have been extruded from the cell, it does not happen instantaneously: the glucan chains in fact are able to form ordered (but non-crystalline) bundles, by binding to external agents after synthesis, suggesting stages in the process of crystallization itself (12). Based on studies with A. Xylinum and incorporating results from molecular modelling, Cousins and Brown (13; 14) have proposed a two-step model for cellulose I crystallization (Fig. 2.4): first, glucan chains assemble as a monomolecular glucan chain sheet using Van der Waals forces; secondly, the short-lived glucan sheets associates with adjacent sheets via H-bonding to produce the crystalline cellulose I CMF.

The formation of glucan chain sheets as primary event in microfibril formation is experimentally supported by the fact that, as already remarked, in vivo assembly of cellulose in A. Xylinum can be interrupted by the addition of Calcofluor White (12): this dye has a preferential affinity for H-bonding to the glucan sheets, and, once bound to them, it prevents the induction of the second stage of cellulose crystallization to form the cellulose I CMF.

2.4 The role of cellulose in Nature

Now that we know something more about the structure and biogenesis of cellulose, we can start focusing on the role that this polymer plays in nature. Cellulose is not only an essential product for our everyday life, being the major constituent of paper, wood, and textiles. As we will learn in this section, in fact, this biopolymer serves a more fundamental function, since it is one of the major storage point of solar energy and atmospheric CO2 in organic form that we can use.

Let's start from the beginning: as previously said in this chapter, cellulose is made up of glucose, which is a primary product of photosynthesis. This process, that can be illustrated as follows

$$6H_2O + 6CO_2 + \text{light energy} \longrightarrow C_6H_{12}O_6 + 6O_2$$

essentially converts light energy in chemical energy, producing a molecule of glucose plus six of oxygen starting from water, carbon dioxide (CO2), and light. Through the process of photosynthesis, green plants absorb solar energy and remove CO2 from the atmosphere to produce sugars. Plants and animals burn these carbohydrates (and other products derived from them) through respiration, the reverse of photosynthesis, a process that releases the energy contained in sugars for use in metabolism, and renders the carbohydrate fuel back to carbon dioxide. Together, respiration and decomposition (respiration that consumes organic matter mostly by bacteria and fungi) return the biologically fixed carbon back to the atmosphere. This vast interplay between the CO2 of the atmosphere and its "fixation" via photosynthesis into organic products, among which cellulose is the most abundant, is called “carbon cycle”(Fig. 2.5).

In addition to the natural fluxes of carbon through the Earth system, human activities, particularly fossil fuel burning and deforestation, are also releasing carbon dioxide into the atmosphere. When we mine coal and extract oil from the Earth's crust, and then burn these fossil fuels for transportation, heating, cooking, electricity, and manufacturing, we are effectively moving carbon more rapidly into the atmosphere than is being removed naturally through the sedimentation of carbon, ultimately causing the concentration of atmospheric CO2 to increase. Moreover, by clearing forests to support agriculture, we are transferring carbon from living biomass into the atmosphere (dry wood is about 50 percent carbon). The result is that humans are adding ever-increasing amounts of extra carbon dioxide into the atmosphere. Because of this, atmospheric CO2 concentrations are higher today than they have been over the last half-million years or longer. This emerging problem could have immense consequences if the CO2 content continues to rise: the global warming cycle, affected by the emergence of the industrial age, is in fact closely related to this issue.

In this context, the role of cellulose within the global carbon cycle is fundamental: cellulose can be thought of as a giant carbon "sink" that fixes the atmospheric CO2 in organic form. Most of the organic compounds that are formed as a result of CO2 fixation in the bodies of photosynthetic organisms are ultimately broken down and released back into the atmosphere or water. However, certain carbon-containing compounds, such as cellulose, are more resistant to breakdown than others, and carbon incorporation into cellulose remains in the product for a rather lengthy time, sometimes for thousands of years. This makes clear the importance that this biopolymer has not only in our everyday's life, but also, and most of all, on large time scale events, through the balancing of CO2 levels over long time periods.

A possible solution to the extra CO2 amounts in the atmosphere would be to reverse the conversion process by increasing photosynthesis, which results in the trapping of more carbon dioxide. It is straightforward to understand that a good way to accomplish this task is to enhance the production of cellulose, developing organisms that are able to synthesize this polymer more efficiently and in improved forms. It is also clear that in order to do that, we need to know more about the mechanisms that control and regulate cellulose production in different organisms.

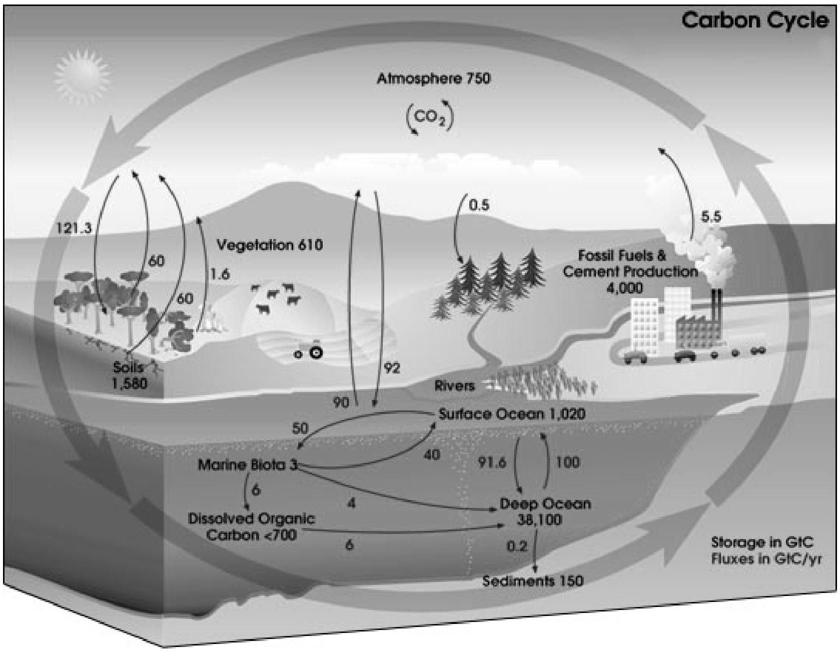

Figure 2.5: The carbon Cycle on earth: the numbers show the total amount of stored carbon (black) and the annual carbon fluxes (gray)

2.5 This Thesis

In this context this thesis can be thought of as an attempt to gather together and elucidate a number of open biological problems concerning the synthesis, crystallization and self-organization of cellulose. Using theoretical methods coupled to simulation techniques, we analyze the mechanism at the basis of cellulose biosynthesis by focusing on two of the most important cellulose producing entities: plant cells and Acetobacter bacteria. The first three chapters of this thesis (3-5) will be therefore related to different issues concerning cellulose biosynthesis in plant cells, while the last chapter will deal with cellulose production in Acetobacter cells.

We start in Chapter 3 proposing a mechanism for the the self-assembly of the cellulose synthase complex (CSC) in higher plants. At present, rather little is know about the internal structure of this protein, as well as about the molecular mechanism that regulates its formation. This enzyme, named also hexagonal rosette, is a transmembrane complex thought to be composed of 36 subunits, the CESA proteins. Using experimental evidences and results from mutants analysis, it is possible to obtain information on the mutual and specific interactions between the CESA. The knowledge of this interaction scheme allows the formulation of a dynamical model, which we will subsequently implement in a MonteCarlo simulation, that is able to reproduce the processive assembly of the final hexagonal complex.

After having studied the formation of the CSC, we pursue presenting a biophysical model that explains the force generating mechanism underlying the propulsion of this enzyme. While polymerizing the cellulose microfibrils (CMFs), the CSC walks through the plasma membrane of plant cells. Early theories assumed the CSC to be linked by motor proteins to the cortical microtubules, supposed to act as rails to guide its motion. In Chapter 4 we present an alternative model for the propulsion of the CSC: we show how the growth of the cellulose CMFs against the membrane causes an accumulation of elastic energy: the energy release, controlled by thermal fluctuations, happens in the form of unidirectional force and propels the CSC through the membrane. Our model is able to provide an estimate for the velocity of the CSC as a function of the other relevant parameters of the system (bending energies, temperature and polymerization rate constants) that is very close to the experimental value.

We go on investigating in Chapter 5 the process involved in cell wall deposition: depending on the orientation of the CMFs in the plant cell wall, one can obtain very regular and different textures, among which the helicoidal pattern is the most striking one. A fundamental and fascinating question is how the CMFs become oriented during the deposition at the plasma membrane. The current textbook explanation for this phenomenon is again a guidance system mediated by cortical microtubules. However, too many contradictions are known for this to be a universal mechanism, notably in the case of helicoidal arrangements, which occur in many situations. Our aim in this Chapter is to use geometrical considerations to formulate a mathematical model for the spatio-temporal evolution of the orientation of the CMFs in the cell wall. We show how the solutions of our model can generate a great variety of textures, including the helicoidal one. Moreover, we show that our solutions are robust against different perturbations and noise effects, suggesting that this mechanism can be considered a strong and successful tool for the explanation of a great variety of cell wall textures.

Finally, in Chapter 6, we focus our attention on Acetobacter bacteria. These rod-shaped organisms live at the air-liquid interface and swim while producing a long and flat cellulose ribbon. The ribbon is composed by cellulose CMFs that are synthesized by a row of catalytic sites positioned along the long axis of the cell. Once polymerized, the CMFs cooperatively bend and become oriented along the axis of the bacterium. The aim of this Chapter is to explain such orientation mechanism, by the means of theoretical and numerical techniques. Our goal is to correlate this phenomenon with a hydrodynamic effect due to the interactions between the cellulose chains and the fluid in which they are immersed. To demonstrate that this can actually be the case, in the second part of the Chapter we implement a Brownian Dynamics simulation which explicitly reproduces the bacterial motion together with the cellulose orientation mechanism.

With this work we hope to contribute in elucidating some key questions, both regarding the cell biology of plants as well as concerning the physics of interacting filaments and complex macromolecular assemblies.

3 The Cellulose Synthase Complex

The universal distribution of cellulose among prokaryotic and eukaryotic organisms attests to its ancient evolutionary history. This polysaccharide is in fact synthesized by all land plants, a number of bacterial species, many groups of algae, the slime mold *Dictyostelium* and tunicates in the animal kingdom. It is an extracellular polymer, and with the exception of bacteria and tunicates, it is generally the main component of the cell-wall, a rigid shell that surrounds the cell. The diverse function that cellulose plays in different groups of organisms is reflected by the particular structure of the polymerizing enzyme, the cellulose synthase complex (CSC), in each of the different species. Even though specific features are found in CSCs from different organisms, it is believed that the catalytic region is conserved in all these enzymes.

The goal of this chapter is to provide a comprehensive view of the structure and the features of the CSC in different organisms. To do this, we first illustrate examples of CSCs in various species. Then we narrow our attention to plants, analyzing in detail the structure and the chemical composition of the CSC in this case. Finally, we build a model that elucidates the assembly of this enzyme in plants, algae and bacteria, and which suggests how a unique mechanism may be responsible for the formation of this multiform protein complex at least in these three species.

3.1 A bit of history...

One of the great enigmas in plant biology is the biosynthesis of cellulose. During the past 50 years, the site of cellulose synthesis has been investigated intensively, but until few years ago there had been no direct proof for the presence of the multimeric enzyme complex whose existence had been postulated by Preston in 1964 (15). According to Preston's theory, the "Ordered Granule Hypothesis", an array of catalytic subunits forming the cellulose synthase, would function together to synthesize glucan chains that would then self-assemble to form a cellulose microfibril (CMF). In the 1960s, with the advent of the freeze fracture technique, capable of revealing replicas of the interior of membrane surfaces, investigators began to notice highly ordered, multiparticulate protein subunits in association with cell membranes. In 1976 Preston's vision was realized as being most likely true with the first successful application of freeze fracture on the membrane of the fresh water alga "Oocystis apiculata" (Fig. 3.1a) that led to the imaging of ordered structures at the tip of the CMFs.

These structures were linear multimeric arrays, termed "linear terminal complexes" (linear TCs), and consisted of three rows of subunit particles. The complexes were intimately associated with the CMFs, as clearly evidenced by impressions of the cellulose fibrils on the E-fracture face of the plasma membrane. Subsequently, in 1980, a different arrangement was found for the cellulose enzyme (16), a cluster of six particles associated with CMF's imprints in the P-fracture face of the plasma membrane of corn root cells (Fig. 3.1b). Due to the regular hexagonal arrangement of its six transmembrane subunits these particles were named "rosette TCs". Although already identified for several decades, the definite biochemical proof that these structures indeed are the location of the cellulose synthases in vascular plants, was only provided in 1999 (17). Eventually the rosettes have been found to be exclusive for all land plant cellulose assembly, including mosses, ferns, liveworts and certain green alga.

In the following we will use for the cellulose TCs (linear or rosette) the most general nomenclature "cellulose synthase complex" (CSC).

3.2 The diversity of CSCs: shape and arrangement

In general, CSCs are observed as particle arrays by freeze-fracture electron microscopy. At present, four distinct types of CSC packing are known: single linear rows, multiple linear rows resulting in a rectangular CSC, single rosette composed of six particles subunits and clusters of rosettes. Linearly arranged CSCs in single or multiple rows are observed in bacteria, tunicates and some algae (18; 19; 20). Considerable variations in the linear CSCs are found in the number of subunits as well as the arrangements of subunits. Hexagonal structures with six-fold symmetry are observed in mosses, ferns, algae and vascular plants (21; 22; 23) and their morphology is conserved between species more than any other structure. Clusters of rosettes are found in algae such as *Micrasterias Denticulata*.

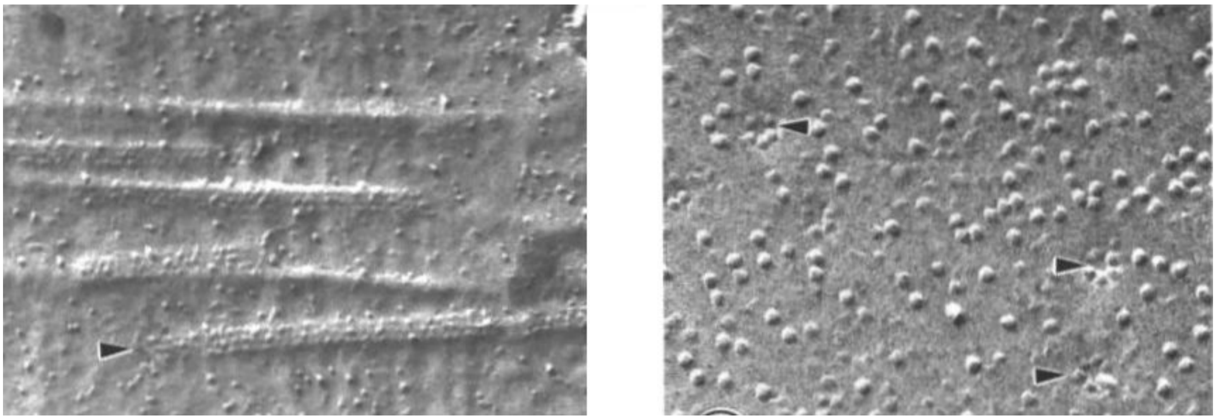

Figure 3.1: CSCs in Oocystis (left) and Zea Mais (right)

3.2.1 Algae

Since 1976, CSCs have been found in more than 14 algal genera, and presently a distinct pattern of CSC's structure is beginning to emerge. The differentiation of CSCs is great among the algae: a single row of particles is observed in brown algae (20) and some red algae. Multiple rows are found in algae with wide microfibrils, glaucophycean algae (24), some red algae (25), chlorophycean and ulvophycean green algae (26). Diagonal rows of particles, as shown in Fig. 3.2a, are observed in the xanthophycean algae such as *Vaucheria hamata* (27; 28).

In contrast to linear CSCs, some species of algae show rosette CSCs which appear identical to those in vascular plants. All embryophytes, the Zygnematales, the Coleochateles and the Charales, which are thought to be the closest relatives of land plants, (23) have six particles rosette, except for *Coleochaete Scutata*, which has a unique CSC consisting of eight particles. Differently from any other alga, the *Micrasterias Denticulata* shows the typical rosette CSC only during primary wall synthesis. During secondary wall synthesis in fact the single rosettes aggregate forming hexagonally ordered complexes (Fig. 3.2b) that result in synthesis of bands of thicker microfibrils (29).

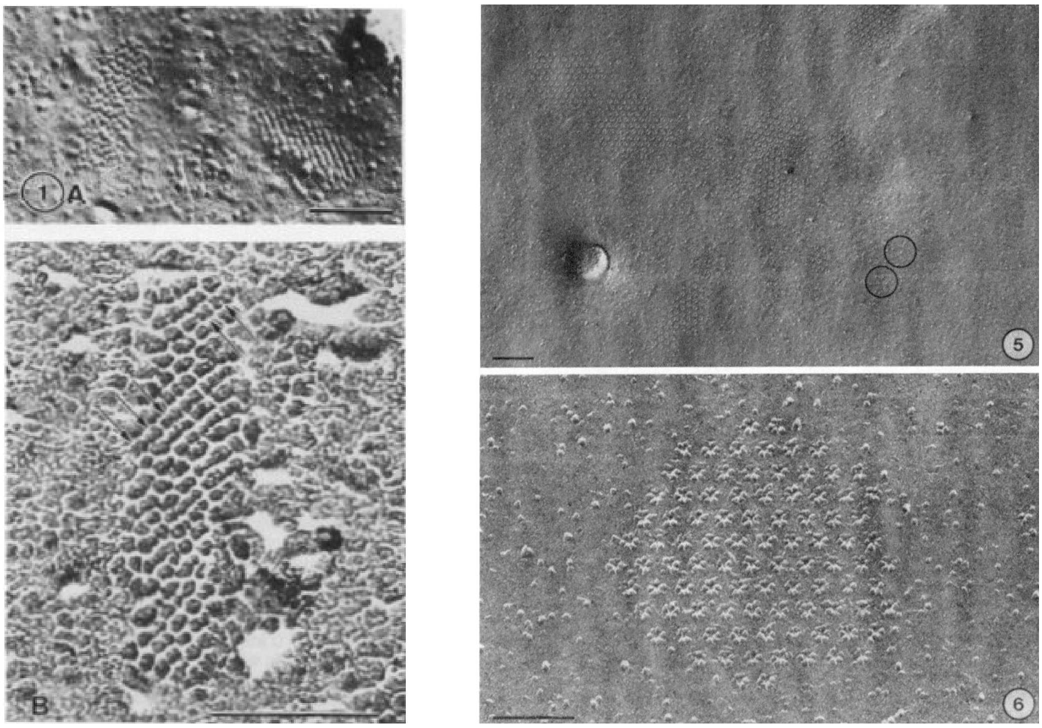

Figure 3.2: CSCs in Vaucheria (left) and Micrasterias Denticulata (right)

3.2.2 Bacteria

Among the prokaryotes, the purple bacteria are thought to be the most advanced (30), being considered as progenitors of mitochondria in the eukaryotic cell (31). Interestingly, many genera in this group synthesize cellulose. The best known examples are various species of *Acetobacter*, *Rhizobium* and *Agrobacterium* (32; 33). Among these, *Acetobacter Xylinum* is a model system for the understanding of cellulose biosynthesis from the aspects of molecular genetics and biochemistry: it produces massive amounts of cellulose, which is secreted not as a cell wall polymer like in eukaryotes, but as an extracellular pellicle (for more information on *Acetobacter Xylinum* go to Chapter 6). In all purple bacteria the site of cellulose synthesis is a linear row of particles parallel to the longitudinal axis of the cell (18).

In addition to this bacterial group, also *Escherichia Coli*, *Klebsiella Pneumoniae*, *Salmonella* (34) and *Sarcina Ventriculi* (35) produce cellulose.

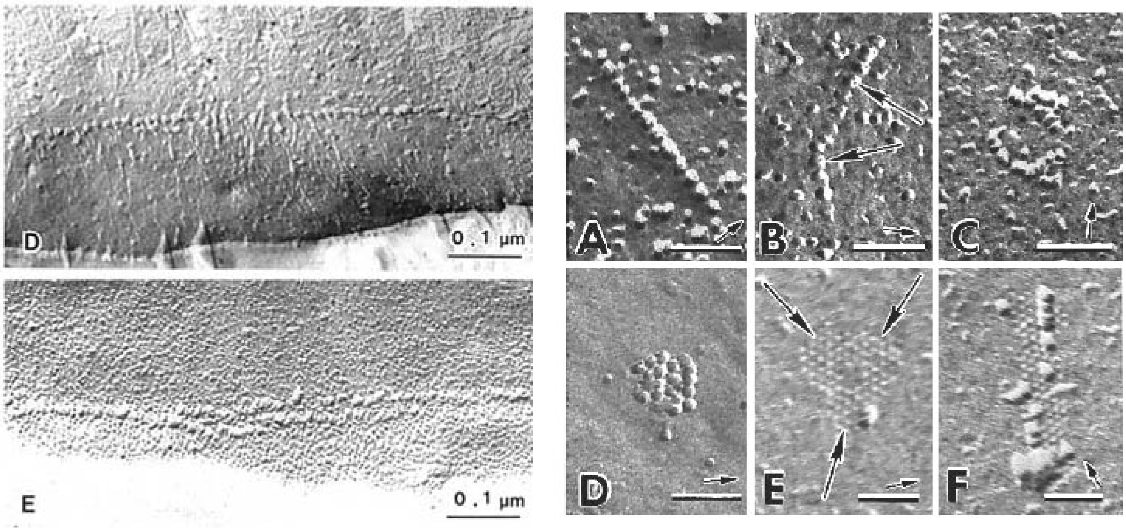

Figure 3.3: Linear CSCs in Acetobacter (left). Linear (a,b,c) and multiple linear CSCs (d,e,f) in Dictyostelium (right).

3.2.3 Amoebae

Cellular slime molds are a simple group of eukaryotic organisms located at the base of the phylogenetic tree. They diverged from the animal lineage after the split from plants, but before fungi. The species *Dictyostelium Discoideum* grows as free- living amoebae in the litter stratum, feeding on bacteria. Once the food supply is exhausted, *Dictyostelium Discoideum* undergoes a complex developmental cycle in which about 10.000-50.000 individual amoebae aggregate in the face of starvation, and differentiate. At the beginning the amoebae organize in a multicellular body, the mould, that soon starts elongating forming a migratory slug which behaves as a single organism. During development, *Dictyostelium* cells produce a number of cellulose-based structural elements: an example is the extracellular matrix, comprised of proteins and cellulose, synthesized by *Dictyostelium* slugs around themselves.

CSCs in *Dictyostelium Discoideum* (36; 37) are unlike any so far found among eukaryotic cells (Fig. 3.3). They appear to consist of a single linear row of about 12 particles in motile prestalk cells, with an arrangement somewhat similar to the one found in *Acetobacter*. However, when the prestalk cell turns into the stalk tube and stops moving, the single linear CSCs collapse until multiple linear CSCs form, creating cluster up to 48 particles. This is one of the most important example of how cell motility regulates two modes of cellulose synthesis.

3.2.4 Animals

Tunicates, small marine invertebrates that are abundant worldwide, are the only animals able to perform cellulose biosynthesis (19; 38). The most familiar tunicates are the sea squirts, or *Ascidians*, cylindrical or globular animals usually found attached to rocks, shells, pilings, or boat bottoms. In the *Ascidians*, cellulose is a product of the epidermis and is incorporated into a thick outer coat known as the tunic, for which the tunicates are named. The tunic surrounds the surface of the animal's soft body to protect it against predators, it is often transparent or translucent and varies in consistency from gelatinous to leathery. The structure of CSCs in Tunicates was categorized at first to the linear type (21). However, the CSCs of most of the *Ascidians* have a unique feature as compared with other types of linear CSCs that have been found in bacteria, algae and slime molds. They are composed of two kinds of membrane particles (Fig. 3.4): small subunits (7.2 nm) corresponding to the cellulose synthases, and large particles (14.5 nm in diameter) surrounding the synthase complexes. It is not clear, however, whether this feature of "double CSCs" is universal in all *Ascidians* or not.

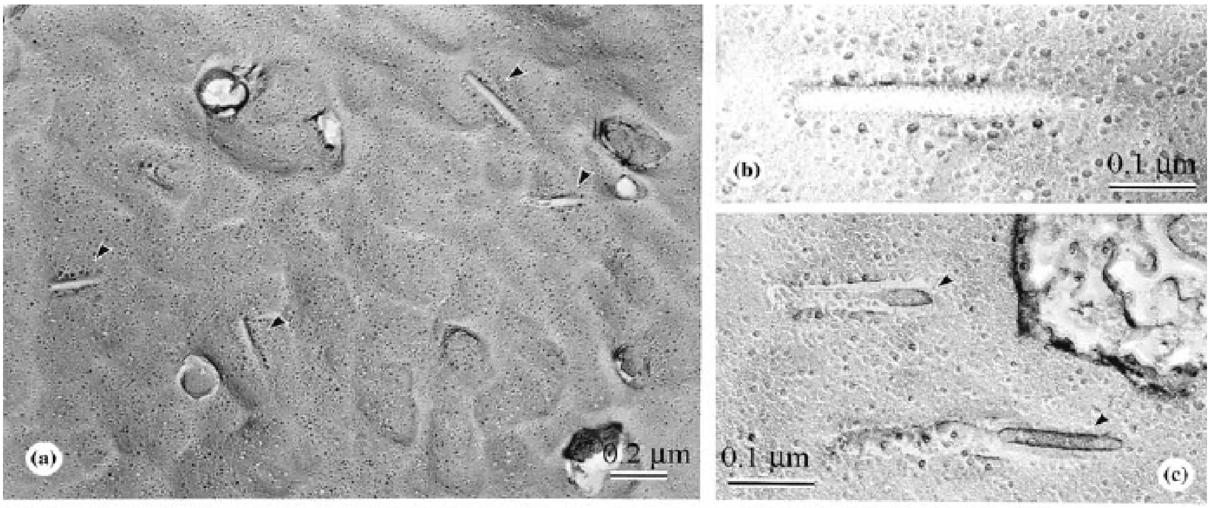

Figure 3.4: CSCs in Tunicates

3.3 Cellulose CSCs in higher plants

Interestingly, among the vascular plants only the rosette CSC (Fig. 3.5) has been found. Thus, algal ancestors with rosette CSCs have assumed additional importance with respect to understanding the evolution of land plants. The rosette CSC was first described by Muller and Brown in 1980 in Zea mays (16). In vascular plants, like mosses and ferns, gymnosperms and angiosperms (39), this enzyme appears as a protein complex with a six-fold symmetry and a diameter of 25nm.

The genes that encode the catalytic subunits of cellulose synthase are called *CESA* genes. They were first identified at the molecular level in the cellulose producing bacteria *Acetobacter* and *Agrobacterium* (review in (22)). From the sequences of these enzymes, motifs characteristic of cellulose synthase have subsequently been recognized. In the late 1990 the first *CESA*s of a plant were identified trough molecular and genetic studies (40; 41). Presently the most information is known about the *Arabidopsis Thaliana CESA* gene family, the *AtCESA*, since the *Arabidopsis* genome is fully sequenced. In this model plant the *CESA* family contains at least ten genes, which are expressed in different tissues and cell types. Sequence data indicate that the *CESA* gene family is as large, or larger, in other plants species.

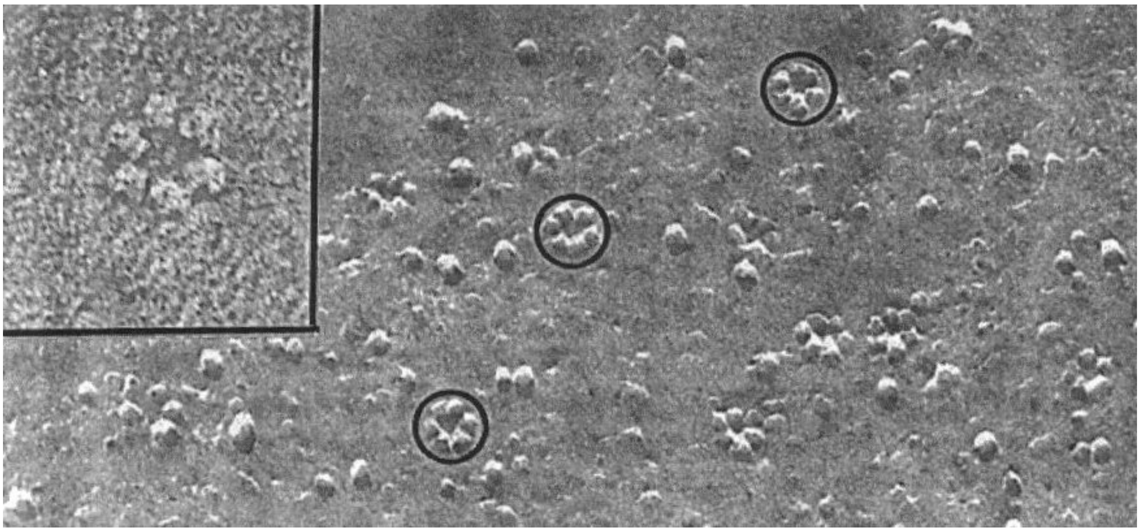

Figure 3.5: Rosette CSCs in the plasma membrane of a vascular plant

3.3.1 CESA proteins: localization and function

CESA proteins, the *CESA*s gene products, have been localized to the rosette CSCs in the plasma membrane of plant cells by immunocytochemistry (17). The smallest subunits that are visible by electron microscopy, and that constitute the six lobes of the rosette, are thought to consist of six CESA proteins. Consequently, the total number of CESA subunits forming the rosette is believed to be 36. As cellulose is a major component of all higher plants cell wall, CESA proteins are expressed in all cell types of the plant. However, the various members of the family in each species are differentially expressed in tissue types.

3.3.2 Isoforms: really identical?

The 10 *CESA* genes contained in *Arabidopsis* are named *AtCesA1-10* (42). It is currently unclear why plants contain so many *AtCESA* genes. The observation that these genes have overlapping expression patterns may mean that they are functionally redundant and thus play identical roles in cellulose biosynthesis. However, phylogenetic analyses tend to group CESA proteins known to be involved in primary wall formation separately from those involved in secondary wall formation, indicating that CESA may not be functionally analogous. This hypothesis also relates to the additional question of how many different CESA isoforms are required for cellulose production within a cell.

If all the CESA were functionally entirely identical, they would be randomly assembled into rosettes. Therefore a mutation in each of the components could be likely to affect the ability of the rosettes to function normally, leading in any case to a reduced cellulose production. Furthermore, if these isoforms were interchangeable, then the total CESA pool size should be the limiting factor in cellulose production, rather then the amount of each CESA isoform.

Interestingly, growing evidence from genetic experiments and gene-expression analysis indicate that only mutations in some of the *CESAs* have an effect in cellulose synthesis. Furthermore, it has been shown that in some cases one CESA isoform cannot effectively compensate for the loss of another. This strongly suggests that the presence of some of the isoforms is critical for cellulose synthesis, and argues a case for non-random incorporation of CESA proteins into rosettes.

3.3.3 Mutants

There are a number of mutants currently known in plant cellulose synthase genes. Here we list the most important mutations in *Arabidopsis Thaliana* (for simplicity we will omit the gene's prefix *At-*).

The *rsw1* temperature-sensitive mutation in *CESA1*, when grown at the non-permissive temperature, causes a specific reduction in cellulose synthesis in primary cell wall, the accumulation of non-crystalline $\beta(1,4)$ glucan, disassembly of cellulose synthase, and widespread morphological abnormalities (41).

In addition to *rsw1*, mutations in *CESA6* gene results in a deficiency in cellulose in primary cell wall. This suggest that both *CESA1* and *CESA6* are required for cellulose synthesis in the primary cell wall.

The *irx3* (irregular xylem3) point mutation in *CESA7* shows a defect in secondary cell wall formation in xylem. As a result, the *irx3* mutant have weakened walls and collapse upon themselves (43; 44). The *irx1* point mutation in *CESA8* is a member of the same family of mutants as *irx3*, and causes a reduced production of cellulose in secondary wall.

Not to be confused with *irx* is *ixr1* (isoxaben resistance). There are two mutants alleles, *ixr1-1* and *ixr1-2* that confer resistance to the cellulose biosynthesis inhibitor isoxaben. Both alleles are point mutations in the *CESA3* gene, suggesting that this gene may also be required for primary wall cellulose synthesis. Another mutation that confers resistance to isoxaben is *ixr2*, a point mutation in the *CESA6* gene.

Recently a novel mutant, *irx5*, has been discovered, which has severely reduced secondary cell wall cellulose. This phenotype is caused by a mutation of the *CESA4* gene.

Finally, *procuste1* is one of a class of mutants that show decreased elongation and increased radial expansion in hypocotyls in Arabidopsis. *Procuste1* is mutation a in the *CESA6* gene, the same gene as *ixr2*.

3.4 Rosette structure

The assembly of CESA subunits into hexamers is still not well understood. However, the data on mutants shown above suggest that there are two different non-overlapping sets, each composed at least by three CESA proteins, which are responsible for the formation of an operative cellulose-synthesizing complex. The triplet CESA4, CESA7 and CESA8 (whose mutation corresponds respectively to the *irx5*, *irx3*, and *irx1* mutants) is required to correctly assemble the cellulose rosette in the secondary cell wall (45); on the other hand, CESA1, CESA3 and CESA6 (corresponding to the *ixr1*, *ixr2* and *rsw1* mutants) are needed for the synthesis of the primary wall (41; 46). This hypothesis is consistent with the idea that CESA proteins are not functionally redundant but, rather, play distinct roles in the cellulose biosynthesis mechanism.

Understanding how three CESAs interact to form a functional rosette CSC is essential for a proper comprehension of how single $\beta(1,4)$ chains of glucose are synthesized, and how these chains become organized into crystalline microfibrils. So far there are two main models proposed for the architecture of the rosette: the first one is based on the hypothesized CESAs interactions in primary cell wall, while the second one makes use of the known experimental evidences in secondary cell wall extracts.

3.4.1 Model for CESAs interactions in primary cell wall

Based on the experimental results concerning the isoxaben resistance of *ixr* mutants, Robert *et al.*(46) have proposed for the cellulose synthase in *primary wall* the model shown in Fig.(3.6a). As said in the previous paragraph, the triplet CESA1, CESA3 and CESA6 is thought to be required for cellulose synthesis in primary wall. Alterations in both *CESA3* and *CESA6* genes produce the isoxaben-resistant mutants *ixr1* and *ixr2*. However, no *ixr* mutant has been found found associated with alterations in *CESA1* gene. A possible interpretation for the existence of two non-redundant resistance loci in the rosette, is that the herbicide directly or indirectly recognizes a binding site associated with a complex containing both CESA3 and CESA6, but not CESA1. Moreover, studies on cotton show that CESA proteins have the capacity to form homo dimers through their N-terminal ring-finger domain. Together these data support the model shown in Fig. 3.6a. In this picture, each globule contains 3 homodimers of distinct CESA isoforms: CESA3 and CESA6 form an isoxaben-sensitive complex, so that mutations in both these proteins can provide resistance to isoxaben, while mutations in CESA1 do not cause such resistance.

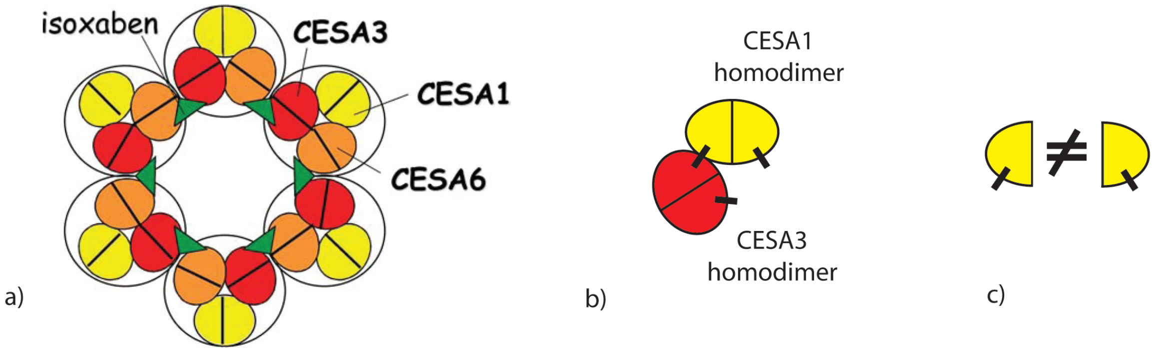

Figure 3.6: (a) Model for CESAs interactions in primary cell wall. (b) Interactions between CESA1 and CESA3 homodimers. (c) Interactions between two CESA1 subunits

Even if this model is able to explain the resistance to isoxaben in a consistent way, it doesn't resolve the self-assembly of the rosette from a dynamical point of view. The formation of the multiparticulate enzyme is a very complex procedure, in which nothing can be left at random. Since the 6 globules are supposed to be identical, it is straightforward to believe that the first step in the formation of the whole complex is the assembly of the single globule. However, in this context, there is nothing that assures the correct formation of the globule. To better understand this last point, let's focus on the interactions between the CESA1- and CESA3-homodimers: in order to bind to each other these dimers must share some binding loci, for example the binding arms shown in Fig. 3.6b. However, for symmetry reason, the proteins that form each of the dimers (the two CESA1 and the two CESA3) must be identical to each other. As you can see form Fig. 3.6c, this is clearly impossible. It is therefore very hard to understand how the three homodimers can interact in the right way to form a functional globule, and subsequently a functional rosette.

3.4.2 Model for CESAs interactions in secondary cell wall

The model for the architecture of the rosette in secondary cell wall has been originally proposed by Scheible in 2001. In this section we first examine in detail the experimental evidences that led to the formulation of this model. Then, based on these results, we build an interaction scheme for the CESAs proteins in secondary cell wall extract. Finally, we implement these interactions in a dynamical model, which we demonstrate to be able to reproduce the processive assembly of the cellulose synthase complex.

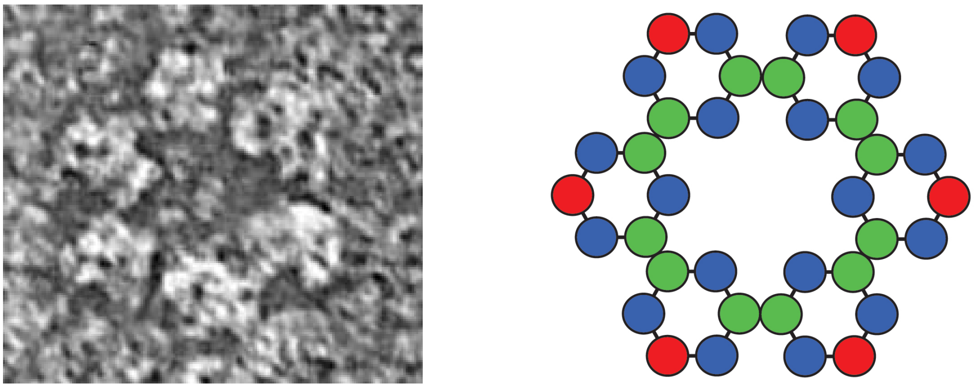

Figure 3.7: (a) Rosette CSC. (b) Model for CESAs interactions in secondary cell wall

3.4.2.1 Experimental evidence

Immunoprecipitation and co-localization studies carried out on secondary cell wall extracts (45; 47) have shown that CESA8, CESA7 and CESA4 are expressed in exactly the same cells at the same time. In addition, stems from *irx1*, *irx3* and *irx5* mutated plants all contain approximately a third of wild-type cellulose levels, suggesting that CESA4, CESA7 and CESA8 are equally important in cellulose synthesis. Consistent with this suggestion, experiments have demonstrated that the three isoforms are all coimmunoprecipitated in wild type cells by using antibodies specific to CESA8. Identical results were obtained when antibodies specific to either CESA4 or CESA7 were used. These findings indicate that the three proteins associate and are all part of the same multimeric complex.

In order to determine the interactions of two of the subunits when the third component of the complex is not present, experiments on mutant backgrounds were realized. Interestingly, they demonstrate that in solubilized extracts from *irx5-1* plants, in which there is no detectable CESA4 protein, CESA8 is no longer precipitated by the anti-CESA7 antibody. At the same time, in these types of cells, CESA7 is no longer detectable in the proteins precipitated by the anti-CESA8 antibody. To check the validity of the experiment, control tests were conducted: they clearly indicate that CESA8 and CESA7 are both present in the *irx5-1* extracts.

Another analysis was performed using a mutated form of CESA8 (in *irx1-1* plants). In *irx1-1* extracts, antibodies specifically recognizing CESA7 and CESA4 were able to coprecipitate CESA8, in a manner identical to that seen in wild-type. Thus, the presence of a mutated form of CESA8 did not affect the interactions of the three proteins. This suggests that CESA8 may differ from CESA4 in that it is not required for assembly of the other two subunits.

3.4.2.2 Rosette self-assembly in secondary wall: the model

If we consider the rosette assembly purely from a theoretical perspective, at least two different types of interactions can be envisaged, one between CESA proteins within a rosette subunit and one between rosette subunits. For symmetry reasons, we consider the six lobes of the rosette being structurally identical. As said before, each of the lobes is thought to be composed of 6 CESAs, that have to assemble in a highly ordered manner to make a full size complex. Assuming the spatial extent of the three different CESAs to be comparable, we argue an hexagonal arrangement of the six proteins within each rosette subunit.

This disposition implies that the CESAs should have at least two binding sites positioned at 120° one from each other (Fig 3.9). On the other hand, each of the lobes is itself a subunit of the hexagonal rosette, and therefore it also should have two binding sites positioned a 120° one from each other. This is possible only if at least one of the three CESA types possess a third binding sites that links two of the rosette lobes (Fig. 3.8a). Therefore, there must be at least two isoforms, one with 2 binding sites and one with 3 binding sites, for the correct assembly of the rosette to occur. What, then, is the role of the third isoform discussed in the previous section?

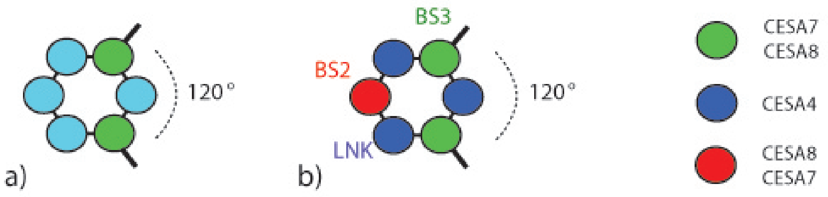

Figure 3.8: (a) In order to form the hexagonal rosette the lobes must have two binding sites positioned at 120° one from each other. (b)Possible model for the structure of the single lobe

As already said, interactions between CESA7 and CESA8 are below the limits of detection in secondary wall extracts in absence of CESA4. This strongly suggests the idea that CESA8 and CESA7 are not directly connected, and that CESA4 acts like a linker between the other two. One possibility then would be the one shown in Fig. 3.8b: in this picture the blue particles, which we will call "linkers" (LNK) from now on, represent the CESA4 proteins; the green spheres with three binding sites (BS3) could be exclusively the CESA7 or the CESA8, and the red subunits (BS2) would correspond to the third component of the system. This scheme is consistent with the mutant analysis discussed in the last section: in normal cells in fact, CESA7 and CESA8 (BS3 and BS2) are linked through CESA4 (LNK) and manage to coimmunoprecipitate. If LNK is removed, however, like it happens with CESA4 in the *irx5-1* plant cells, BS2 and BS3 particles are no more connected and behave independently.

Based on these considerations, Doblin proposed for the rosette CSC the structure shown in Fig. 3.7b (48; 49). In this model the CESAs are represented as spherical particles that interact with each other through oriented binding-arms. As illustrated in Fig. 3.9, each of these three particle has specific interactions. In particular, LNK can bind with BS3 as well as BS2, BS2 can bind only to LNK and BS3 can bind with itself as well as with LNK.

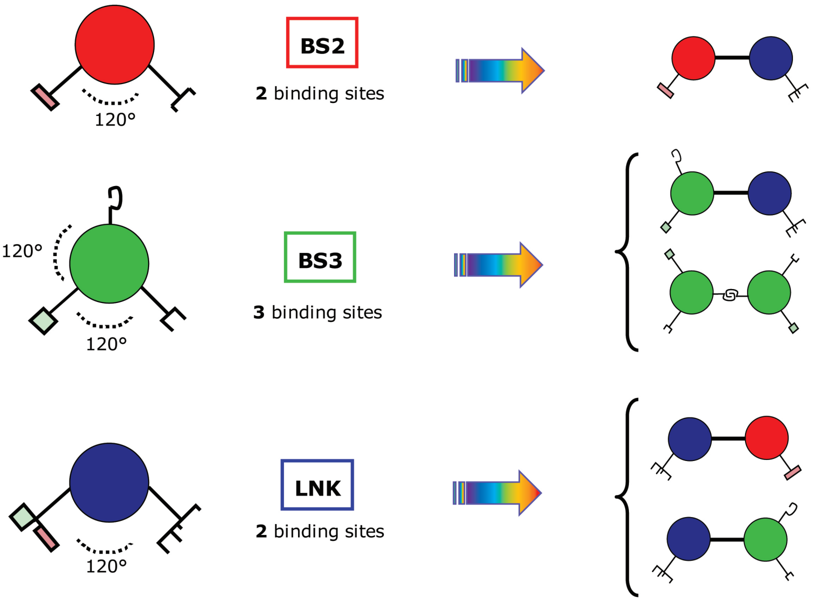

Figure 3.9: Scheme of CESAs interactions

3.5 How does a rosette assemble? Monte Carlo answers...

In order to demonstrate that the interaction scheme displayed in Fig. 3.9 is actually able to resolve the self-assembly of the rosette, we have performed a Monte Carlo simulation. The Monte Carlo scheme consists of a series of stochastic transitions between different system configurations, all satisfying the imposed constraints. In our simulation each Monte Carlo step involves the displacement (translation or rotation) of a randomly chosen particle. The simulation starts with all the particles, of diameter σ, positioned at the vertexes of a grid, in a planar box with reflecting boundary conditions. Since the CESAs particles are thought to assemble in the plasma membrane, we have performed our simulation in a two-dimensional space.

The probability of a given move depends on the energy difference between two successive configurations, i.e. the trial move is accepted with a probability

$$P(E_i \to E_f) = \min[1, e^{-\beta(E_f - E_i)}]$$

where E_f and E_i are respectively the energies of the final and initial system state. This rule satisfies the detailed balance condition that ensures the correct sampling of the equilibrium phase space. After the trial move has been carried out, three situations can occur: 1) the particle has moved over another particle, in which case the move is rejected because we are supposing hard-core interactions among the spheres; 2) the particle has moved over a free spot; 3) the particle has bound to another particle.

Since the interactions are very specific and orientation-dependent, the "binding event" can happen only if: a) the interaction rules of Fig. 3.9 are satisfied; b) the distance d between the two particles is $\sigma < d < 1.2\,\sigma$; c) their binding arms are correctly co-aligned. Each binding event corresponds to a decrease in the total energy of the system of a quantity that depends on the specific interaction, as discussed in Table 3.1.

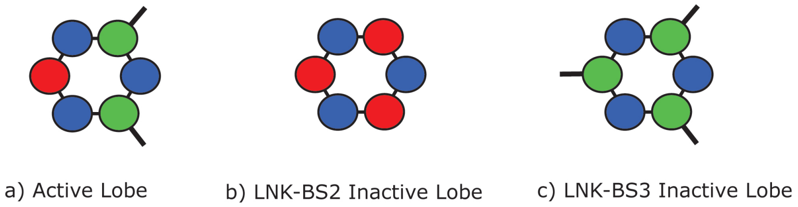

Figure 3.10: Active (a) and inactive lobes (b-c)

The rules described in Fig. 3.9, although being extremely specific, allow for the formation of three types of rosette subunits (Fig. 3.10): the ones with all the three types of particle forming the ring (we will call these "active lobes"), and the ones with only two type of subunits (LNK-BS2 and LNK-BS3 "inactive lobes"). Since we know that the rosette CSC contains at least three types of particles, and since we have assumed the identical structure of the six lobes, to prevent the formation of "faulty" rosettes we have to impose that only active lobes can associate to form the final hexagonal product. Moreover, we also require the BS3-BS3 binding event between two rosette subunits, to occur only when both of the rings are already completely formed. The closure of the rosette-ring prior to the complete formation of the lobes, in fact, is an obstacle to the correct assembly of the rosette itself.

Interaction	*Binding Energy*
BS2 ⇔ LNK	$\varepsilon_{2,L}$
BS3 ⇔ BS3	$\varepsilon_{3,3}$
BS3 ⇔ LNK	$\varepsilon_{3,L}$

Table 3.1: Binding energies for CESAs interactions

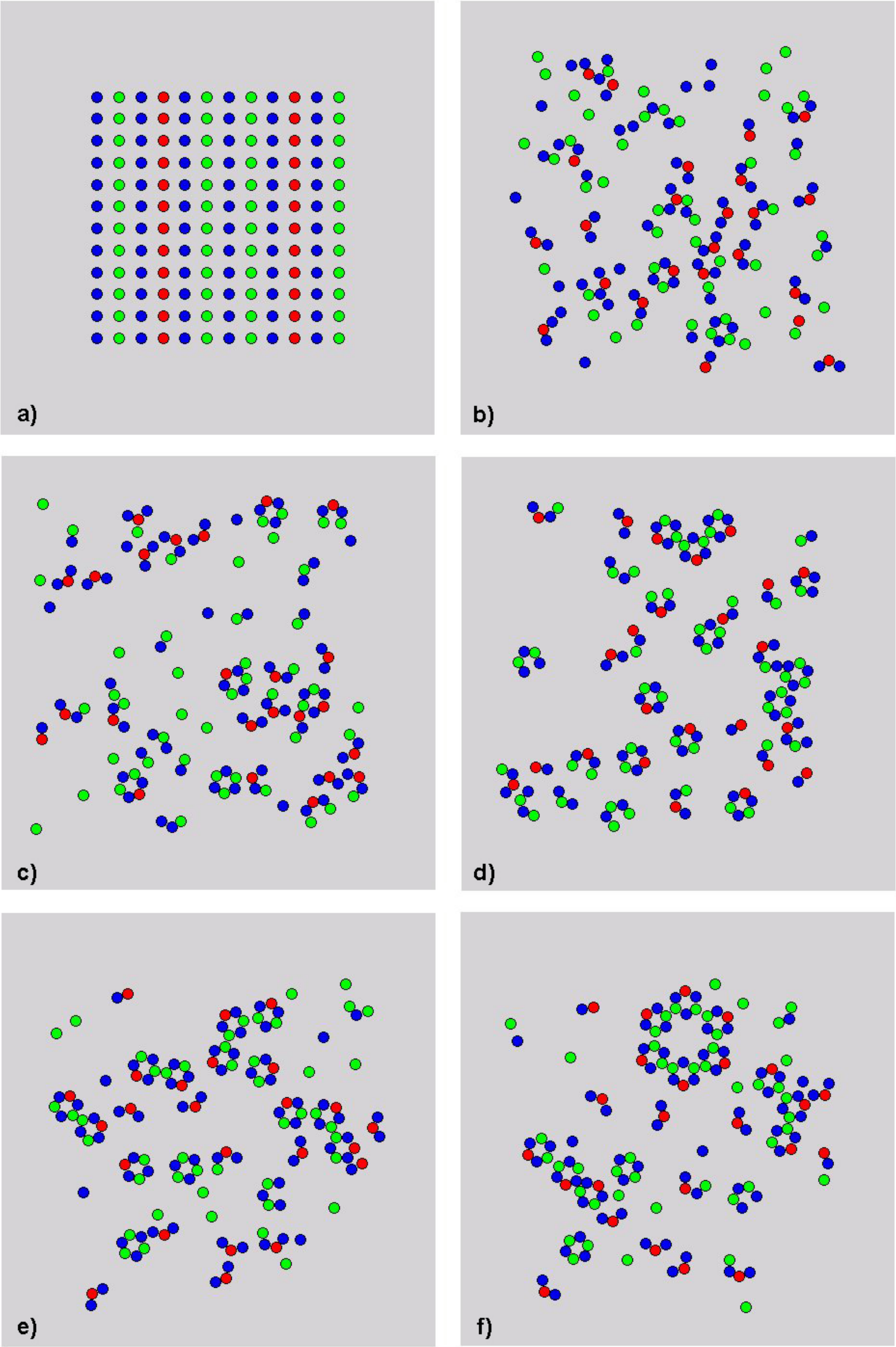

Figure 3.11: Six successive frames of the Monte Carlo simulation

3.5.1 The simulation

Here we present the results of our simulation. The total number of particles in the system is 144, and the initial ratio of the three system's components is exactly the one needed for the correct assembly of 4 single rosettes.

Fig. 3.11 shows six snapshots of the simulation. During the first stages of aggregation, the CESAs undergo brownian motion and start to interact forming dimers and trimers of subunits. Subsequently the first rosette subunits begin to emerge (Fig. 3.11b-c), and some of them rapidly aggregate with each other forming two- three-lobes structures (Fig. 3.11d-e). These structures then bind together and the rosette is finally formed (Fig. 3.11f).

Looking carefully at the images we can see that the trimers which are initially formed are mostly LNK-BS2-LNK (blue-red-blue) type. This specific pre-aggregation event is essential for the correct formation of active lobes, and strictly depends on the choice of the binding energies. By setting conveniently the energies ratios in such a way to have $\varepsilon_{2,L} >> \varepsilon_{3,L}$ (see Table 3), it is possible to favour the LNK-BS2-LNK linking with respect to the LNK-BS3-LNK one, and increase in this way its stability. Once these main LNK-BS2-LNK trimers are created, the six lobes can correctly complete their self-assembly. Fig. 3.11b shows some lobes already formed in a pool of subunits. Interestingly, together with correctly assembled lobes, here we can note also the presence of LNK-BS3 inactive complexes, i.e. lobes in which the BS2 subunit is missing. Even if the interaction rules of Fig. 3.9 in principle allow for this anomalous binding to happen, their occurring is rare due to the low stability of these complexes.

3.5.1.1 Need of a chaperone?

For the correct assembly of the rosette to happen we had to make two main assumptions: only a) active and b) completed lobes can associate to form the hexagon. However, these conditions are not sufficient to ensure the formation of an intact rosette. The BS3-BS3 binding site in fact should be blocked in some manner for a ring rather than a linear array to be assembled.

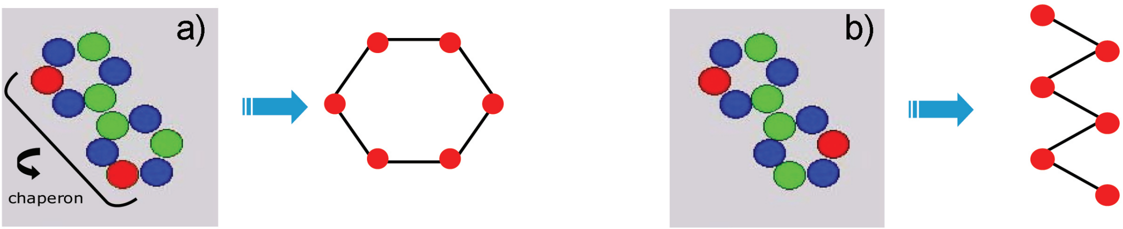

Figure 3.12: The presence of a chaperone could be necessary for the choice of the ring (a) or the zig-zag (b) configuration

We can understand this point more easily looking at the Fig.(3.12): once two active lobes are completely formed and thus ready to interact, they can bind to each other in two different ways. In the first mode (Fig. 3.12a), that we call the "ring" configuration, the lobes interact in such a way that the BS2 particles are always on the same side. This arrangement is necessary for the correct formation of the hexagon ring (Fig. 3.7). In the "zig-zag" configuration the lobes interact in such a way that the red particles are always on opposite sides. Interestingly, this arrangement is not inconsequential, but it brings to the assembly of linear complexes very similar in structure at the ones found in some algae and bacteria (Fig. 3.14).

The task of selecting one of the BS3-BS3 binding modes could be performed by chaperones. The chaperone is a molecular complex that aids in the folding of a protein and prevents it from taking conformations that would be inactive. In this case one or more chaperones would have to act like switches, choosing between the linear and the zig-zag configurations depending on the final CSCs structure that has to form.

3.5.2 What about Micrasterias?

As pointed out in the previous section, the alga *Micrasterias Denticulata* shows during secondary wall synthesis a very particular CSCs arrangement: the single rosette aggregate forming clusters with an hexagonal structure (Fig. 3.13). We can question whether this kind of structure can be explained with the same interaction rules used for the rosette CSC and the linear CSC. Well, as shown in Fig. 3.13, this is actually possible.

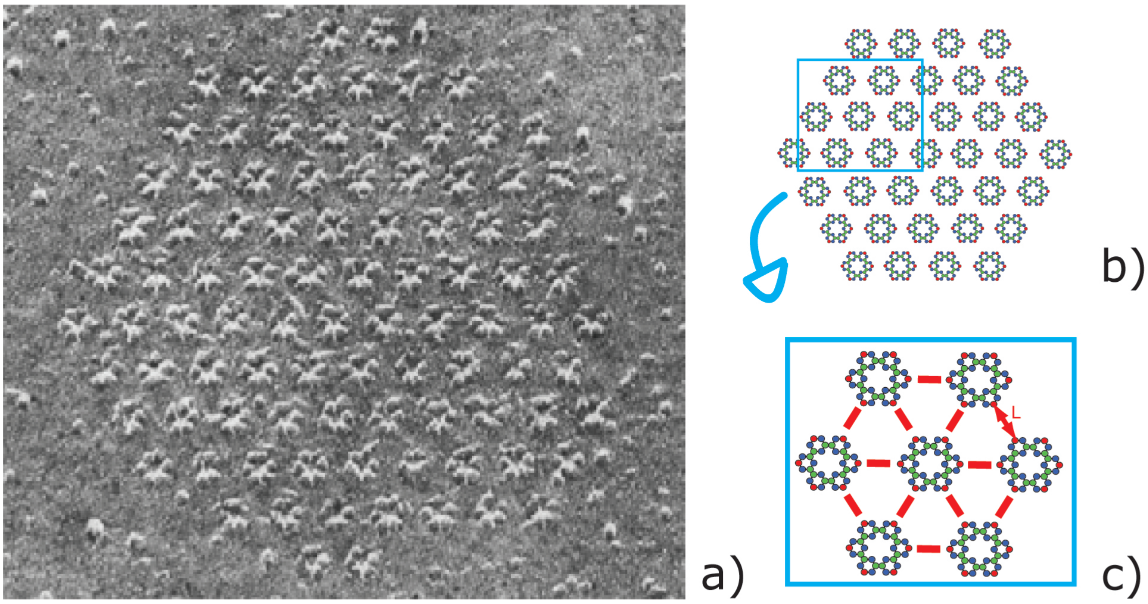

Figure 3.13: (a) Hexagonal clusters of rosettes in the secondary cell wall of Micrasterias; (b-c) Model for rosette's interactions

What we need for the formation of the hexagonal cluster of rosettes is a simple ingredient: a long-range interaction among BS2 particles. Suppose that the BS2 particles, instead of having the two binding sites described in Fig. 3.9, possess three binding arms. Two of them are short-range, and allow for connections with only blue particles, as previously discussed. The third one, instead, is long-range, and links two BS2 subunits, belonging to different rosettes, in such a way that their distance is a certain length L. As shown in Fig. 3.13, the presence

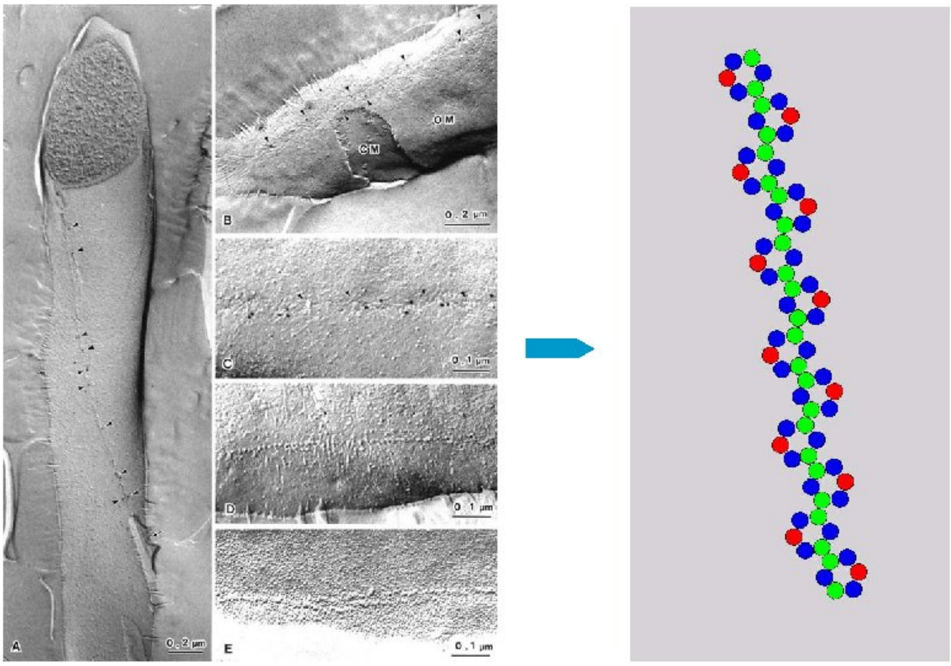

Figure 3.14: Linear CSCs in Acetobacter, real image (a) and model structure (b)

of this new link makes possible the construction of hexagonal clusters, very similar to those present in secondary cell wall of *Micrasterias* (Fig. 3.13).

It has to be noted that in principle also the LNK-BS3 inactive lobes could interact forming hexagonal structures in a manner similar to the rosette's cluster. However, in this case, the two-particles lobe would interact with each other always via short-range links, and the final structure of this aggregation process would be an homogeneous hexagonal pattern, different from the one observed in real algae.

3.6 Conclusions

In this chapter we described a model for the self-assembly of the cellulose rosette CSC in secondary cell wall of plant cell. Our model, besides documenting in detail all the steps involved in the rosette CSC's building, is also able to explain the formation of linear CSCs as well as clusters of rosettes. Nevertheless, our model does not adequately explain how rosette assembly would occur in cells in which there are apparently less than three CesA isoforms expressed. Clearly, further characterization of rosette components and their interactions, as well as the unequivocal identification of which CesA proteins are assembled into a rosette in a particular cell-type, is required before any conclusions can be drawn as to the merits of this model.

4 A polymerization driven molecular motor

In plant cells, cellulose occupies a dominant place being the major component of the cell wall, an extracellular assembly that acts like an external skeleton and which constitutes the principal feature distinguishing plants from animals. The cell wall derives its robust mechanical properties from its ingenious construction (for a detailed description of the cell wall architecture go to Chapter 5): it consists of stacks of thin lamellae (50), all deposited parallel to the plasma membrane, that are formed by long and mostly crystalline aligned cellulose microfibrils (CMFs) embedded in a matrix of polysaccharide "packing" material (51; 52). The CMFs, which represent the structural unit of the cell wall, are constituted by bundles of glucan chains that are synthesized and extruded from the plasma membrane by a moving transmembrane protein complex (go to Chapter 3 for details), the rosette CSC (Fig. 4.1).

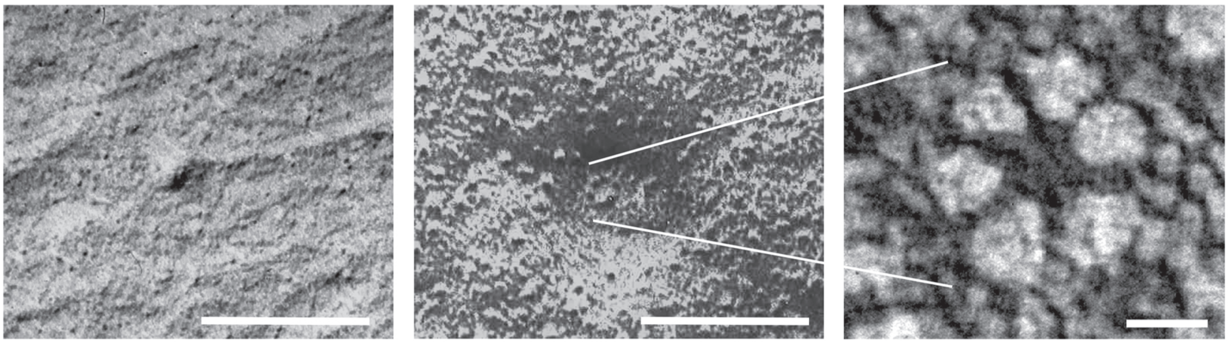

Figure 4.1: Electron micrographs from freeze-fracture preparations of plant cell walls showing a so called terminal-complex, the imprint of a cellulose synthase complex (CSC), with an attached cellulose microfibril (CMF) in the exoplasmatic face of the plasmamembrane (left panel), a so-called particle rosette, the outward facing side of the CSC, within a characteristic depression of the plasmamembrane (right panel, scale bar is 100 nm) and a close-up of the particle rosette with is typical six sided symmetry (inset in right panel)

The aim of this chapter is to explain the mechanism at the basis of CSC motility in plant cell. We show how the concept of a brownian polymerization ratchet, originally proposed by Peskin *et al.* to explain force production by growing polymeric filaments such as microtubules (53; 54), can also serve as a basis for describing CSC propulsion in the plasma membrane of plant cells. However, we argue that obtaining a full understanding also requires taking into account the geometry of the deposition process, the additional driving force provided by the crystallization of the cellulose, and finally the role of the elastic energy stored in the nascent microfibril as well as in the deformable plasma membrane.

4.1 Functioning of the CSC

The assembly of the CSC occurs in the interior of the cell, presumably in the endoplasmic reticulum and in the Golgi apparatus. Current estimates of the diameter of the CSC on the endoplasmic side are in the range of 40 – 60 nm (55), making the CSC one of the largest protein complexes so far observed. Once assembled, the complex is then transported to the plasma membrane for activation and cellulose synthesis. Since most of the structure of the CSC is deeply embedded in the cytoplasm of the cell, EM images of freeze fracture preparations of the P-face of plant membranes are only able to show a small fraction of the structural unit. What these pictures reveal is a characteristic structure of six hexagonally arranged particles forming a ring, or “rosette” (56; 16), with diameter of approximately 25 nm (Fig.4.1). At the locus of the rosette, a depression on the P-side of the membrane (Fig. 4.1b) can be seen to associate with a bulge on the E-side, from which the growing tip of a CMF departs (Fig. 4.1a and Fig. 4.2a).

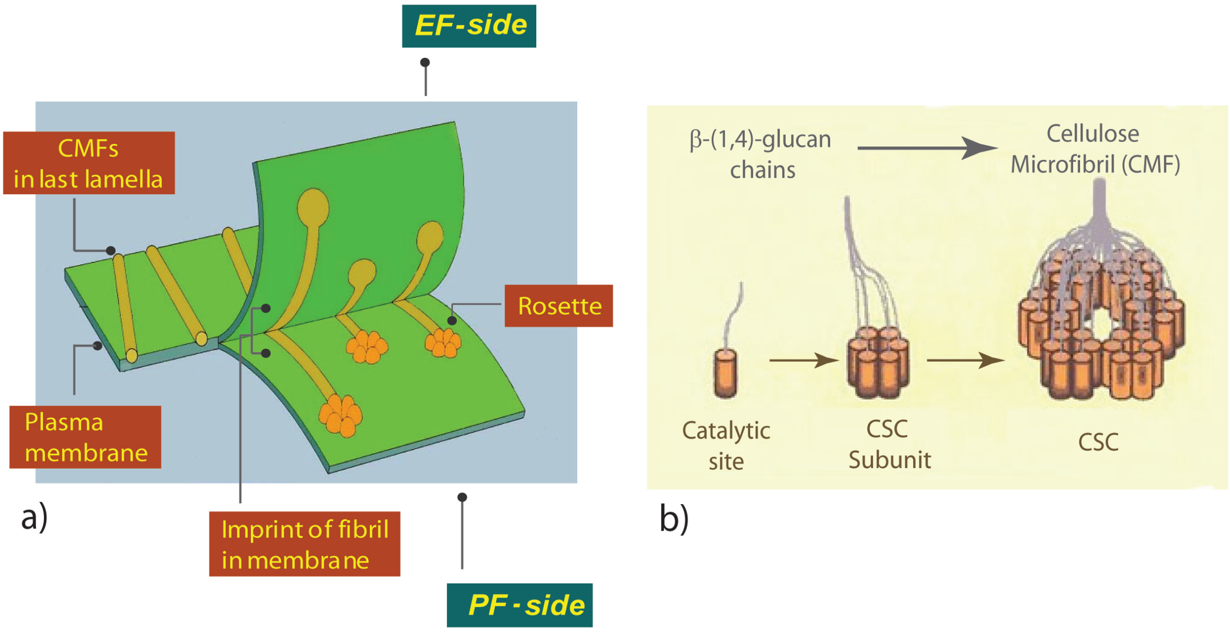

Figure 4.2: (a) Cartoon representing the rosette and the CMF in the double layered plasma membrane; (b) Cartoon of the 36 glucan chains emerging from the rosette

The current view about cellulose synthesis in plant cells (go to chap. 2 for further reading), is that each of the six lobes of the CSC in turn consists of six cellulose synthases, each of them polymerizing a single glucan chain using UDP-glucose as a substrate (22) . These individual chains are then assembled into the CMF, which by implication consists of $6 \times 6 = 36$ chains

(Fig. 4.2b), consistent with the known crystal structure and the measured cross-section of approximately 3.5 nm (22; 57). Since the cell wall is deposited from the inside out, and since the CSC is bound to the membrane, the deposition of new CMFs has to take place in the limited space between the outer surface of the fluid plasmamembrane and the earlier deposited rigid cell wall. For this process to work it had to be assumed that the CSC would have to move in the plane of the membrane (58), leaving behind a CMF in its track. The latter hypothesis has now finally been confirmed (59).

Although the idea that the CSC moves was widely accepted, the question of the origin of this movement has so far received less attention. Obvious candidates for the required force production are motor proteins, molecular chemical energy transducers that are involved in many different biological tasks (60; 53). Examples are processive molecular motors such as kinesin, that can transport organelles and vesicles using cytoskeletal elements as tracks, or non-processive motors such as myosins that deliver the power strokes for muscle contraction, both using ATP as fuel. Indeed, one of the early theories (61) assumed the CSC to be linked by a motor protein to a cortical microtubule, that then acted as a rail to guide the motion. Another proposal (62) had the cortical microtubules acting as force producers themselves, which by setting up a shear flow in the membrane provide a motive force to the CSC. Later, it was realized that in principle the energy released by the glucose polymerization process could by itself be sufficient to propel the CSC (63). In addition, it was shown that preventing CMF crystallization through Calcofluor treatment led to a thickening of the cell wall, suggesting a dysfunctional dispersion of the CSC along the membrane (35). This observations put in correlation the movement of the CSC with the CMF's polymerization and crystallization processes, but to date a detailed mechanistic explanation of how the CSC's motion is achieved was lacking.

In this chapter we develop an explicit biophysical model to explain CSC motility. Before digging into the details of the model, however, we need to recover the basic mechanism through which, in a cellular environment, work can be produced from chemical energy: the Brownian Polymerization Ratchet.

4.2 The Browian Polymerization Ratchet

At the size scale of a cell or a protein assembly within a cell, Brownian motion plays a fundamental role. Thermal collisions constantly batter cellular components, and cells have learned to exploit some of this random motion and convert it in a directed way. In the last 15 years, different physical models have been proposed for how chemo-mechanical energy transduction is carried out at the microscopic level by filament polymerization (54; 64). These models, called Brownian Polymerization Ratchets (BPRs), are variations on the theme of the 'Brownian ratchet', whose name comes from the hypothetical perpetual motion machine proposed by Feynman (65). Feynman's ratchet shows how random thermal motion can be harnessed with the help of an external energy source such as a temperature gradient (the details of this machine are reported in Appendix C). Even if large temperature gradients are essentially impossible to maintain over small cellular distances, Feynman's concept of the Brownian ratchet can be readily extended to other energy sources, such as electric fields and non-equilibrium chemical reactions that are available to cells (66).

Brownian ratchets of all sorts share three basic characteristics. First, there is a discrete step or event that defines the steps of the ratchet: a potential of some kind with periodic energy minima in space or time. Second, there is random thermal motion in some component of the system, providing variability somewhere so that the machinery can move both forward and backward. Third, critically, there is an energetic asymmetry, either in the periodic potential or in some other potential, that creates a preferred direction for the cycle to turn. In most interesting biological cases, the asymmetry is provided by a non-equilibrium chemical reaction. In our case, this non-equilibrium reaction is a polymerization process where the attachment event is much more frequent the the detachment one.

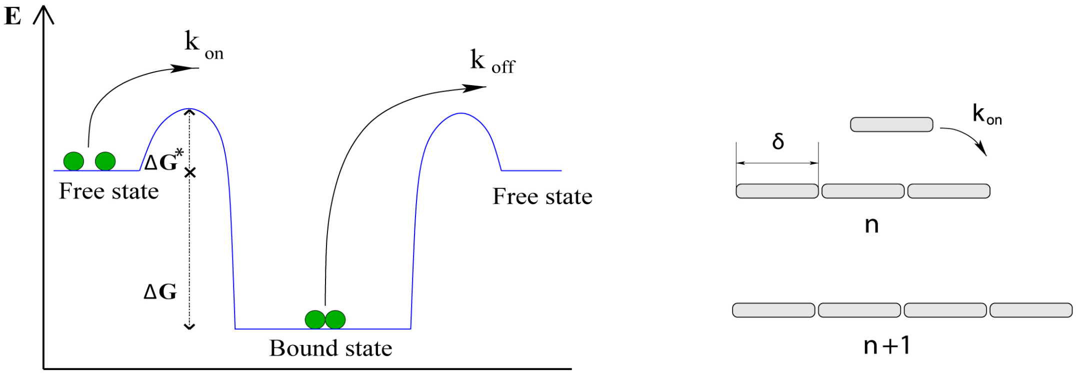

(a)

(b)

Figure 4.3: The polymerization ratchet.(a) Energies of the bound and unbound state. (b) The elongation process

In the brief introduction on the BPR that follows, we will describe how thermal fluctuations manage in transducing the chemical energy into directed motion. To achieve our aim, we divide the conversion process in two steps: first, we show how chemical energy can be extracted from a polymerizing filament; then, we explain how thermal fluctuations succeed in transforming this chemical energy into mechanical energy, and hence into work.

4.2.1 Extracting the chemical energy

The chemical energy that is transduced into mechanical pushing force by filament polymerization, is stored in the difference ΔG in chemical potential (Gibbs free energy) between the free monomer form and the polymer form of a protein subunit (Fig. 4.3a)(67). In general, filament polymerization can be thought of as a simple bi-molecular binding reaction, where a free subunit binds to the end of a polymer formed by n subunits to generate a filament of length n+1 (Fig. 4.3b). The transition rate between the free and the bound state is determined by the energy barrier $\Delta G*$ (Fig. 4.3a). If the free energy of the bound state is equal to the free energy of the subunits in the free state, then $\Delta G = 0$, and $k_{on} = k_{off}$. Filament elongation proceeds spontaneously whenever the free energy of the subunit in solution is greater than the free energy of the subunit in the polymer. Whenever there is excess free energy ΔG liberated from a chemical reaction, it can in principle be harnessed and converted into another form of energy.

There are two main physical models that describe how the ΔG available from spontaneous polymerization can be used to provide a pushing mechanical force (54; 64). In both, the discrete step corresponds to the addition of a single protein subunit to a filament tip. In both, the energetic asymmetry is provided by the difference in free energy between the free- and bound- state for the monomer. The difference between the two lies in where the thermal motion comes into the system (Fig. 4.4).

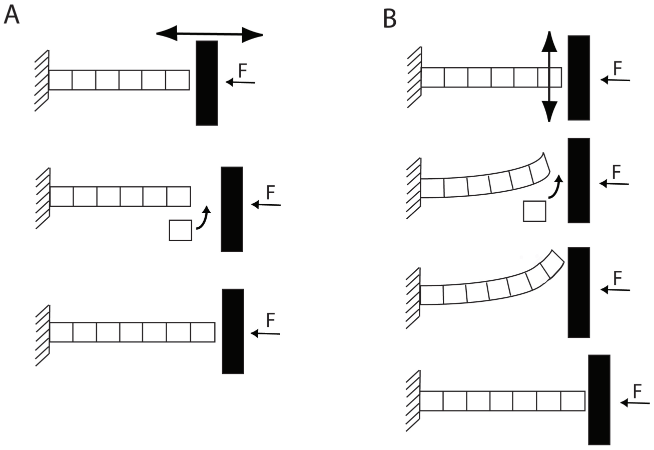

Figure 4.4: The two models for BPR: (a) rigid filaments and (b) semi-flexible filaments

4.2.2 BPR for rigid filaments

The first model, proposed by Peskin *et al.* in 1993 (54), envisions a simple filament, fixed at one end, that encounters a diffusing load which is being pushed by a force F against its other tip (Fig. 4.5). As the load bounces around by thermal motion, it attempts to move both backward and forward. Backward diffusion is inhibited by the presence of the filament. Forward diffusion, though limited by the pushing force, is allowed, and every so often the excursion distance is sufficiently large that a new protein subunit can intercalate between the filament tip and the load, ratcheting the position of the object one step further. For the filament to add a new monomer, the load must be pushed forward by a distance δ that corresponds to the size of the protein subunit, and thus, an amount of work $W = F\,\delta$ has to be done against the pushing load.

This physical model allows calculation of the speed at which an object can be pushed by a polymerizing filament. In particular, if we indicate by k_{on}^0 and k_{off}^0 the free attachment and detachment rates of monomers (corresponding to the situation in which the polymer does not have any pushing force nor load at its tip), we simply have for the free-growing case an expression for the polymerization velocity that reads like:

$$v_0 = \delta(k_{on}^0 - k_{off}^0). \tag{4.1}$$

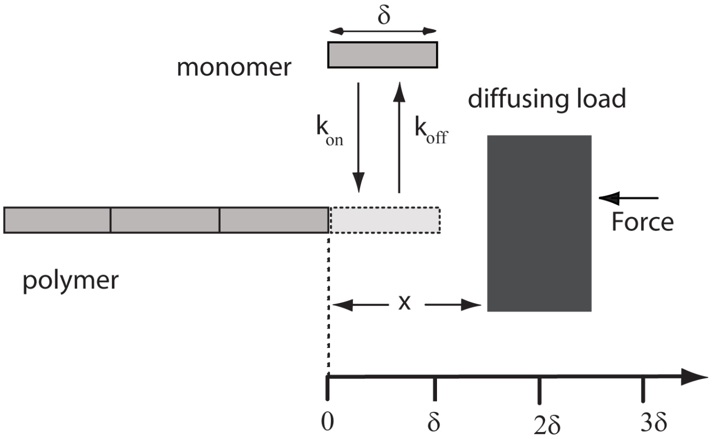

Figure 4.5: Details of the BPR for rigid filaments

How do things change in presence of an obstacle? Since the load is being pushed against the polymer, the probability $P(x > \delta)$ of having the gap wider than the subunit size is limiting the polymerization rate. This implies obvious corrections to be made for the effective polymerization rate in presence of a load, which becomes:

$$k_{on} = k_{on}^{0} P(x > \delta). \tag{4.2}$$

However, the model of Peskin *et al.* predicts no change for the de-polymerization rate, i.e. $k_{off} = k_{off}^{0}$. In principle, a load can have an effect on the de-polymerization as well: however, understanding how this change come into action is beyond the aim of our presentation of the brownian polymerization ratchet model and we will not delve into unnecessary details.

Putting together Eq. (4.1) and Eq. (4.2) we finally obtain that the new polymerization velocity in presence of a load becomes

$$v = \delta(k_{on}^{0} P(x > \delta) - k_{off}) \tag{4.3}$$

where, to consistently solve the equation, one needs to evaluate the probability $P(x > \delta)$ (54). Regardless of its specific expression, however, we can argue that it must depend on the diffusion coefficient D of the moving load and on the magnitude F of the pushing force.

4.2.3 BPR for semiflexible filaments

The simple model discussed above is a very useful starting point for understanding how the BPR works. But much like the original perpetual motion machine imagined by Feynman, it ignores the fact that thermal motion must affect all components in the system, i.e., in this case, the filament as well as the load. In most biological situations, the load can be much larger than the filament, and thermal bending of the polymer is much more likely to open a monomer-sized gap between the filament and the load than is diffusion of the whole load.

Based on that idea, Mogilner and Oster described a revised elastic Brownian ratchet model in 1996 (64), where the load is considered to be stationary, and the filament is subject to bending (Fig. 4.4b). In this case the polymerization velocity has an expression that is similar to the one found in the previous model, i.e.

$$v = \delta\cos(\theta)[k_{on}^{0}P(\theta,F) - k_{off}^{0}] \tag{4.4}$$

where now $P(\theta,F)$ indicates the probability that a gap of width $x > \delta\cos(\theta)$ is opened between the tip of the filament and the load that is being pushed with a force F (Fig. 4.6).

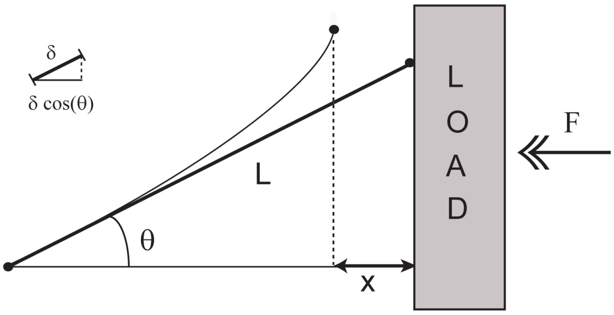

Figure 4.6: Details of BPR for semiflexible filaments

The relationship between force, velocity, and angle with this more realistic model is quite complex, and must be computed numerically (64). However, here we can say that the probability $P(\theta,F)$ is predicted to depend on the stiffness (Young's modulus) of the filament and on the angle between the filament and the load, and does not depend on the diffusion coefficient of the load object like in the previous model. Mogilner and Oster derived the velocities in four limiting cases where filaments are stiff or flexible, and the load force is high or low.

4.3 Modelling the movement of CSC

The two different models described in the previous sections are not mutually exclusive. In reality, it is possible that both elastic bending of the filaments and thermal motion of the load object can cooperate to open up the gap that allows addition of a subunit to the growing filament.

In this section, we are going to build such a more complex mechanism to explain the force generating system underlying the locomotion of the CSC. To achieve this task, we develop our approach in three steps: first, we formulate a model that integrates the relevant physical components to obtain a heuristic explanation for the propulsion process; in the next step, we simplify the model into a form that allows analytical predictions to be made and show that we can reproduce the experimentally measured value for the CSC speed; in the final step, we implement this model in a stochastic simulation, providing a proof of principle of the proposed mechanism.

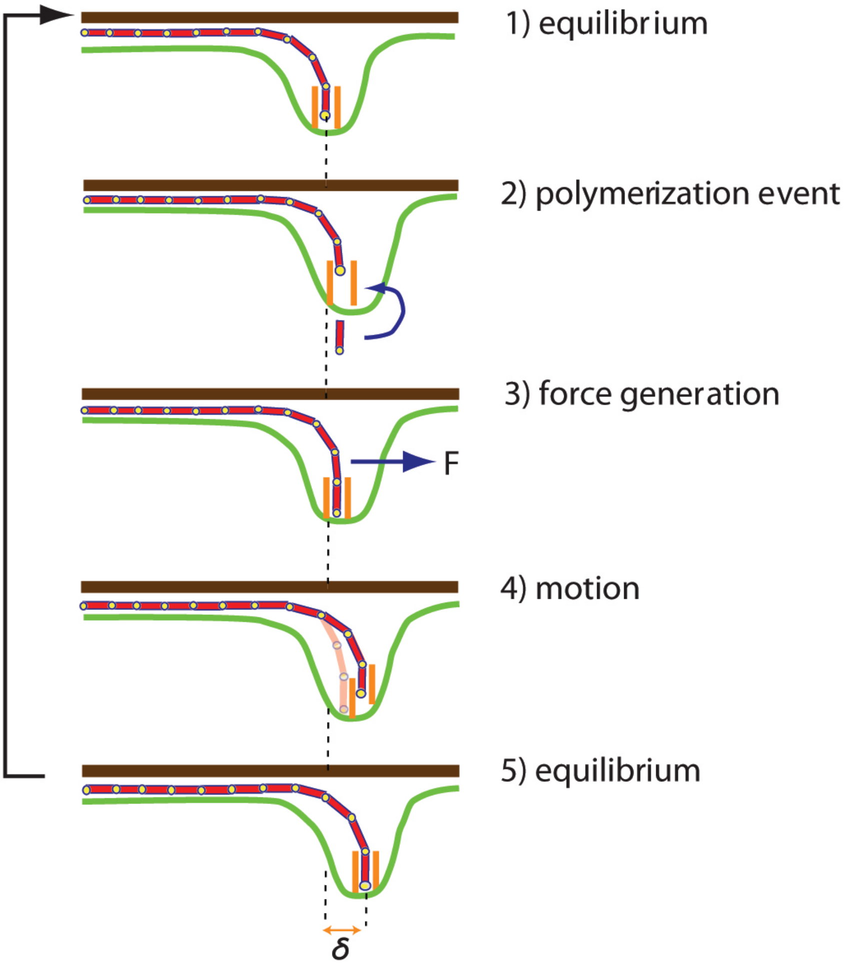

Figure 4.7: Schematic representation of the mechanical cycle in our model of CSC propulsion, illustrated for the case of a single CMF. From top to bottom: Step 1: the filament and the membrane are in thermal equilibrium. Step 2: due to fluctuations of the filament and/or the membrane, a gap of sufficient size is opened allowing a new monomer to be added to the filament. Step 3: the increase in length of the filament causes an accumulation of elastic energy in the system, which generates a force on the tip of the filament. Step 4: the accumulated energy is released in a unidirectional motion of the tip of the filament, which is attached to the CSC. Step 5: the filament has effectively advanced by one monomer unit and equilibrium is restored, allowing the cycle to repeat itself.

4.3.1 The model

The mechanical cycle we propose is responsible for CSC propulsion is illustrated in a schematic fashion in Fig. 4.7. We model the CSC as a planar, membrane-bound object. On the side of the object facing away from the cell a regular array of cellulose polymers is extruded. We model these polymers as inextensible semiflexible chains of beads. The configuration of these polymers is constrained by three factors. The first is their attachment to the CSC itself. Here we assume that this attachment not only fixes the location of the polymer tips, but also specifies the orientation of their first bonds to be perpendicular to the plane of the CSC. The latter assumption is consistent with the hypothesis that the chains emerge from narrow channels in the complex. The second constraining factor is the confining influence of the already deposited cell wall, which we model as an impenetrable barrier. The final constraint arises from the fact that the polymers are at their other ends all linked up into a nascent CMF, which on this scale is an effectively rigid linear structure constrained to lie in the plane of the membrane.

Because the polymers have a finite resistance to bending, the combination of geometrical constraints imposed on them implies that they are in a non-relaxed conformation, resulting in forces acting on their attachment points. At the loci where the polymers emerge from the CSC these forces will typically have both a perpendicular component and an in-plane component. The perpendicular component has two effects: (i) it acts as a barrier for the polymerization process, thus influencing the rate of addition of new monomers, and (ii) it contributes to a net force which pushes the CSC downward, counteracted by an elastic response of the membrane. The latter effect is consistent with the membrane-indentations that are seen in some freeze-fracture images of the CSC (68) (See also Fig.4.1). Note that we disregard the possibility that the CSC “tilts” with respect to the global membrane orientation, as the energetic cost of such short length-scale deformations of the membrane is probably appreciable.

The resultant of all the in-plane force components due to the individual polymers is the net force that drives the linear motion of the CSC. Energy is injected into this system by the polymerization- as well as the crystallization process, as both will tend to increase the stress in the polymers. The energy is dissipated by the work the CSC as a whole performs against the frictional forces it experiences. We stress the fact that thermal fluctuations, which are a dominant effect at the relevant molecular scale, play a crucial role in the whole process, making possible the opening of a gap big enough for the insertion of a new polymer subunit. It is these fluctuations which allow the system to cross (and also to re-cross) the energetic barriers associated with the mechanical constraints imposed on the polymerization process. Like in the BPRs models discussed in the previous sections, it is the rectification of these fluctuations that allow the system to convert chemical energy into directed motion.

4.3.2 Analytical treatment

Now that we have illustrated how the proposed mechanism manages in pushing the CSC through the membrane, we undertake to strip the model to its bare essentials, focusing on a single growing polymer constrained to a 2D planar geometry interacting with an 3D elastic membrane. In this simplified setting, whose projection on a vertical plane is already illustrated in Fig. 4.7, the model can be solved exactly, allowing the polymerization velocity to be determined.

In our analytical picture the chain is modeled as a semiflexible filament with a persistence length ξ_f significantly larger than the typical dimensions of the region where the filament is bent. The membrane is fixed at its edges to a rigid frame of size $\Omega = l^2$, and its equilibrium position is taken to coincide with the hard top wall which represents the already extant cell wall.

We neglect the spatial extent of the CSC, which is now simply represented by the constraint on the verticality of the first bond of the polymer.

We first investigate the equilibrium configuration of the polymer. The active part of the filament can be considered as an elastic rod clamped at one end horizontally to a rigid part, representing the crystallized CMF, and vertically at the tip by the CSC. In order to minimize its elastic energy under the given constraints, such a rod adopts an quarter arc of circle configuration. Recalling that the elastic energy of a semiflexible polymer can be written as

$$E = \frac{J_f}{2} \int_0^L \frac{ds}{R^2(s)} \tag{4.5}$$

where $R(s)$ is the local curvature radius and J_f is the bending modulus of the filament, we obtain that the equilibrium shape of the polymer is a quarter arc of circle of length $\frac{\pi}{2} z_f$, with energy $E_f(z) = \pi J_f / 4 z_f$, where z_f is the vertical distance of the filament tip to the wall. The geometry of this situation is schematically depicted in Fig. 4.8. In the following we will consider the polymer so stiff to always maintain the definite shape of arc of crcle: thermal fluctuations have the only effect to modify its radius of curvature z_f.

The force the tip of the filament exerts on the supporting membrane is

$$F_f(z_f) = -\frac{dE_f(z_f)}{dz_f} = \frac{\pi J_f}{4} \frac{1}{z_f^2}. \tag{4.6}$$

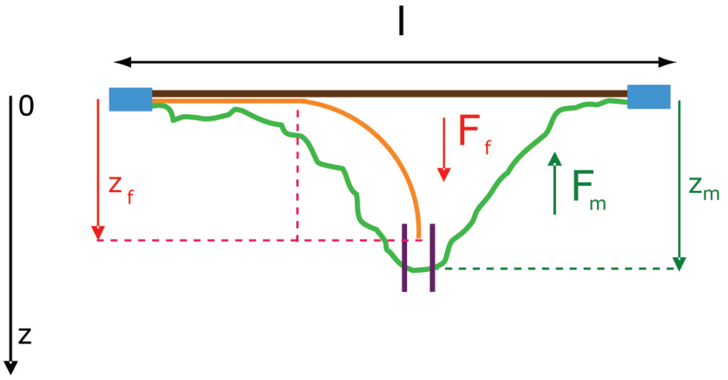

Figure 4.8: Schematic cross-sectional drawing of the geometry employed in the analytical model.

In response to this force the membrane will deform by flattening out as much as possible, generating a counter-force on the tip of the polymer. In order to obtain this opposing force $F_m(z_m)$, being z_m the vertical displacement from the equilibrium configuration of the membrane, we follow the method of Daniels et al. (69), first calculating the partition function for the fluctuations of a membrane described by the energy functional (4.20), that is constrained such that its midpoint can not come closer than a distance z from its unconstrained equilibrium location. Assuming that we are in a regime where the fluctuations of the membrane around its equilibrium position, which scale as $\Delta = (\beta A \gamma)^{-\frac{1}{2}}$, are small compared to the amplitude z of the induced deformation, we can neglect the presence of the rigid wall in $z = 0$ and extend the relevant integrations over all the possible membrane conformations.

The partition function is then given by

$$Q_m(z) = \exp(-\beta A \gamma z^2), \tag{4.7}$$

where $\beta = (k_B T)^{-1}$ and $A = 2\pi/[\log(1 + \frac{\gamma\Omega}{J_m \pi^2})]$, with $\Omega = l^2$ the area of the membrane frame, γ the surface tension and J_m the bending modulus. We assume throughout that the size of the frame is large enough such that all physical results obtained are insensitive to the shape of the frame. When the membrane is constrained such that the midpoint can not be above the location z_m, as is the case when an impinging filament is present, it can only explore those configurations where its midpoint is located at positions $z \geq z_m$. The force the membrane exerts on the filament is thus given by

$$F_m(z_m) = -\frac{\partial \mathcal{F}_m(z_m)}{\partial z_m} \tag{4.8}$$

where the free energy is given by

$$\mathcal{F}_m(z_m) = -\beta^{-1} \log \frac{1}{\Lambda} \int_{z_m}^{\infty} dz Q_m(z) \tag{4.9}$$

with Λ an irrelevant constant added for dimensional purposes. In case $z_m \gg \Delta$, the force is approximately linear in the displacement and given by

$$F_m(z_m) \simeq -2\, A\, \gamma\, z_m \equiv -k_m\, z_m \tag{4.10}$$

which defines the spring constant k_m.

Balancing the two opposing forces F_f and F_m yields the equilibrium position for the filament tip and the membrane midpoint

$$z_{\text{eq}} = \frac{1}{2} \left(\frac{\pi J_f}{A\gamma} \right)^{\frac{1}{3}}. \tag{4.11}$$

To study the fluctuations around this equilibrium position, and assuming that these are small with respect to z_f itself, we linearize the force F_f around z_{eq} yielding

$$F_f(z_f) \simeq \frac{\pi J_f}{2 z_{\text{eq}}^3} \left(z_f - \frac{3}{2} z_{\text{eq}} \right) \equiv -k_f \left(z_f - z_f^{(0)} \right) \tag{4.12}$$

with the effective spring constant given by $k_f = -4A\gamma$ and the effective rest length of the spring by $z_f^{(0)} = \frac{3}{2} z_{\text{eq}}$.

This procedure maps our model conceptually onto a system of two brownian linear springs acting in opposite directions, the polymer downward and the membrane upward. These springs are connected to a thermostat and are coupled by the constraint that the tip of neither spring may pass the other since the polymer and the membrane cannot interpenetrate (see Fig. 4.9), i.e. $z_m - z_f \geq 0$. To determine the velocity of polymerization we then need to evaluate the

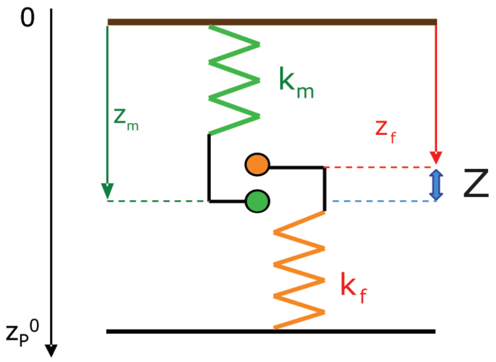

Figure 4.9: The effective model of two coupled springs the analytical model maps onto.

probability that a gap, larger than the monomer size δ, is opened between the filament tip and the membrane midpoint.

Like in the BPRs discussed in the previous sections, thermal fluctuations represent a key element in this process, being the source that allows the system to open such a gap. The dynamics of the growing polymer, assuming a reversible polymerization reaction, is governed by the balance between the rate of addition and the rate of removal of monomers. In the case that the timescale of the thermal fluctuations is fast compared to the polymerization kinetics, the polymerization speed is given by (54) Eq. (4.3), where now the size of the gap between the filament tip and the membrane is identified by the coordinate $Z = z_m - z_f$. It then follows that:

$$v = \delta(K_{on}^0 P(Z > \delta) - K_{off}) \tag{4.13}$$

where we recall that K_{on} and K_{off} are the bare rates of monomer addition and removal respectively, and $P(Z > \delta)$ the probability that the gap of length Z is larger than the monomer size. For the effective two-spring system we derived above, the probability distribution for the tip-membrane gap can be evaluated exactly. Recalling that the probability distribution for a one-dimensional harmonic oscillator in a thermal bath is given by

$$P^{\text{osc}}(z) = \sqrt{\frac{\beta k}{2\pi}} \exp\left\{-\frac{1}{2}\beta k (z - z^{(0)})^2\right\} \tag{4.14}$$

we can determine the probability for a gap of given size $Z > 0$ from

$$P(Z) = \int_{-\infty}^{\infty} dz_m \int_{-\infty}^{\infty} dz_f P_m^{\text{osc}}(z_m) P_f^{\text{osc}}(z_f) \delta\left((z_m - z_f) - Z\right) \tag{4.15}$$

where, as before, we have freely extended the upper limit of the integrations boundaries to $+\infty$ since the product $(P_m^{\text{osc}}\, P_f^{\text{osc}})$ is significantly different from zero only in a small region around $Z = 0$;. Performing these integrations yields

$$P(Z) = \frac{e^{-\frac{1}{2}\beta\bar{k}(Z+z_f^{(0)})^2}}{\int_0^\infty dZ' e^{-\frac{1}{2}\beta\bar{k}(Z'+z_f^{(0)})^2}} \tag{4.16}$$

where the effective spring constant of the coupled system is given by $\bar{k} = k_m k_f/(k_m + k_f)$. In order to assess the validity of the approximations made in deriving the analytical model, we compare the prediction of the gap distribution in Eq. (4.16) with the results we obtain from sampling of a one-filament version of the full stochastic model that will be presented in section 4.3.3. The results are presented in Fig. 4.10 and show a perfect agreement.

Eq. (4.16) in turns allows the explicit evaluation of the probability that the gap is larger than the monomer size

$$P(Z > \delta) = \int_{\delta}^{\infty} dZ' P(Z') = \frac{1 + \mathrm{erf}\left(\sqrt{\tfrac{1}{2}\beta\bar{k}}\,(z_f^{(0)} - \delta)\right)}{1 + \mathrm{erf}\left(\sqrt{\tfrac{1}{2}\beta\bar{k}}\, z_f^{(0)}\right)} \tag{4.17}$$

where $\mathrm{erf}(x)$ is the error function, $z_f^{(0)}$ the equilibrium position of the linearized polymer-spring, $\bar{k}$ an effective spring constant and $\beta = 1/k_B T$ the standard inverse temperature. Taken together, Eqs. (4.13) and (4.17) allow the polymerization velocity, which equals the velocity of motion of the CSC, to be determined as a function of all the relevant parameters. Deferring the numerical estimate of this velocity to the next section, we remark that we can readily deduce that the polymerization velocity increases with increasing temperature and decreases with increasing stiffness of the system, caused either by increased stiffness of the filaments or the membrane. Interestingly the former consideration is backed up with experimental evidence (unpublished data, Brown lab).

4.3.2.1 Results

We can now employ the results obtained through this analytical approach to estimate the velocity of the CSC. In this attempt we are of course limited by the availability of quantitative estimates of the relevant parameters.

We first consider the bending modulus of the effective filament, arguably the least well determined parameter. Using crystallographic data we can provide an upper and a lower bound to the value of J_f as the Young's modulus Y of cellulose is known to vary between 5 GPa for the amorphous state and 150 GPa for the crystalline state (70). We can, however, extract a more appropriate estimate from the depth of the observed indentation of the plasma membrane at the locus of the CSC, which provides an estimate for the equilibrium value of the filament tip to wall distance z_{eq}. Through the use of relation Eq. (4.11) we can then determine $J_f = 8\,A\gamma z_{\mathrm{eq}}^3/\pi$. For typical values of the membrane surface tension $\gamma = 5 \times 10^{-5}$ N/m, the membrane bending modulus $J_m = 2 \times 10^{-20}$ Nm, an indentation depth of $z_{\mathrm{eq}} = 100$ nm and size of the relevant membrane patch $l \approx 300$ nm, we find $J_f = 2.5 \times 10^{-25}$ Pa m^4. Taking the radius of the effective filament to be $r = 1/2$ diameter of CMF $=$ 2nm, we obtain an estimate of $Y = 4J_f/(\pi r^4) =$ 20 Gpa, which falls squarely between the bounds mentioned above. We have to keep in mind that, even if the structure of the CMF is almost perfectly crystalline, at the moment of the extrusion from the CSC the glucan chain aggregates are in a non-crystallized phase. Thus the effective Young's modulus of the aggregate is much lower that the one of a cellulose crystal.

For the polymerization rate we use the value of free polymerization of cellulose achieved by the bacterium *Acetobacter*, the so-called vinegar bacterium that lives at the water-air interface

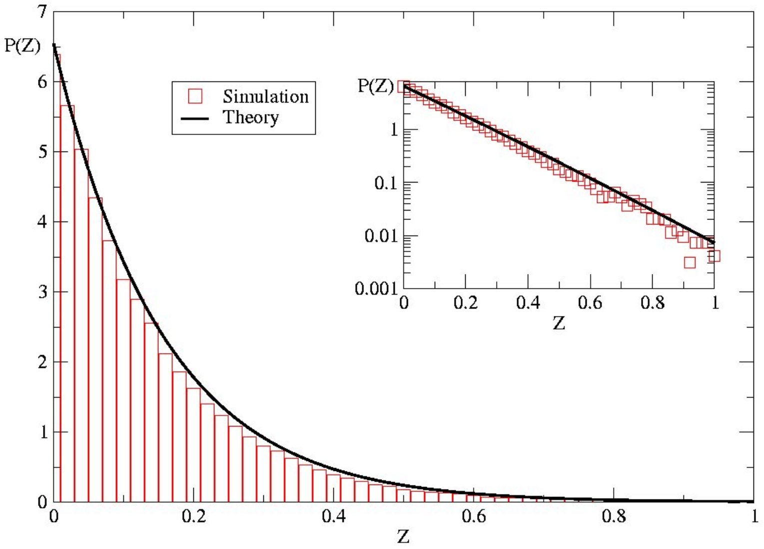

Figure 4.10: The gap probability $P(Z)$ as determined from the analytical model (solid) line, compared to the distribution sampled from a a one-filament stochastic simulation (histogram). The inset is a semi-logarithmic plot that shows how well the tail of the distribution is reproduced.

and propels itself by forces derived from cellulose synthesis (go to Chapter 4 for further details). Strictly speaking, these experiments determine the net rate $K_{on} - K_{off}$, but we assume that the off-rate for these almost irreversible chemical bonding processes is negligible. We therefore take $K_{\text{on}} \simeq 100\ \text{s}^{-1}$ (71; 11) and we neglect the effects of spontaneous depolymerization setting $K_{\text{off}} = 0$. The final parameter necessary is the size of the monomer, which is equal to the size of a glucose subunit, making $\delta \simeq 0.5$ nm.

With these ingredients we can now estimate the speed of the CSC to be

$$v_p = \delta\, K_{on}\, P(Z > \delta) \simeq 4.5 \times 10^{-9} \text{m/s}. \tag{4.18}$$

This number compares favourably to the measured average speed $v_p \simeq 5.8 \times 10^{-9}$m/s observed by the Somerville group (59). We can also compare our results to the estimate of Hirai et al. (72) who observed Calcofluor stained CMFs growing from membrane fragments isolated from Tobacco BY-2 protoplasts. Their estimated elongation rate of $v_b^{\text{extract}} = 1.03 \times 10^{-8}$m/s is higher than that observed *in vivo*, presumably due to the absence of the spatial constraint of an existing cell wall, which lowers the counter-force experienced by the polymerization process. Nevertheless, given the inevitable effects of friction with surrounding aqueous medium this value is still lower than that which we would estimate for totally unobstructed deposition, in which case $P(Z > \delta) = 1$ and we obtain $v_p^{\text{free}} = 5\ \times 10^{-8}$ m/s.

4.3.3 Stochastic simulation

We now implement the conceptual model presented in sect. 4.3.1 in terms of a stochastic simulation. In the following, even though the simulated systems are discretized for numerical purposes, we will express their Hamiltonians in the continuum limit. The Monte Carlo scheme used in the stochastic simulation consists of a series of stochastic transitions between different system configurations, all satisfying the imposed constraints. The probability of a given transition depends on the energy difference between the two successive configurations and satisfies the detailed balance condition that ensures the correct sampling of the equilibrium phase space.

For simplicity we consider a CSC producing 6 effective filaments (EFs), each representing 6 cellulose chains. This simplification is consistent with the mechanism proposed by Cousins et al. (13) in which the approximately 36 cellulose strands that emerge from the CSC are first assembled into 6 glucan chain aggregates, which subsequently coalesce crystallizing into a CMF. The EFs are modelled as bead-chains with a bending potential governing the relative orientation of pairs of neighboring bonds. Each filament is represented as a discrete linear chain of N_f spherical beads of diameter σ that are rigidly connected by bonds of fixed length $\delta = \sigma$. The length of each chain is thus $l_{f_i} = N_{f_i}\sigma$, where the subscript $i = (1..6)$ refers to the i-th filament. The angular bending potential between two subsequent bonds in the chain is given by $U(\theta) = J_f[1 - \cos(\theta)]$, where θ is the angle and J_f is the bending constant that determines the stiffness of the filament.

The already extant cell wall is taken to be a rigid wall located at $z = 0$, into which the beads are not allowed to enter. The EFs emerge from six hexagonally arranged channels representing the CSC. The first monomer-monomer bond (tip) of each filament is constrained to be perpendicular to the plane of the CSC (i.e. is oriented along the vertical axis of the laboratory frame) while the last monomer-monomer bond (tail) is parallel to the horizontal axis. Because of the morphology of the CSC, the tips of the filaments are also constrained to be located at the vertexes of a regular hexagon, with edge-length $R_{\text{hex}} = 6\sigma$. In addition, the beads on different chains have a short range attractive interaction allowing them to crystallize into a compact arrangement.

The individual filaments can be described by inextensible space curves $\mathbf{r}(s)$, where s is the arc-length parameter. The constraint of inextensibility implies that $\frac{d}{ds}\mathbf{r}(s) = 0$, so that the local curvature of a filament is given by $\kappa(s) = \left|\frac{d^2}{ds^2}\mathbf{r}(s)\right|$. In the absence of the constraints, the Hamiltonian for the full bundle of 6 filaments is then given by

$$\mathcal{H}_p^{bundle} = \frac{1}{2} J_f \sum_{i=1}^{6} \int_0^{l_{f_i}} ds_i \kappa_i(s_i) - \varepsilon\sigma^{-2} \sum_{1\leq i<j\leq 6} \int_0^{l_{f_i}} ds_i \int_0^{l_{f_j}} ds_j\, \theta\left(\sqrt{2}\sigma - \left|\mathbf{r}_i(s_i) - \mathbf{r}_j(s_j)\right|\right) \tag{4.19}$$

where the binding energy ε is attributed to each pair of monomers on different filaments that are closer than the attraction radius $\sqrt{2}\sigma$.

The whole construct (EF+hexagon) interacts with a fluid membrane modelled as a dynamically reconfigurable squared network of beads and springs. The liquid bilayer is represented as a $l \times l$ grid of N_m^2 point particles of size σ that are capable of moving only in the vertical direction. The edges of the membrane are kept fixed at $z = 0$. The Hamiltonian for the membrane is described by the Helfrich functional (73)

$$\mathcal{H}_m = \int \left(\frac{J_m}{2} (\nabla^2 h)^2 + \frac{\gamma}{2} (\nabla h)^2 \right) dxdy \tag{4.20}$$

where h is the local vertical distance with respect to the equilibrium position, J_m the bending modulus, γ the surface tension contribution and the integration runs over the area of the membrane. This Hamiltonian is the base-model to describe lipid bilayers, since such membranes are fluid in their lateral direction but resistant to stretching forces due to the hydrophobic effect. In this model we neglect the internal pressure P of the cell, since it has been shown that it makes only a trivial contribution (74).

The fact that the tips of the EFs cannot penetrate the membrane, couples the EFs energetically to the membrane. Starting from an initial condition in which the end of one of the chains is clamped, the simulation now proceeds as follows. An attempt is made to move one of the particles in the system (either a chain or a membrane bead). The proposed movement is accepted with a probability proportional to the Boltzmann weight of the associated change in energy of the whole system (including the energies associated with various constraints). This procedure is then repeated for several sweeps over all the particles in the system. This standard Metropolis Monte Carlo scheme allows the system to equilibrate its state to the current lengths of the individuals EFs. After this equilibration step, the gap between the tips of the EFs and the membrane is monitored for all the EFs. If this gap is larger than the size of a chain bead, a new bead is added at the tip, preserving the perpendicular orientation of the first bond. The system is then allowed to equilibrate again, and the whole cycle is repeated. Note that this algorithm is a microscopic implementation of a Brownian ratchet, in the case that the fluctuations are fast compared to the polymerization rate.

4.3.3.1 Results

The results of our simulation show that after initial effects have died down, a stationary regime is reached in which the CSC moves with a statistically stationary velocity in a direction dictated by the essentially straight CMF produced. This shows that indeed, the polymerization and crystallization processes, both exothermic, coupled by thermal fluctuations to the membrane and the partially flexible chains as energy transducers, are sufficient to obtain the directed motion of the synthase.

Fig. 4.11 shows four snapshots of our simulation at successive times. We note that although the trajectory of the CSC is approximately linear, the complex itself undergoes a rotation during its motion. This is caused by the helical nature of the crystalline structure of our pseudo-CMF, which is a natural consequence of the maximization of the binding energy. Intriguingly, cellulose microfibrils have also been observed experimentally to "twist" (75; 76), an effect generally attributed to the chirality of the planar glucan chains, which spontaneously “twist” to relieve the strain built around the oxygen bridge that holds the glucan together. Clear evidence of this phenomenon is given by the twisted cellulose ribbon produced by the *Acetobacter*, whose cells move undergoing a continuous rotation on their longitudinal axis: this is caused by the relieving of the stress induced by the non-linear crystallization of the nascent glucan chains during the biogenesis of the CMF (18). Also clearly visible in the side views of

Fig. 4.11 is the marked indentation of the membrane at the locus of CSC, over an area several times the area of the complex itself. This indentation is a consequence of the forces generated by the bent EFs, and has been observed experimentally (see Fig. 4.1 and (68)), and as such provides direct evidence in favour of our model.

4.4 Conclusions

The model proposed for the mechanism of the CSC propulsion in this chapter achieves three goals. First of all, on a conceptual level it provides an explicit and physically consistent heuristic for understanding CSC motion. Secondly, the analytical approach, which abstracts the model to its bare essentials, allows the observable result of the mechanism, i.e. the velocity of motion of the CSC, to be quantified in terms of the underlying physico-chemical parameters. Finally, our stochastic simulations, albeit simplified with respect to reality, provide a proof of principle of this mechanism. The fundamental assumption of the model, i.e. the microscopic fluctuations occur on timescale fast compared to that of the motion of the CSC, justifies the use of the coarse graining that underlies the analytical approach: this manages in replacing the many individual microscopic degrees of freedom with a small number of effective ones.

We contend that the biophysical model presented here provides a solid basis for understanding the propulsion of an individual CSC . Moreover, it gives an estimate for the polymerization velocity of the CMF that is consistent with the observed speed of the CSC within the uncertainty imposed by the approximations used. This opens the way for considering the much more challenging problem of understanding the full dynamics of cell wall deposition, which involves the simultaneous and apparently highly coordinated deposition of many CMFs. Indeed, the question of the origin of the highly regular CMF textures found in secondary cell walls is still actively debated. Whilst the textbook explanation involves the guidance of CSCs by ordered arrays of cortical microtubules (77), there is also a body of evidence against this idea, and a few models have been suggested that rely more strongly on the physical interactions between the CSCs and the CMFs they produce (see e.g (78; 79)). Clearly, all these approaches will benefit from a fuller understanding of the motive processes of the CSC in interaction with its direct environment.

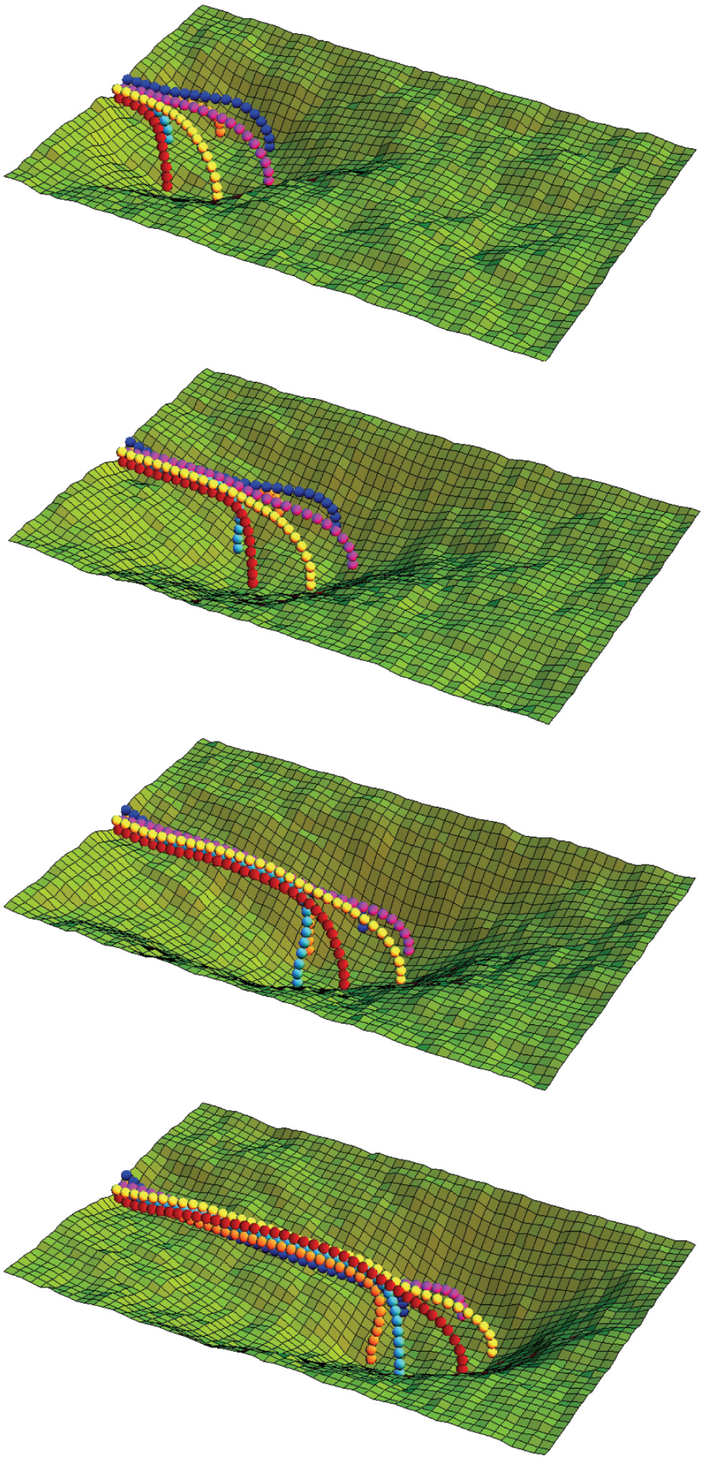

Figure 4.11: Snapshots at four different time points in a stochastic simulation of the motion of a six filament CSC. Note the rotation of the complex, induced by the helical nature of the crystalline arrangement in the CMF.

5 Modeling the architecture of the plant cell wall

As already pointed out in Chapter 4, plants found their structural stability on extra-cytoplasmic walls (cell wall) created by the cell. The rigidity of the cell wall serves a dual purpose: it protects the cell mechanically from the environment and provides a framework to support the turgor pressure which allows plants to raise themselves against gravity. The specific solution adopted by nature to obtain the required rigidity seems to be nearly universal (51): long cellulose microfibrils (CMFs), deposited in lamellar structures (80) and synthesized by protein complexes (CSCs) embedded in the plasma membrane (go to Chapter 4 for details). How the plant cell organizes these ordered textures around itself, creating its own protective environment, is a fascinating question. In this chapter we propose a geometrical mechanism for the orientation of the CMFs in the plasma membrane of plant cells. Our model explains the genesis of the complicated helicoidal texture and shows that the cell has intrinsic, versatile tools for creating a variety of textures.

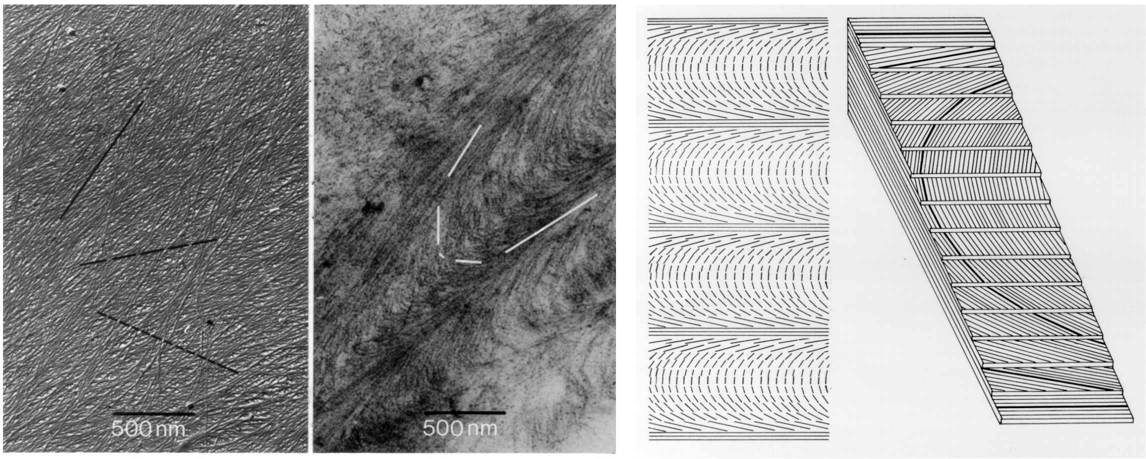

Figure 5.1: (a-b) EM images of the inner-side of the cell wall of a root hair of Equisetum Hymale showing the last three deposited lamellae; (c) Cartoon representing the arches typically observed in helicoidal cell walls

5.1 Genesis of the cell wall

Cell walls are made by apposition of new material from the side of the plasma membrane. This material is contained in Golgi vesicles that deliver their content into the existing cell wall after fusing with the plasma membrane. It is possible to distinguish two types of cell wall, depending on the developmental stage of the cell. The *primary cell wall* is deposited while the cell is still growing, and typically has a more disordered structure, with relatively short CMFs occurring with a random orientation distribution. The *secondary cell wall*, on the other hand, is deposited after the cell has stopped growing, or, in the case of tip growing cells such as root hairs, in the non expanding part of it.

The building blocks of plant cell walls are lamellae that are one-microfibril thick. Typically, secondary cell walls have surprisingly regular textures, with a constant orientation of the CMFs within each lamella. The global architecture of the cell is determined by the distribution of CMF orientation both between lamellae and with respect to the cell axis (81). The most striking of cell wall textures is the helicoidal wall, which is formed by lamellae in which the orientation of the CMFs changes by a constant angle from lamella to neighbouring lamella. This can be observed in surface preparations (Fig. 5.1.a) and gives rise to a characteristic pattern of arches in oblique sections (Fig. 5.1.b and 5.1.c) (82). Other wall textures are the axial, the transverse, the crossed-polylammelate, the helical, and the random wall textures, illustrated in Fig. 5.2, and combinations of these textures.

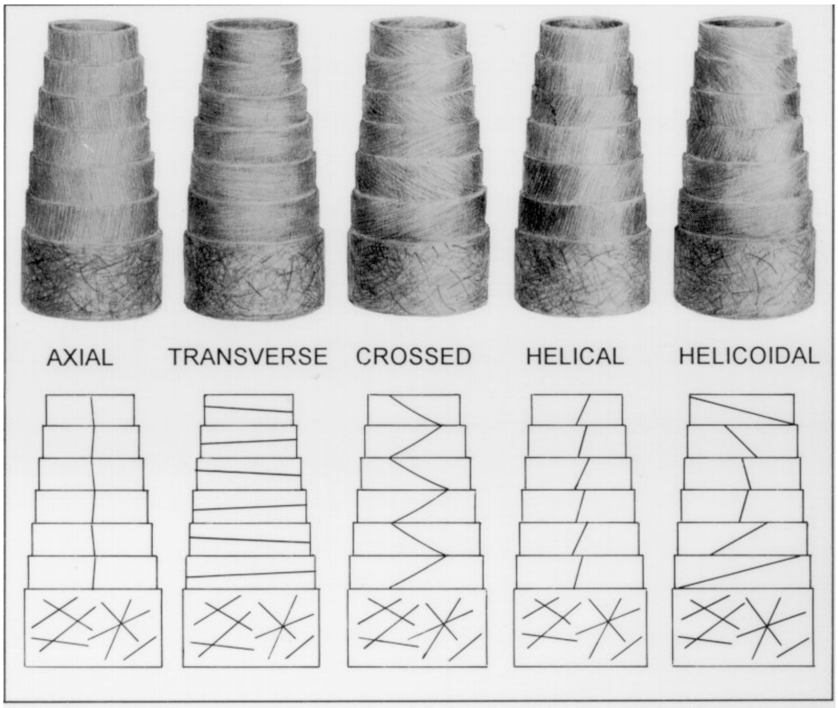

Figure 5.2: A collection of various ordered cell walls textures

Although the textures of plant cell walls have been the object of intense research effort, the question of the origin of these wall architectures still remains unanswered. There are two major schools of thought on the subject, one that believes that the structures arise from liquid crystalline self-organization (83) supposed to take place in a developmental phase prior to the final “setting” of the wall, i.e. an equilibrium effect, and one that adheres to the view that the structures are determined by the sequential growth-process of the CMFs itself (84), i.e. a mechanical, non-equilibrium effect. This latter school has to come to grips with two questions: since the growth history determines the structure, one needs to know (i) how the CMFs are actually created and (ii) how the cell can manipulate the orientations of the CMFs during (or after) their creation so as to result in the observed structures. On the first question a fair amount of consensus has been reached: CMFs are synthesized by so called particle rosettes (41) that are embedded in the cell plasma membrane and move pushed by the polymerization and crystallization forces (for a detailed explanation of this motion mechanism go to Chapter 4).

The second question is harder to answer. Several mechanisms for CMF orientation have been proposed of which guidance by cortical microtubules (85) is widely accepted for growing cells, but seems to be ruled out for walls deposited in non-elongating cells, where CMF orientations are not correlated to the microtubule arrangement (86)(81). Because these walls are nevertheless highly organized this mechanism cannot be considered a unique explanation for the observed structures.

A few years back, on the basis of extensive observations on the cell wall structure of *Equisetum Hymale* root hairs, Emons (87) put forward a theory based on the novel idea that fibril orientation is due to the restricted geometry in which the deposition process is taking place. This geometry is restricted in three ways. Firstly, the rosettes can only move inside the plasma membrane which limits their field of motion to that of the geometry of the 2d cell membrane. Secondly, the space in which the fibrils are deposited is extremely limited as they are apposed during formation against already formed primary or secondary wall material. Thirdly, it is observed that the average distance between adjacent CMFs within a lamella is a constant, independent of their orientation. It seems that the available space for deposition is optimally exploited, i.e. the fibrils (plus their adherent matrix material) are packed as densely as possible. Based on these observations, and on the idea that the long, cylindrically shaped, *Equisetum Hymale* root hairs can be mathematically represented by a perfect cylinder with radius R, Emons proposed the mechanism described in the next section.

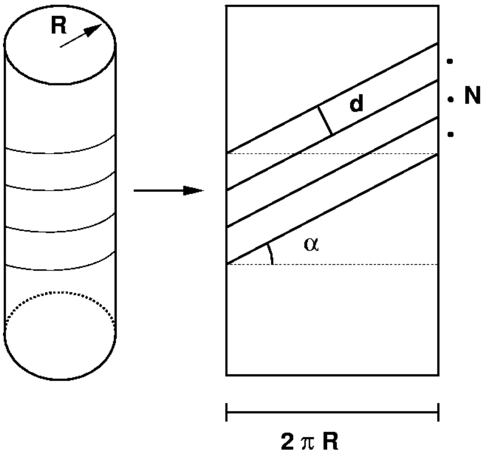

Figure 5.3: Cartoon illustrating the geometrical rule Eq. 5.1 by showing the path of N CMFs of effective width d on the unrolled cylindrical surface

5.2 The close-packing hypothesis

Consider a number N of rosettes in the plasma membrane simultaneously depositing fibrils with an effective width d (being d the width of the CMF plus adherent matrix material) at a certain position along the cell. It is assumed that the direction of motion of the rosettes is distal to proximal (tip-to-base), henceforth simply denoted as the ”plus-” and ”minus end” respectively . The deposited microfibrils left in the wake of the rosettes are apposed outside of the cylindrical plasma membrane on the inside of the already deposited wall material. Because this wall is deposited in a non-elongating tube, the once deposited CMFs remain in place, do not reorient, and therefore simply “record” the trajectory of the rosettes. Using the principle that the CMFs plus adherent matrix material pack as densely as possible, one arrives at a relation between the angle α a rosette trajectory makes with the tangent to any circular cross section of the cylinder that intersects this trajectory, and the number of CMFs being deposited.

$$\sin\alpha = \frac{Nd}{2\pi R} \tag{5.1}$$

This relation is most easily understood by unrolling the cylinder (Fig. 5.3).

This geometrical rule implies a coupling between the orientation of the newly deposited fibrils and the number of them that is being deposited, which by definition equals the number of active rosettes that are depositing them. Such a coupling provides the cell with a mechanism for manipulating the CMF orientations by controlling the number of active rosettes and/or the amount of wall matrix. Of course, for a given cell radius R, there is a maximum number of CMFs of effective width d that can be simultaneously deposited. This maximum is given by

$$N_* = \frac{2\pi R}{d} \tag{5.2}$$

corresponding to the fully axial deposition orientation of $\alpha = \pi/2$ radians.

5.3 The Geomodel

Based on the geometrical rule Eq. (5.1), some years ago Mulder *et al.* proposed a model that translated the close-packing hypothesis into a dynamical mathematical process (88). The model, which in the following will be denoted as *Geomodel*, describes the spatio-temporal dynamics of co-moving rosettes on the surface of cylindrical cells, and, provided some strict assumptions, is able to reproduce a great a variety of textures observed e.g. in *Equisetum Hymale* root hairs during development, including the helicoidal pattern (Fig. 5.4).

The aim of the present chapter is to test the robustness of this model under the relaxation of some of its main postulations. To achieve this task, we will proceed in the following way: we start with a general overview that provides a simple heuristic explanation of the dynamical process. Subsequently, we analyze in detail the basic ingredients necessary for the formulation of the space-time evolution equation proposed by Mulder *et al.*. Finally, we start constructing “variations” on the model, loosening some of the strict conditions imposed, and demonstrating that its solutions are still stable despite the introduction of such perturbations.

5.3.1 Insertion domains

The fundamental assumption at the basis of the Geomodel, is that creation of rosettes occurs in localized, but mobile, regions of the cell, which are called *insertion domains* (IDs). At present, there is some evidence for the spatial modulation of the rosette density, coming from plasma membrane surface preparations. However, to obtain a cell wall texture where the local angle of CMF deposition varies from lamella to lamella (e.g. the helicoidal wall), one must also assume that the rosette density is modulated in time. The concept of mobile IDs provides a mechanism to achieve the necessary modulation, both in space and in time. Each ID is thought to consist of active Golgi-bodies that produce Golgi vesicles. The vesicles, that carry rosettes in their membranes and contain cell wall matrix, are then incorporated into the cell plasma membrane by exocytosis, the usual membrane fusion mechanism.

The IDs are assumed to move with a constant velocity v in the plus (distal) direction. It is possible to envisage two mechanisms for the motion of the IDs: 1) The motion could be due to physical movement of patches of active Golgi bodies, caused e.g. by transport along the cytoskeleton; 2) The local activation of rosette insertion, by immobile Golgi bodies, could be switched on or off by travelling excitatory waves. One possible candidate are calcium waves, as Ca2+ is known to be involved in exocytosis (89). Such a mechanism also neatly provides for a train of IDs, which, as it will be shown later on, is necessary to describe cell wall textures that consist of repetitions of a basic structural motif e.g. the 'arches' of the helicoidal wall. Very recently such travelling chemical waves have been visualized directly for the first time in elongated cells (90).

5.3.2 Heuristic Mechanism

With the definition of the ID, it is now possible to give a complete picture of the life-cycle of a rosette according to the Geomodel. Rosettes, once inserted into the plasma membrane, travel towards the minus-end of the cell, i.e. in the direction opposite to that of the ID motion, leaving a CMF in their wake. The life cycle is illustrated in Fig.5.5a.

Consider what happens in the cell: at a given moment t a small number of rosettes is introduced into the plasma membrane. Once delivered, the complexes start producing the CMFs, which, given their small amount N, initially are deposited nearly transverse to the cylinder ($\alpha \sim 0$). At a next moment t' more rosettes are introduced into the plasma membrane, inside a domain which itself is moving in the direction of the cell tip. Some of the newly created rosettes encounter those already produced at t, causing a local increase of the angle of deposition α. Repeating this process, whereby earlier created rosettes encounter newly created ones along their trajectories, one can imagine successive lamellae being created with steadily increasing value of the angle α, the hallmark of the helicoidal structure. For a helicoidal pattern to be formed the angle should now continue to increase beyond $\alpha = \pi/2$ to eventually reach $\alpha = \pi$, when a full helix twist has been completed. This development is allowed for by the geometric rule Eq. (5.1), provided the number of rosettes decreases from the maximum value as soon as it is reached. Here the finite lifetime of the rosettes (or equivalently the finite length of the CMFs) comes into play as a mechanism for decreasing the number of active rosettes (or equivalently the number of CMFs being simultaneously deposited).

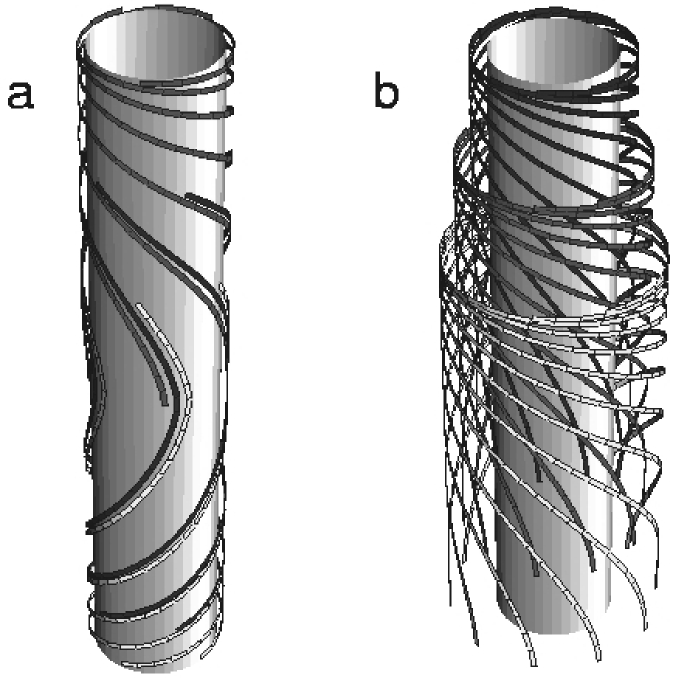

Figure 5.4: Two views of the helicoidal solution obtained in the geomodel representing: (a) three generations of CMFs co-deposited within the same ID at different times and locations; (b) three sets of CMFs originated at equally spaced time intervals at the same position within an ID

The process described above calls for individual CMFs to change their orientation continuously. The key point of the geometrical theory is the coupling of the rosette trajectories (and hence the orientation of the deposited CMFs) to the local number of active rosettes. This provides the cell with a route to manipulate the cell wall structure by creating controlled local variations of the number of active rosettes. It also gives a new interpretation to the lamellar structures observed in cell sections: lamellae are formed by stretches of CMFs deposited at different moments in time and different locations along the cell that happen to share the same orientation, rather than by a specific collection of CMFs that have a *constant* orientation throughout. In the new picture an individual CMF actually participates in many lamellae as its orientation changes during its deposition history. This relationship between individual CMFs and the resultant lamellar structure is depicted schematically in Fig. 5.5b. Actual sections only provide a local view of the structure and are therefore unable to reveal the global structure.

On the basis of this simple explanation, it is now possible to conduct a more detailed analysis on the evolution equation for the local density of rosettes as described in the Geomodel, by looking in turn at the creation, subsequent motion and final de-activation of rosettes.

5.3.3 Implementation of the dynamics

As stated in the introduction, the Geomodel is confined to cylindrical cells: the cell plasma membrane is thus chosen to be a perfect cylinder with radius R. Points on the cell are char-

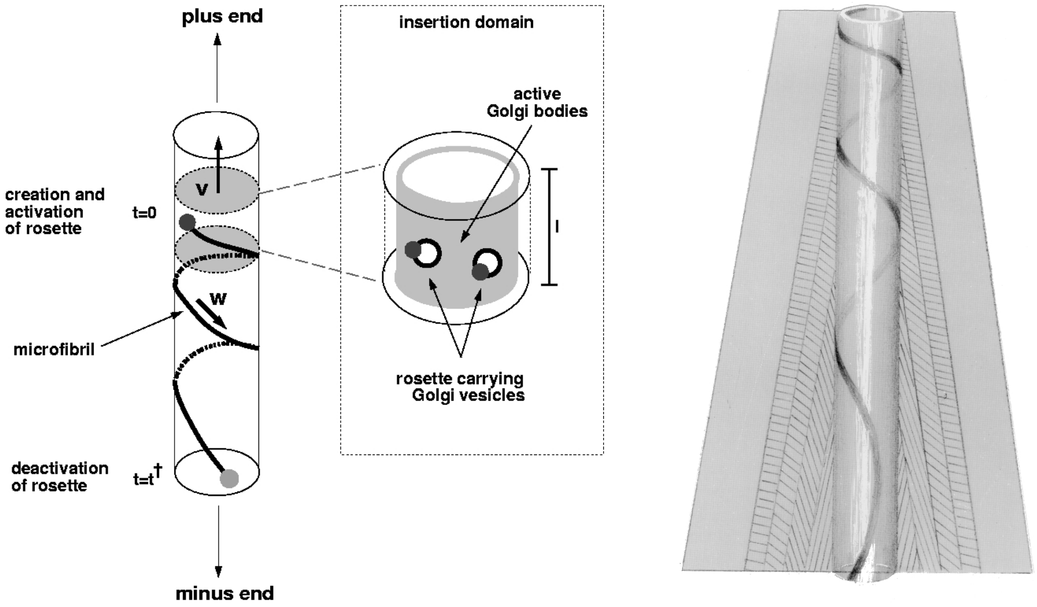

Figure 5.5: The life cycle of the rosette on the cylindrical cell surface

acterized by a coordinate z along the cell axis and an azimuthal angle ψ around the cell axis. The length of the cell is assumed to be infinite, an approximation justified for root hairs like those of *Equisetum Hymale* whose length can be order of a few mm's, whereas their diameter is of the order of a few tens of μm's. The "minus-end" and the "plus-end" of the cell are located respectively at $z = -\infty$ and at $z = \infty$. The source of the underlying polarity that allows this distinction (obvious in the case of tip-growing cells) is not specified. The thickness of the individual CMFs, equal to the amount by which the tube radius decreases per deposited lamella, is neglected. This approximation is allowed at least for the initial stages of secondary cell wall formation, when in *Equisetum hyemale* root hairs the radius is still in the order of 20 μn, whilst the thickness of a CMF is $\approx$ 4 nm (91). At a later stage of its development the radius of the plasma membrane can have shrunk considerably because of previous deposition. This leads to a changeover in cell wall texture (50), process that is successfully predicted by the Geomodel (88).

The maximum number of CMFs that can be simultaneously deposited is taken to be large, i.e. $N_* \gg 1$, reasonable since the width d of a CMF+adherent matrix material is also in the nm range. This condition allows to treat the number N as an essentially continuous variable. As it is assumed that CMFs are deposited uniformly along the circumference of the cell, and the cell itself is cylindrically symmetric, the local number of active rosettes $N(t,z)$ at a given position z along the cell at time t, is the fundamental dynamical variable of the geomodel, rather than the locations of all individual rosettes. This quantity is defined as follows. We identify each active rosette by a label $r \in \mathcal{R}(t)$, being the set of active rosettes at time t. The location of a given active rosette is specified through its coordinates $(z_r(t), \psi_r(t))$. The set of locally active rosettes is then defined through

$$\mathcal{R}(t,z) = \left\{ r \in \mathcal{R}(t) | z - \frac{1}{2}\delta z < z_r(t) < z + \frac{1}{2}\delta z \right\} \tag{5.3}$$

where δz is an infinitesimal averaging interval. The local number of active rosettes is then simply given by $N(t,z) = |\mathcal{R}(t,z)|$.

In the following we will adopt the slightly imprecise, but more convenient, nomenclature, *(local) rosette density* for $N(t,z)$, and we will use the word "particle" as a synonym for rosette.

5.3.3.1 Motion of rosettes

We now consider the influence that, according to the geomodel, the motion of the individual rosette has on the evolution of the rosette density $N(t,z)$. We assume for the moment that the absolute value of the velocity of a moving particle is equal to a constant w. The equation of motion for the position of a rosette along the cell is obtained by applying the geometrical rule Eq. (5.1) locally

$$\dot{z}_r(t) = -w \sin \alpha_r(t) = -\frac{wd}{2\pi R} N(t, z_r(t)) = -w \, \frac{N(t, z_r(t))}{N_*} \tag{5.4}$$

where the minus sign is the consequence of our assumption of plus-to-minus end motion of the rosettes. For the moment we disregard all processes that increase or decrease the total number of particles. Consider the set of locally active rosettes $\mathcal{R}(t,z)$. By definition all particles in this set have axial velocity $\dot{z}_{r \in \mathcal{R}(t,z)}(t) = -\frac{wd}{2\pi R} N(t,z)$. A time interval $\frac{\delta z}{w} \ll \Delta t \ll 1$ later all rosettes in $\mathcal{R}(t,z)$ will thus have moved over a distance $\Delta z = -\frac{wd}{2\pi R} N(t,z)\Delta t + O\left(\Delta t^2\right)$ so that $\mathcal{R}(t,z) \simeq \mathcal{R}(t+\Delta t, z - \frac{wd}{2\pi R} N(t,z)\Delta t)$, or equivalently $N(t,z) \simeq N(t+\Delta t, z - \frac{wd}{2\pi R} N(t,z)\Delta t)$. Expanding the right hand side to first order in Δt then yields the following quasi-linear PDE describing the conserved evolution of the rosette density

$$\frac{\partial N(t,z)}{\partial t} - \frac{wd}{2\pi R} N(t,z) \frac{\partial N(t,z)}{\partial z} = 0. \tag{5.5}$$

5.3.3.2 Constructing the complete evolution equation

The left hand side of Eq. (5.5) represents the ”kinematical” part that describes the motion of the rosettes with an axial speed proportional to their density. However, if we also want to allow for creation and de-activation of rosettes, we have to add in the equation a further "dynamical" term to take into account the sources of change of the rosette density. This is done by introducing at the right hand side of Eq. (5.5) a birth rate function $f(t,z)$ and a de-activation rate function $f^{\dagger}(t,z)$, that, for the moment, we leave in the most general form. The final evolution equation for the rosette density then becomes:

$$\frac{\partial N(t,z)}{\partial t} - \frac{wd}{2\pi R} N(t,z) \frac{\partial N(t,z)}{\partial z} = f(t,z) - f^{\dagger}(t,z). \tag{5.6}$$

This PDE is the core of the geomodel: from the solutions of this equation it is possible to obtain the trajectories of the rosettes on the cell membrane, and consequently the patterns emerging from the orientation of the deposited CMFs.

In order to consistently solve Eq. (5.6), one needs to specify the exact mathematical form of the birth and death rate functions $f(t,z)$ and $f^{\dagger}(t,z)$. For what concerns the first one, since there is a maximum allowed number of active rosettes, given by Eq. (5.2), one must allow for the existence of a feedback mechanism that controls the rate at which active rosettes are created, so as to preclude this maximum from being surpassed. The choice of a specific rate function $f(t,z)$, is then guided by a few operational requirements: (i) it should depend only on the local density (ii) it allows the maximum density to be reached from zero in a finite time t_* (iii) it does *not* allow the maximum density to be surpassed.

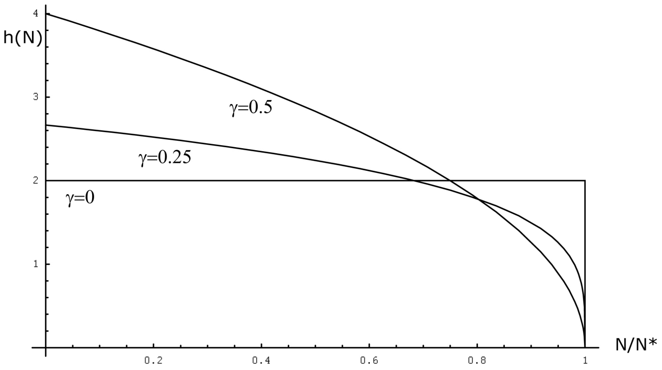

Figure 5.6: Birth rate function adopted in the geomodel for different values of γ

Moreover, as stated in the previous section, creation of rosettes must occur only in specific regions on the cell, the IDs, that move themselves with a velocity v. Therefore, the general form of the birth rate function will be:

$$f(t,z) = g(z - vt)h(t,z)$$

where $h(t,z)$ is a local production rate that has to satisfy the three requirements discussed above, while $g(z - vt)$ is a modulating function that depends on the specific choice of the ID shape: typically it is peaked around $z = vt$ and vanishes outside a domain characterized by a width l.

The production rate function that was chosen in the Geomodel reads like:

$$h(t,z) = \frac{N_*}{t_*(1-\gamma)}\left(1 - \frac{N(t,z)}{N_*}\right)^{\gamma}\theta(N_* - N(t,z)) \tag{5.7}$$

where t_* is the time necessary to build up to the maximum density N_*, $0 \leq \gamma < 1/2$ is a parameter that determines the shape of the production rate of particles, and $\theta(x)$ is a standard Heavyside step function. The particular situation $\gamma = 0$ describes the limiting case of a constant rate with an infinitely sharp cut-off (Fig. 5.6).

For what concerns the shape of the ID, the geomodel assumes it to be simply a cylindrical region along the cell, so that

$$g(z-vt)=\theta(vt+z(0)-z)\,\theta(z-(vt+z(0)-l))$$

where l is the length of the ID and $z(0)$ is the location of its front (plus-end) at $t=0$.
The final form of the birth rate function then becomes:

$$\begin{aligned} f(t,z) &= \frac{N_*}{t_*(1-\gamma)}\left(1-\frac{N(t,z)}{N_*}\right)^{\gamma}\theta(N_*-N(t,z))\times && (5.8)\\ & \quad \theta(vt+z(0)-z)\,\theta(z-(vt+z(0)-l)). && (5.9)\end{aligned}$$

Fig. 5.7 shows the behaviour of $f(t,z)$ along the cell in the particular case in which $\gamma=0$. In order to consistently describe repetitive wall textures, the model needs also to assume that a whole train of IDs can be present along the cell. To decouple the contributions of the individual IDs, which are labeled with successive integers according to their arrangement, we simply have to require that $z_i(0)-z_{i+1}(0)>l$, for all i.

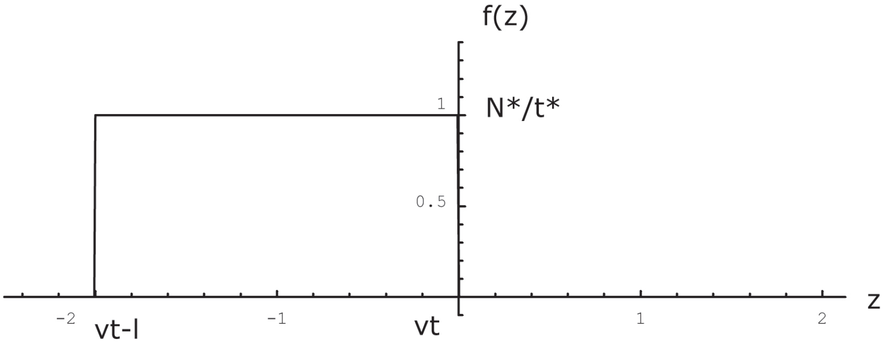

Figure 5.7: Square wave ID (birth rate function for $\gamma=0$)

Regarding the deactivation of rosettes, the Geomodel consider them to have a constant finite lifetime $t^{\dagger}$. The rate at which they are deactivated at time t and position z therefore depends on the number of rosettes (if any) created at $t-t^{\dagger}$ that reach the location z at time t. The deactivation rate at (t,z) than equals the creation rate at $(t-t^{\dagger},z^{\dagger}(t,z))$, where we have indicated by $z^{\dagger}(t,z))$ the position that a virtual rosette should have had in order to arrive at z at time t. Therefore,

$$f^{\dagger}(t,z)=f(t-t^{\dagger},z^{\dagger}(t,z)). \qquad (5.10)$$

5.3.3.3 Dimensionless Equation

To solve Eq. (5.6) with the activation rate given in Eq. (5.9), it is convenient to introduce a set of dimensionless variables and constants into the model. This is done by adopting t_*, wt_*

and N_* as our units of time, length and density respectively. We are left then with the reduced independent time, space and density variables

$$\tau = \frac{t}{t_*} \qquad \zeta = \frac{z}{wt_*} \qquad \nu = \frac{N}{N_*}. \tag{5.11}$$

The dimensionless parameters of the model are therefore

$$\lambda = l/(wt_*) \qquad \beta = v/w \qquad \tau^\dagger = t^\dagger/t_* \tag{5.12}$$

and the evolution equation (5.6) becomes

$$\frac{\partial\nu(\tau,\zeta)}{\partial\tau} - \nu(\tau,\zeta)\frac{\partial\nu(\tau,\zeta)}{\partial\zeta} = \phi(\tau,\zeta) - \phi^\dagger(\tau,\zeta) \tag{5.13}$$

where

$$\phi(\tau,\zeta) = \frac{(1-\nu(\tau,\zeta))^\gamma}{1-\gamma}\Theta(1-\nu(\tau,\zeta))\Theta(\beta\tau-\zeta)\Theta(\zeta-(\beta\tau-\lambda)) \tag{5.14}$$

and

$$\phi^\dagger(\tau,\zeta) = \phi(\tau-\tau^\dagger,\zeta^\dagger(\tau,\zeta)).$$

We will return to the problem of self consistently determining $\zeta^\dagger(\tau,\zeta))$ when we construct the solutions of the evolution equation using the method of characteristics.

5.3.3.4 Method of solution

In order to solve Eq. (5.13) we apply the method of characteristics. The details of this method of solution are reported in Appendix. Since we wish to study the solutions of the evolution equation in absence of any transient or boundary related effects, we assume that cell wall deposition has started sufficiently long ago that all transient effects have died down: we are essentially in a steady state in which IDs from a long train are passing the origin (middle of the cell) at regular intervals. The zero of our timescale is now arbitrarily chosen such that at $\tau = 0$, the front of a new ID is located at $\zeta = 0$. The rosettes created in this ID will for $\tau > 0$ start spinning CMFs that will contribute to a new lamella being deposited in the regime $\zeta > 0$.

The equations for the characteristics, which are parametrized by the variable s and identified by the initial value parameter p, follow directly from Eq. (5.13)

$$\begin{aligned} \frac{d\tau(s;p)}{ds} &= 1 && (5.15)\\ \frac{d\zeta(s;p)}{ds} &= -\nu(s;p) && (5.16)\\ \frac{d\nu(s;p)}{ds} &= \phi(s;p) - \phi^\dagger(s;p) && (5.17) \end{aligned}$$

with initial conditions

$$\begin{aligned} \tau(0;p) &= 0 && (5.18)\\ \zeta(0;p) &= p && (5.19)\\ \nu(0,p) &= 0. && (5.20) \end{aligned}$$

From the trivial equation Eq. (5.15), it is possible to directly eliminate the parameter s in favour of the time τ, and we will do so in the following. We first note that Eq. (5.16) is just the dimensionless form of the original equation Eq. (5.4) describing the motion along the cell of a single rosette. The full path over the cell surface of the rosette can therefore be reconstructed by considering the extended characteristics $\vec{\sigma}(\tau;p) = (\rho\cos\psi(\tau;p), \rho\sin\psi(\tau;p), \zeta(\tau;p))$, where the dimensionless cell radius is given by $\rho = R/wt_*$. The equation of motion for the azimuthal angle $\psi(\tau;p)$ is readily derived from the constancy of the speed w of the rosette, which in dimensionless form becomes

$$\frac{d\vec{\sigma}(\tau;p)}{d\tau}\cdot\frac{d\vec{\sigma}(\tau;p)}{d\tau} = \rho^2\left(\frac{d\psi(\tau;p)}{d\tau}\right)^2 + \left(\frac{d\zeta(\tau;p)}{d\tau}\right)^2 = 1. \tag{5.21}$$

Combining with Eq. (5.16), yields

$$\rho\frac{d\psi(\tau;p)}{d\tau} = \left(1-\nu^2(\tau;p)\right)^{\frac{1}{2}} \tag{5.22}$$

showing how $\psi(\tau;p)$ can be obtained from the characteristics. Since the track of a rosette completely determines the configuration (position and orientation) of a CMF being deposited, any arc of length $\tau^\dagger$ along the extended characteristic can now be identified with an actual CMF.

5.3.3.5 The helicoidal solution

Before describing in detail the mathematical conditions that lead to the occurrence of the helicoidal solution, we first recall how the helicoidal texture looks like: a transverse section of the cell wall shows an increasing orientation of the CMFs, starting form the transverse one ($\alpha = 0$), then reaching the axial direction ($\alpha = \pi/2$)) and eventually completing a full turn ($\alpha = \pi$). This geometrical description can be explained in terms of the solution of the equation, since we know that the characteristic can be identified with a CMF strand.

For example, the fact that the CMF must cross the value $\alpha = \pi/2$ means that the density must reach its maximum value $\nu = 1$. Moreover, since in a helicoidal pattern no significant patches of purely axial orientation occur, the density must immediately decrease again after the maximum has been reached, implying that from that point on no more rosettes may be created and only deactivation may occur. This condition has two main consequences: on one hand it immediately fixes the rosette lifetime, which has to be equal to the time to build up to the maximum density, which is in fact our unit of time, so that $\tau^\dagger = 1$; on the other hand, the fact that for $\tau > \tau^\dagger = 1$ only deactivation occurs implies that the characteristic has to cross the bottom of the domain exactly when $\tau = 1$.

On the basis of the above discussion we can therefore divide the evolution along the characteristic in two main phases:

Phase I	$0 \le \tau < \tau^\dagger = 1$	(only creation of rosettes occurs)
Phase II	$1 \le \tau < \tau_d$	(only de-activation of rosettes occurs)

where we have indicated by τ_d the time at which deactivation of rosettes stops.

We now construct the solution along a generic characteristic, labelled, for sake of simplicity, by the initial value parameter $p = 0$. In the first phase creation of rosette occurs at the rate given by Eq. (5.14), and de-activation is absent. The resultant equations (5.16) and (5.17) can be easily integrated to give:

$$\begin{aligned} \nu_{\mathrm{I}}(\tau) &= 1-(1-\tau)^{\frac{1}{1-\gamma}} && (5.23)\\ \zeta_{\mathrm{I}}(\tau) &= -\tau+\frac{1-\gamma}{2-\gamma}(1-(1-\tau))^{\frac{2-\gamma}{1-\gamma}}. && (5.24)\end{aligned}$$

Having obtained this solution, we are now in position to determine the constraints that have to be satisfied in order for the helicoidal solution to exist. First of all, the characteristic has to cross the bottom of the ID as soon as the maximum density is reached (i.e. when $\tau = 1$): this implies that $\zeta_{\mathrm{I}}(1) = \beta-\lambda$, yielding to the condition

$$\lambda = \beta + \frac{1}{2-\gamma} \tag{5.25}$$

that links the size of the ID to its speed along the cell. Moreover, we also know that the last rosettes created are the ones which were born just before the exit from the ID, i.e. the time $\tau = 1$. Since these rosettes are the last to be deactivated, and they have a fixed lifetime $\tau^{\dagger} = 1$, we have to respect the further condition $\tau_d = 1+\tau^{\dagger} = 2$.

In the second phase of the evolution equation, only deactivation takes place, and the density satisfies the equation:

$$\frac{d\nu_{\mathrm{II}}}{d\tau} = -\frac{(1-\nu_{\mathrm{I}}(\tau-1))^{\gamma}}{1-\gamma} \tag{5.26}$$

that again is easily integrated to yield

$$\begin{aligned} \nu_{\mathrm{II}}(\tau) &= (2-\tau)^{\frac{1}{1-\gamma}} && (5.27)\\ \zeta_{\mathrm{II}}(\tau) &= -1+\frac{1-\gamma}{2-\gamma}(2-\tau)^{\frac{2-\gamma}{1-\gamma}}. && (5.28)\end{aligned}$$

Putting together Eq. 5.24 and Eq. 5.28 one obtains the final helicoidal solution shown in Fig. 5.8. As one can see, during the "creation phase" the characteristic passes through a regime in which $\nu(\tau)$ increases and $\zeta\tau$ decreases. However, after a time $\tau = 1$ the second phase begins, $\zeta(\tau)$ continues to decrease but the density $\nu(\tau)$ goes back to zero. As already said, from the behaviour of $\nu(\tau)$ it is also possible to extract information on the angle of deposition $\alpha(\tau)$: in fact from Eq. (5.4) it follows that $\alpha(\tau) = \arcsin[\nu(\tau)]$. One thing that should be noted, however, is that in order to consistently interpret the decrease of the density away from the maximum as an increase of the angle $\alpha(\tau)$,the inverse of the post-maximum density has to be chosen as:

$$\alpha(\tau) = \pi - \arcsin[\nu(\tau)] \qquad \tau > \tau^{\dagger}. \tag{5.29}$$

Plotting the solutions for $\alpha(\tau)$ one obtains the behaviour shown in Fig. 5.9: as expected, the angle of deposition is continuously increasing, form o to π. To better visualize the helicoidal solution, we can plot also the extended characteristic $\psi(\tau)$ on the surface of the cylinder: Fig. 5.4 shows this solution for values of the parameter $\gamma = 0$ and $\beta = 0.5$.

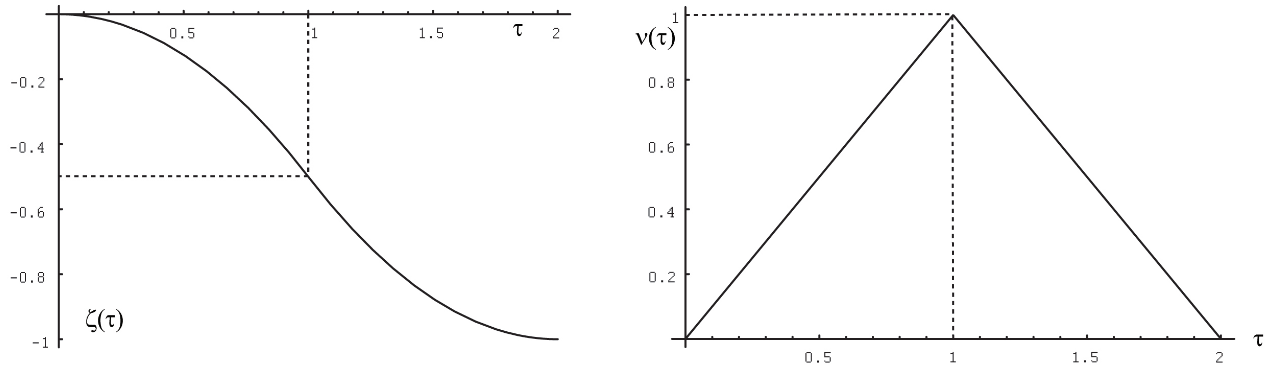

Figure 5.8: $\zeta(\tau)$ and $\nu(\tau)$: the original helicoidal solution

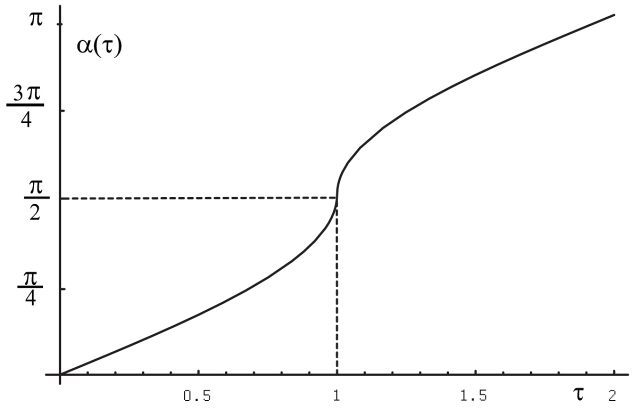

Figure 5.9: Solution for $\alpha(\tau)$ as found in the geomodel

5.4 Testing the robustness of the Geomodel

Solving Eq. (5.6) with the activation and de-activation rate functions discussed in the previous sections, led to solutions that were able to reproduce a number of variety of textures, including the helicoidal pattern as just demonstrated. Our goal in this section is to check whether the same solutions still hold when some of the main assumptions of the model are loosened. This is essential, because one of the biggest limitations of the Geomodel is the non-complete flexibility of its underlying requirements. We therefore need to consider to which extent the theory presented in the model is actually able to deal with real life uncertainties. In the following we are going to "perturb" the postulations at the basis of the Geomodel in three different ways: 1) we change the shape of the ID, passing from the homogeneous cylindrical cell segment to a more complex, modulated in space, production wave; 2) we allow for a non fixed distribution of the life time of the rosettes; 2) we introduce fluctuations in the birth rate, constructing a new geometrical mechanism that allows for the maximum number N_* of simultaneously deposited rosettes to be surpassed. In all these three cases we demonstrate that the solutions of the geomodel are still stable and that the helicoidal pattern can be obtained as well.

5.4.1 The Triangular birth rate function

We start analyzing the effect that a spatially inhomogeneous birth rate has on the solutions of the Geomodel. Consider a constant production rate

$$h(t,z) = \frac{f_*}{l}\,\Theta(N_* - N(t,z)) \tag{5.30}$$

associated with a triangular modulating function

$$g(z-vt) = (vt-z)\Theta(vt-z)\,\Theta(z+l-vt) + (z-vt+2l)\Theta(vt-l-z)\,\Theta(z-vt+2l).$$

The final birth rate function then becomes:

$$f(t,z) = \begin{cases} \frac{f_*}{l}\,(vt-z)\,\Theta(N_* - N(t,z)) & \text{if } vt-l < z < vt, \\ \frac{f_*}{l}\,(z-vt+2l)\,\Theta(N_* - N(t,z)) & \text{if } vt-2l < z < vt-l. \end{cases}$$

and its behaviour is depicted schematically in Fig. 5.10. Here the ID has a total length $2l$ and travels towards the cell plus end with a constant velocity v. The rosettes have a finite life-time $t^\dagger$ and their rate of creation is not uniform along the domain but reaches its maximum value f^* whenever $z = vt - l$ (provided of course that $N(t,z) < N_*$).

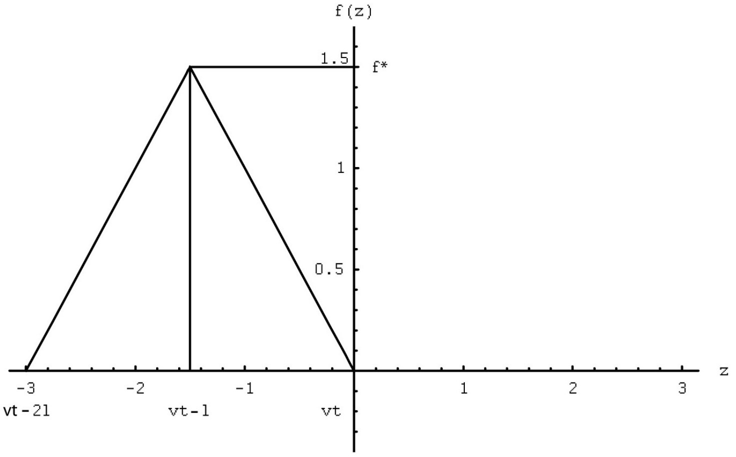

Figure 5.10: Triangular local rate of production

In order solve Eq. (5.6) with this new activation rate, we again non-dimensionalize adopting $t_* = N_*/f_*$, wt_* and N_* as our units of time, length and density respectively. With these new parameter the shape of the birth rate is described by the function

$$\phi(\tau,\zeta) = \begin{cases} \frac{1}{\lambda}\,(\beta\tau-\zeta)\,\Theta(1-\nu(\tau,\zeta)) & \text{if } \beta\tau-\lambda < \zeta < \beta\tau, \\ \frac{1}{\lambda}\,(\zeta-\beta\tau+2\lambda)\,\Theta(1-\nu(\tau,\zeta)) & \text{if } \beta\tau-2\lambda < \zeta < \beta\tau-\lambda. \end{cases}$$

where again

$$\phi^\dagger(\tau,\zeta) = \phi(\tau-\tau^\dagger, \zeta^\dagger(\tau,\zeta)).$$

5.4.1.1 Helicoidal texture

We start studying the solution along a characteristic labelled by the initial value parameter $p = 0$. For the considerations carried out previously, we know that in order to have the helicoidal solution, deactivation of rosettes has to begin exactly when creation stops, because the angle of deposition α has to decrease as soon as its maximum value $\pi/2$ is reached. This implies that the maximum number of active rosettes must be reached as soon as the characteristic crosses the bottom of the ID. The evolution along the characteristic can be divided in four phases:

Phase I	$0 \leq \tau < \tau_1$	(passage of first region of triangular domain - negative slope)
Phase II	$\tau_1 \leq \tau < \tau_2$	(passage of second region triangular domain - positive slope)
Phase III	$\tau_2 \leq \tau < \tau_1 + \tau_2$	(death of rosette born during Phase I)
Phase IV	$\tau_1 + \tau_2 \leq \tau < 2\tau_2$	(death of rosette born during Phase II)

Phase I and II: In the first phase creation of rosettes is due to the passage of the first region of the triangular domain, and deactivation is absent. The governing equations are therefore:

$$\frac{d\zeta_{\mathrm{I}}}{d\tau} = -\nu_{\mathrm{I}}(\tau) \tag{5.31}$$

$$\frac{d\nu_{\mathrm{I}}}{d\tau} = \frac{1}{\lambda}(\beta\tau - \zeta_{\mathrm{I}}(\tau)) \tag{5.32}$$

with initial conditions

$$\zeta_{\mathrm{I}}(0) = 0 \tag{5.33}$$

$$\nu_{\mathrm{I}}(0) = 0. \tag{5.34}$$

The above system is easily integrated and gives

$$\zeta_{\mathrm{I}}(\tau) = \beta\left(\tau - \sqrt{\lambda}\,\sinh\left[\frac{\tau}{\sqrt{\lambda}}\right]\right) \tag{5.35}$$

This solution is valid until a time $\tau_1 = \sqrt{\lambda}\,\operatorname{asinh}\left[\frac{\sqrt{\lambda}}{\beta}\right]$, where the variable τ_1 satisfies the condition $\zeta_{\mathrm{I}}(\tau_1) = \beta\tau_1 - \lambda$. At this time, in fact, the characteristic $\zeta_{\mathrm{I}}(\tau)$ crosses the region of the triangular domain with a negative slope. In this second phase deactivation is still absent, and the equations read like:

$$\frac{d\zeta_{\mathrm{II}}}{d\tau} = -\nu_{\mathrm{II}}(\tau) \tag{5.36}$$

$$\frac{d\nu_{\mathrm{II}}}{d\tau} = \frac{1}{\lambda}(2\lambda - \beta\tau + \zeta_{\mathrm{II}}(\tau)) \tag{5.37}$$

with initial conditions:

$$\zeta_{\mathrm{II}}(\tau_1) = \zeta_{\mathrm{I}}(\tau_1) \tag{5.38}$$

$$\nu_{\mathrm{II}}(\tau_1) = \nu_{\mathrm{I}}(\tau_1). \tag{5.39}$$

These equations are again easily integrated and we obtain:

$$\zeta_{II}(\tau) = -2\lambda + \beta\tau + \lambda\cos[g(\tau)] - \sqrt{\lambda(1+\frac{\lambda}{\beta^2})}\beta\sin[g(\tau)] \tag{5.40}$$

where

$$g(\tau) = \left(\frac{\tau}{\sqrt{\lambda}} - \text{arccsch}\left[\frac{\beta}{\sqrt{\lambda}}\right]\right).$$

At this point we can determine the conditions that have to be satisfied to obtain the helicoidal solution. First of all, we know that the characteristic crosses the bottom of the triangular ID when $\zeta_{II}(\tau_2) = \beta\tau_2 - 2\lambda$. This identifies the time τ_2, that results to be $\tau_2 = \sqrt{\lambda}\left(\arccos\left[\sqrt{\frac{\lambda+\beta^2}{2\lambda+\beta^2}}\right] + \text{arccsch}\left(\frac{\beta}{\sqrt{\lambda}}\right)\right)$. As already discussed, in order for the helicoidal solution to exist, we require the characteristic to exit from the ID exactly when the maximum density is reached. This means that $\nu_{II}(\tau_2) = -\zeta'_{II}(\tau_2) \equiv 1$, yielding to the condition:

$$\lambda = \beta + \frac{1}{2} \tag{5.41}$$

that links the size of the ID to its speed along the cell. It has to be noted that this relation is equal to the one found in the Geomodel (Eq. 5.25) for the squared ID ($\gamma = 0$), with the only difference that in this case the total length of the domain is 2λ instead of λ.

Phases III and IV: In the third phase only deactivation of rosettes can take place, because the characteristic is already out of the ID. Since the density must immediately decrease again after the maximum has been reached, the lifetime of a rosette has to be equal to the time at which creation stops. That means that

$$\tau^{\dagger} = \tau_2 \tag{5.42}$$

and the equations for the characteristics read like:

$$\begin{aligned} \frac{d\zeta_{III}}{d\tau} &= -\nu_{III}(\tau) && (5.43)\\ \frac{d\nu_{III}}{d\tau} &= -\frac{1}{\lambda}[\beta(\tau-\tau_2) - \zeta_I(\tau-\tau_2)] && (5.44) \end{aligned}$$

for $0 < \tau - \tau_2 < \tau_1$, and:

$$\begin{aligned} \frac{d\zeta_{IV}}{d\tau} &= -\nu_{IV}(\tau) && (5.45)\\ \frac{d\nu_{IV}}{d\tau} &= -\frac{1}{\lambda}[2\lambda - \beta(\tau-\tau_2) + \zeta_{II}(\tau-\tau_2)] && (5.46) \end{aligned}$$

for $\tau_1 < \tau - \tau_2 < \tau_2$.

The initial conditions are respectively:

$$\begin{aligned} \zeta_{III}(\tau_2) &= \zeta_{II}(\tau_2) && (5.47)\\ \nu_{III}(\tau_2) &= \nu_{II}(\tau_2) && (5.48) \end{aligned}$$

and

$$\begin{aligned} \zeta_{\mathrm{IV}}(\tau_1+\tau_2) &= \zeta_{\mathrm{III}}(\tau_1+\tau_2) && (5.49)\\ \nu_{\mathrm{IV}}(\tau_1+\tau_2) &= \nu_{\mathrm{III}}(\tau_1+\tau_2). && (5.50) \end{aligned}$$

Solving the first equation we obtain:

$$\zeta_{\mathrm{III}}(\tau) = -2\lambda - (\tau-\tau_2)\sqrt{2\lambda+\beta^2} + \beta\tau_2 + \sqrt{\lambda}\,\beta\sinh\left[\frac{\tau-\tau_2}{\sqrt{\lambda}}\right] \tag{5.51}$$

while for the second equation:

$$\begin{aligned} \zeta_{\mathrm{IV}}(\tau) = \beta\tau_2 - (\tau-\tau_2)\sqrt{2\lambda+\beta^2} - \sqrt{\lambda(\lambda+\beta^2)}\cos[h(\lambda,\beta)] + \arcsin[h(\lambda,\beta)] && (5.52)\\ -\lambda\sin\left[2g(\tau) - \frac{\tau}{\sqrt{\lambda}} + \arcsin[h(\lambda,\beta)]\right] && (5.53) \end{aligned}$$

where $h(\lambda,\beta) = \sqrt{\frac{\lambda+\beta^2}{2\lambda+\beta^2}}$.

5.4.1.2 Visualization of solutions

The complete characteristic is obtained summing up the contributions of the four solutions just found, each defined only in its particular time range, as discussed in the previous section. We have therefore:

$$\zeta(\tau) = \zeta_{\mathrm{I}}(\tau) + \zeta_{\mathrm{II}}(\tau) + \zeta_{\mathrm{III}}(\tau) + \zeta_{\mathrm{IV}}(\tau) \tag{5.54}$$

Again, from the behaviour of $\zeta(\tau)$ we can extract information on the density $\nu(\tau)$ and on the angle of deposition $\alpha(\tau)$. From Eq. (5.16) in fact we have that $\nu(\tau) = -\zeta'(\tau)$, while from Eq. (5.4) it follows that $\alpha(\tau) = \arcsin[\nu(\tau)]$.

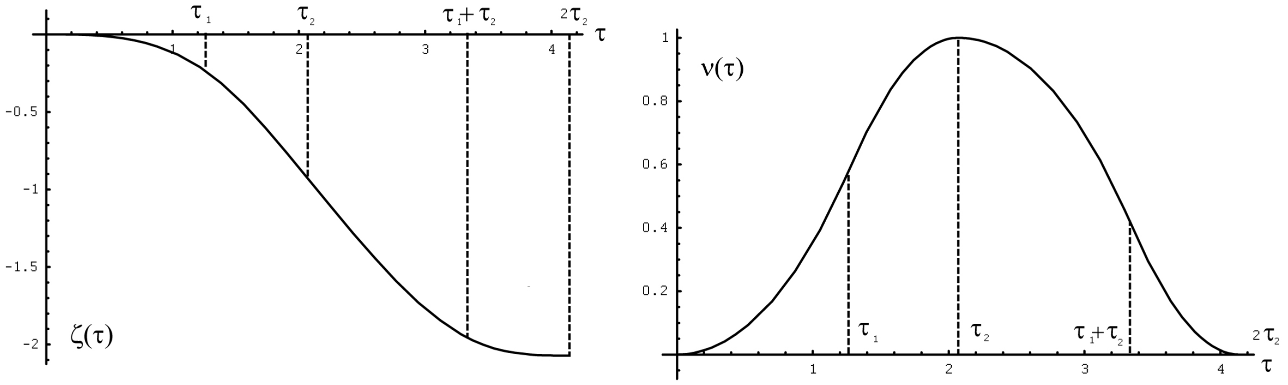

Figure 5.11: $\zeta(\tau)$ and $\nu(\tau)$ for the "triangular ID" case

Fig. 5.11 and Fig. 5.12 show the behaviour of the three relevant quantities $\zeta(\tau)$, $\nu(\tau)$ and $\alpha(\tau)$. The pictures illustrate that the "triangular ID" case discussed in this section reproduces well the helicoidal solution examined in the Geomodel: once assumed the post maximum solution to be

$$\alpha(\tau) = \pi - \arcsin[\nu(\tau)] \qquad \tau > \tau_2.$$

we have that the angle of deposition $\alpha(t)$ in fact is continuously increasing until the value $\alpha = \pi$.

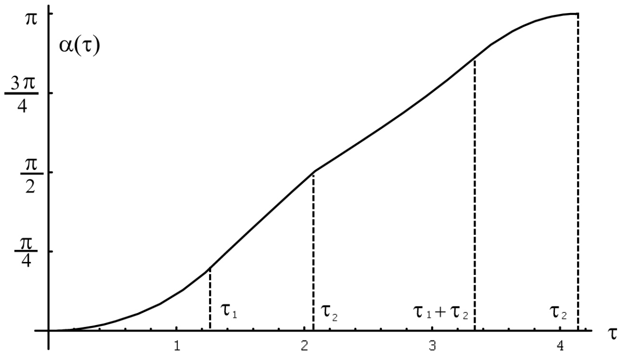

Figure 5.12: $\alpha(t)$ for the “triangular ID” case

5.4.2 Aging

The next step to test the robustness of the geomodel is to allow for a non-constant life time of the rosettes. In order to do this, we need to introduce the concept of “age”: let therefore $n(\mu;z,t)\,d\mu$ denote the number of synthases of age μ per unit length at position z at time t. From this definition it follows that

$$N(z,t) = \int_0^\infty d\mu\, n(\mu;z,t) \tag{5.55}$$

is the total number of synthases per unit length at position z and time t. Our goal in this section is to build up a structured population version of the evolution equation for the rosette density and to resume the same solutions already found in the Geomodel.

5.4.2.1 The evolution equation

We begin recovering Eq. (5.5) starting from the dynamics of this new variable. In the absence of “birth” and “death” processes the equation of motion for $n(\mu;z,t)$ can be derived as follows: in a small time interval dt the sub population $n(\mu;z,t)$ ages by dt and moves down the cell over a distance $dz = -\frac{wd}{2\pi R}N(z,t)\,dt$, as already discussed in section 5.3.3.1. Hence

$$n\left(\mu + dt; z - \frac{wd}{2\pi R}N(z,t)\,dt, t + dt\right) = n(\mu;z,t). \tag{5.56}$$

Expanding the left hand side then yields

$$\frac{\partial n(\mu;z,t)}{\partial \mu} - \frac{wd}{2\pi R} N(z,t) \frac{\partial n(\mu;z,t)}{\partial z} + \frac{\partial n(\mu;z,t)}{\partial t} = 0 \tag{5.57}$$

and integrating over μ leads us to Eq. (5.5):

$$-\frac{wd}{2\pi R} N(z,t) \frac{\partial N(z,t)}{\partial z} + \frac{\partial N(z,t)}{\partial t} = 0 \tag{5.58}$$

were we have used the fact that $n(0;z,t) = 0$ as no new synthases are produced (the birth rate is zero) and $n(\infty;z,t) = 0$ for finite t.

We now turn to the problem of determining the spatio-temporal evolution equation for $n(\mu;t,z)$. Consider for the moment non-moving synthases ($w = 0$), and new synthase production occurring at a fixed location z_0 by a function $f(N(t,z_0))$. For $\mu > 0$ we have

$$n(\mu + dt; t + dt, z_0) = n(\mu;t,z_0) \tag{5.59}$$

so that

$$\frac{\partial n(\mu;t,z_0)}{\partial \mu} + \frac{\partial n(\mu;t,z_0)}{\partial t} = 0 \tag{5.60}$$

which is solved by an arbitrary function $n(\mu;t,z_0) = \bar{n}(t-\mu,z_0)$. Now consider what happens for $\mu = 0$: the number of rosettes of age $\mu = 0$ in z_0 is equal, by definition, to the number of rosettes created in z_0 by the local rate of production $f(N(t))$. This implies that:

$$n(0;t,z_0) = f(N(t,z_0)) = \bar{n}(t,z_0) \tag{5.61}$$

and hence

$$n(\mu;t,z_0) = f(N(t-\mu,z_0)) \tag{5.62}$$

We now generalize to the case in which new synthase production takes place not only at a fixed location z_0, but within an *insertion domain* (ID), that in itself moves with a velocity v. The local rate of production is then described by a function

$$n(0;z,t) = F(z,t,N(z,t)) = g(z-vt) f(N(z,t)) \tag{5.63}$$

where, as said in the previous section, $g(z)$ depends upon the specific choice of the ID shape.

Finally, we turn to the "de-activation" processes. With the definition of the new variable $n(\mu;t,z)$, it is now possible to allow for death rates that depend on the age μ of the rosettes. We assume, therefore, that synthases are deactivated at a generic rate $r(\mu)$. The full equation becomes

$$\frac{\partial n(\mu;z,t)}{\partial \mu} - \frac{wd}{2\pi R} N(z,t) \frac{\partial n(\mu;z,t)}{\partial z} + \frac{\partial n(\mu;z,t)}{\partial t} = -r(\mu) n(\mu;z,t) \tag{5.64}$$

$$n(0;z,t) = F(z,t,N(z,t)). \tag{5.65}$$

Looking at this equation it is possible to note that, differently from what we have seen in the previous section, the birth rate function $n(0;z,t)$ doesn't appear anymore in the right hand side of the evolution equation. Rather, it plays the role of a boundary condition that has to be specified to consistently solve the equation. We will return to this point in the next section.

5.4.2.2 Example: the Poissonian Decay

To better elucidate the meaning of the new evolution equation, we start focusing our attention on a quite simple example. Let $r(\mu)$ be a Poissonian decay rate, i.e. $r(\mu) = -\mu_\dagger^{-1}$. Here $\mu_\dagger$ is a constant that represents the average time after which the number of rosettes significantly decreases, independently from the specific age of the particles. We are going to couple this decay process with the standard "square wave" ID and constant production rate (Eq. 5.9), so that the full equation becomes

$$\frac{\partial n(\mu;z,t)}{\partial \mu} - \frac{wd}{2\pi R} N(z,t) \frac{\partial n(\mu;z,t)}{\partial z} + \frac{\partial n(\mu;z,t)}{\partial t} = -\frac{1}{\mu_\dagger} n(\mu;z,t) \tag{5.66}$$

$$n(0;z,t) = \frac{N^*}{t^*} \theta(vt - z)\, \theta(l - (vt - z))\, \theta(N_* - N(z,t)) \tag{5.67}$$

where t^* is the time necessary to build up to the maximum density. As the death rate does not depend on age we can integrate over μ to obtain

$$\frac{\partial N(z,t)}{\partial t} - \frac{wd}{2\pi R} N(z,t) \frac{\partial N(z,t)}{\partial z} = f_* \theta(vt - z)\, \theta(l - (vt - z))\, \theta(N_* - N(z,t)) - \frac{1}{\mu_\dagger} N(z,t) \tag{5.68}$$

so that we are back to the evolution equation for our original variable $N(t,z)$: as one can see, this equation is just a specific case of Eq. (5.6) with a non-constant life time of the rosettes. If we non-dimensionalize by setting

$$\tau = \frac{t}{t_*} \qquad \zeta = \frac{z}{wt_*} \qquad \nu = \frac{N}{N_*}$$

we then obtain the final equation

$$\frac{\partial \nu(\zeta,\tau)}{\partial \tau} - \nu(\zeta,\tau) \frac{\partial \nu(\zeta,\tau)}{\partial \zeta} = \theta(\beta\tau - \zeta)\, \theta(\lambda - (\beta\tau - \zeta))\, \theta(1 - \nu(\zeta,\tau)) - \frac{1}{\varphi_\dagger} \nu(\zeta,\tau) \tag{5.69}$$

where

$$\beta = \frac{v}{w} \qquad \lambda = \frac{l}{wt_*} \qquad \varphi_\dagger = \frac{\mu_\dagger}{t_*}.$$

We now follow the procedures described in Appendix to obtain the solution along a characteristic specified by the initial data

$$\zeta(0;p) = p \tag{5.70}$$

$$\nu(0;p) = 0. \tag{5.71}$$

Along the characteristics we have the coupled equations

$$\frac{d\zeta(\tau;p)}{d\tau} = -\nu(\tau;p) \tag{5.72}$$

$$\frac{d\nu(\tau;p)}{d\tau} = \theta(\beta\tau - \zeta(\tau;p))\, \theta(\lambda - (\beta\tau - \zeta(\tau;p)))\, \theta(1 - \nu(\tau;p)) - \frac{1}{\varphi_\dagger} \nu(\tau;p). \tag{5.73}$$

Without loss of generality we can choose $p = 0$ and drop the label. Since the Poissonian decay rate affects on an equal footing old and young rosettes, creation and deactivation are no more decoupled processes, and can coexist at the same time. Therefore, the equation for the density is

$$\frac{d\nu(\tau)}{d\tau} = 1 - \frac{1}{\varphi_\dagger}\nu(\tau) \tag{5.74}$$

with solution

$$\nu(\tau) = \varphi_\dagger\left(1 - e^{-\frac{\tau}{\varphi_\dagger}}\right). \tag{5.75}$$

In order to consider helicoidal-like solution we require that the maximum density is reached in a finite time. This determines the parameter φ_* by imposing $\nu(\varphi_*) = 1$, condition that brings us

$$\varphi_* = \varphi_\dagger \ln\frac{\varphi_\dagger}{\varphi_{\dagger-1}} \qquad \varphi_\dagger > 1. \tag{5.76}$$

We can also readily integrate the position equation yielding

$$\zeta(\tau) = \varphi_\dagger\left(\varphi_\dagger\left(1 - e^{-\frac{\tau}{\varphi_\dagger}}\right) - \tau\right). \tag{5.77}$$

The helicoidal solution also requires that the characteristic crosses the bottom of the ID exactly at the point where the maximum density is reached. This implies that $\zeta(\varphi_*) = \beta\varphi_* - \lambda$ so that

$$\lambda = \varphi_\dagger\left((\beta - \varphi_\dagger)\ln\frac{\varphi_\dagger}{\varphi_\dagger - 1} - 1\right) \tag{5.78}$$

After the passage of the ID only deactivation can occur. The post maximum solution is then obtained from

$$\frac{d\nu(\tau)}{d\tau} = -\frac{1}{\varphi_\dagger}\nu(\tau),\ \nu(\varphi_*) = 1 \tag{5.79}$$

with solution

$$\nu(\tau) = e^{-\frac{\tau-\varphi_*}{\varphi_\dagger}} \tag{5.80}$$

so that

$$\zeta(\tau) = \zeta(\varphi_*) - \varphi_\dagger\left(1 - e^{-\frac{\tau-\varphi_*}{\varphi_\dagger}}\right). \tag{5.81}$$

Fig. 5.13 shows the behaviour of $\zeta(\tau)$ and $\nu(\tau)$ for the Poissonian decay problem. Note that in this case, even if the helicoidal solution can be still achieved, the density goes to zero exponentially without vanishing in a finite time.

5.4.2.3 General solution

We now go back to Eq. (5.64) and search for a general solution that is independent from the particular form of the death rate. First we restate the full equation in dimensionless form:

$$\frac{\partial n(\varphi;\zeta,\tau)}{\partial\varphi} - \nu(\zeta,\tau)\frac{\partial n(\varphi;\zeta,\tau)}{\partial\zeta} + \frac{\partial n(\varphi;\zeta,\tau)}{\partial\tau} = -r(\varphi)\,n(\varphi;\zeta,\tau) \tag{5.82}$$

$$n(0;\zeta,\tau) = F(\zeta,\tau,\nu(\zeta,\tau)). \tag{5.83}$$

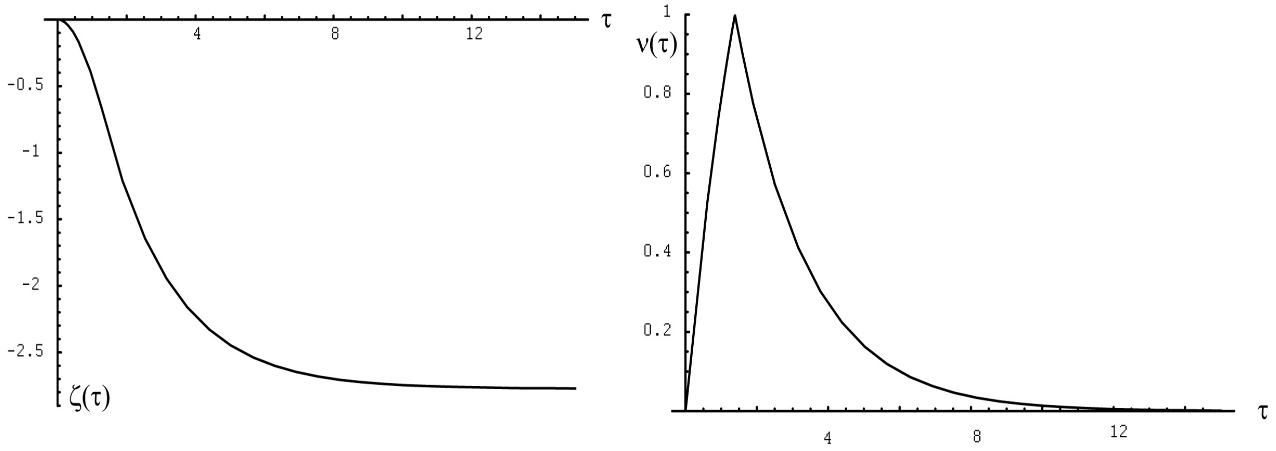

Figure 5.13: $\nu(t)$and $\zeta(t)$ for the Poissonian case

We then consider characteristics for this equation labelled by a space-time point $\left(\bar{\zeta},\bar{\tau}\right)$. Along this characteristic the evolution of the age distribution is given by

$$\frac{dn\left(\varphi;\bar{\zeta},\bar{\tau}\right)}{d\varphi} = -r\left(\varphi\right)n\left(\varphi;\bar{\zeta},\bar{t}\right) \tag{5.84}$$

$$n\left(0;\bar{\zeta},\bar{\tau}\right) = F\left(\bar{\zeta},\bar{\tau},\nu\left(\bar{\zeta},\bar{\tau}\right)\right) \tag{5.85}$$

with formal solution

$$n\left(\varphi;\bar{\zeta},\bar{\tau}\right) = F\left(\bar{\zeta},\bar{\tau},\nu\left(\bar{\zeta},\bar{\tau}\right)\right)e^{-\int_0^{\varphi}d\varphi' r(\varphi')}. \tag{5.86}$$

Note that

$$\frac{d\tau\left(\varphi;\bar{\zeta},\bar{\tau}\right)}{d\varphi} = 1 \tag{5.87}$$

that implies

$$\tau\left(\varphi;\bar{\zeta},\bar{\tau}\right) = \varphi + \bar{\tau}. \tag{5.88}$$

To get at the full dynamics of the problem, we need to consider the evolution of the total number of synthases along the characteristics. We do this by integrating Eq. (5.64) over φ to obtain

$$\frac{\partial\nu\left(\zeta,\tau\right)}{\partial\tau} - \nu\left(\zeta,\tau\right)\frac{\partial\nu\left(\zeta,\tau\right)}{\partial\zeta} = F\left(\zeta,\tau,\nu\left(\zeta,\tau\right)\right) - \int_0^{\infty} d\varphi r\left(\varphi\right)n\left(\varphi;\zeta,\tau\right). \tag{5.89}$$

From either Eq. (5.64) or Eq. (5.89) we find

$$\frac{d\zeta\left(\tau;\bar{\zeta},\bar{\tau}\right)}{d\tau} = -\nu\left(\tau;\bar{\zeta},\bar{t}\right) \tag{5.90}$$

so that along the characteristic we have

$$\begin{aligned}\frac{d\nu\left(\tau;\bar{\zeta},\bar{\tau}\right)}{d\tau} &= F\left(\zeta\left(\tau;\bar{\zeta},\bar{\tau}\right),\tau,\nu\left(\zeta\left(\tau;\bar{\zeta},\bar{\tau}\right),\tau\right)\right)-\int_0^\infty d\varphi r\left(\varphi\right)n\left(\varphi;\zeta\left(\tau-\varphi;\bar{\zeta},\bar{\tau}\right),\tau-\varphi\right)\\ &= F\left(\zeta\left(\tau;\bar{\zeta},\bar{\tau}\right),\tau,\nu\left(\zeta\left(\tau;\bar{\zeta},\bar{\tau}\right),\tau\right)\right)\\ &\quad -\int_0^\infty d\varphi r\left(\varphi\right)F\left(\zeta\left(\tau-\varphi;\bar{\zeta},\bar{\tau}\right),\tau-\varphi,\nu\left(\tau-\varphi;\bar{\zeta},\bar{\tau}\right)\right)e^{-\int_0^\varphi d\varphi' r(\varphi')} \qquad (5.91)\end{aligned}$$

which is a functional delay equation.

If

$$r\left(\varphi\right)=\begin{cases}0 & 0\leq\varphi<\varphi_\dagger\\ \infty & \varphi\geq\varphi_\dagger\end{cases} \qquad (5.92)$$

then

$$\frac{d\nu\left(\tau;\bar{\zeta},\bar{\tau}\right)}{d\tau}=F\left(\zeta\left(\tau;\bar{\zeta},\bar{\tau}\right),\tau,\nu\left(\zeta\left(\tau;\bar{\zeta},\bar{\tau}\right),\tau\right)\right)-F\left(\zeta\left(\tau-\varphi_\dagger;\bar{\zeta},\bar{\tau}\right),\tau-\varphi_\dagger,\nu\left(\tau-\varphi;\bar{\zeta},\bar{\tau}\right)\right) \qquad (5.93)$$

which is the original case considered in the geomodel.

The second term on the right hand side of Eq. (5.91) can also be partially integrated to yield

$$\frac{d\nu\left(\tau;\bar{\zeta},\bar{\tau}\right)}{d\tau}=-\int_0^\infty d\varphi e^{-\int_0^\varphi d\varphi' r(\varphi')}\frac{d}{d\varphi}F\left(\zeta\left(\tau-\varphi;\bar{\zeta},\bar{\tau}\right),\tau-\varphi,\nu\left(\tau-\varphi;\bar{\zeta},\bar{\tau}\right)\right). \qquad (5.94)$$

The latter form is especially convenient when F is of the "square wave" constant production rate type. In this case the derivative $\frac{dF}{d\varphi}$ then is identically zero except at the switching points, where it becomes a δ-function. Let us denote

$$R\left(\varphi\right)=\int_0^\varphi d\varphi' r\left(\varphi'\right). \qquad (5.95)$$

and consider the characteristic starting from $\bar{\zeta}=\bar{\tau}=0$. In the pre-maximum density phase, the solution must then obey

$$\frac{d\nu_<\left(\tau\right)}{d\tau}=\int_0^\infty d\varphi e^{-R(\varphi)}\delta\left(\tau-\varphi\right)=e^{-R(\tau)} \qquad (5.96)$$

$$\nu_<\left(0\right)=0 \qquad (5.97)$$

with solution

$$\nu_<\left(\tau\right)=\int_0^\tau d\varphi e^{-R(\varphi)}. \qquad (5.98)$$

Let τ_1 be the time at which the maximum density is reached, so that

$$\nu_<\left(\tau_1\right)=\int_0^{\tau_1} d\varphi e^{-R(\varphi)}=1. \qquad (5.99)$$

Assume also that at τ_1 the helicoidal condition is met, so that production is fully cut off. Then the post maximum equation is

$$\frac{d\nu_>(\tau)}{d\tau} = -\int_0^\infty d\varphi e^{-R(\varphi)} \{-\delta(\tau-\varphi)+\delta(\tau-\varphi-\tau_1)\} = e^{-R(\tau)} - e^{-R(\tau-\tau_1)} \tag{5.100}$$

$$\nu_>(\tau_1) = 1 \tag{5.101}$$

with solution

$$\nu_>(\tau) = 1 + \int_{\tau_1}^{\tau} d\varphi \left\{ e^{-R(\varphi)} - e^{-R(\varphi-\tau_1)} \right\}$$

. Inserting $R(\varphi) = \frac{\varphi}{\varphi_\dagger}$ and $\tau_1 = \varphi_\dagger \ln \frac{\varphi_\dagger}{\varphi_{\dagger-1}}$ and some algebra retrieves the previously discussed Poissonian case. Another special case is $R(\varphi) = 0$ for $\varphi \leq 1$ and $R(\varphi) = \infty$ for $\varphi > 1$ (the helicoidal $\gamma = 0$ case of the original model). Here we recover

$$\nu_<(\tau) = \tau \tag{5.102}$$

and

$$\nu_>(\tau) = 2 - \tau \tag{5.103}$$

which essentially are the results Eqs. (5.23) and (5.27) presented before.

5.4.3 Effect of fluctuations

Another way to test the robustness of the Geomodel, is to verify the validity of its solutions in presence of fluctuations of the birth rate of rosettes. From now on, we will then assume that the local production rate of particles is described by a function

$$G(t,z) = h(t,z) + \eta(t,z) \tag{5.104}$$

where $h(t,z)$ is a deterministic production rate, like for example the ones discussed in Eq. (5.7) or Eq. (5.30), and $\eta(t,z)$ represents the effect of fluctuations that can locally increase or decrease the number of created rosettes.

5.4.3.1 Solving the problem of overcrowding

To fully take into account the effect of this randomness on the trajectories of the rosettes, and therefore on the orientation of the deposited CMFs, we need to slightly modify one of the main elements of the original Geomodel: we have to allow for the maximum local number N_* of particles to be surpassed. The main consequence of the presence of a noise term in the birth rate, in fact, is to provoke in some cases an overcrowding of the rosettes, whose number can then increase beyond the maximum value N_*. The original geomodel would be inconsistent with respect to such a perturbation: from Eq. (5.4) it is clear, in fact, that, if $N(t,z) > N_*$, the axial speed $\dot{z}(t)$ of a particle would be greater than its present absolute velocity w.

To solve this inconsistency, we therefore need to assume that the velocity w of a particle is no longer constant, but rather depends linearly on the number of active rosettes $N(t,z)$ (Fig. 5.14a) according to the rule:

$$w[N(t,z)] = w_0\,[2 - \frac{d}{2\pi R}N(t,z)] = w_0\,[2 - \frac{N(t,z)}{N_*}]$$

where w_0 represents the new velocity parameter. Consequently, following Eq. (5.4), the vertical velocity of the rosette $\dot{z}(t)$ has the expression:

$$\dot{z}(t) = -w[N(t)]\sin\alpha(t) = -w_0\,\frac{N(t)}{N_*}\,[2 - \frac{N(t)}{N_*}].$$

If we non-dimensionalize in the usual way by setting

$$\nu = \frac{N}{N_*} \qquad \zeta = \frac{z}{w_0 t_*} \qquad \lambda = \frac{l}{w_0 t_*} \qquad \beta = \frac{v}{w_0} \qquad \tau = \frac{t}{t_*}$$

where t_* is the time necessary to build up to the maximum density, we then obtain that

$$\dot{\zeta}(\tau) = -\nu(\tau)(2 - \nu(\tau)). \tag{5.105}$$

From this equation it follows that the absolute value of the axial speed $\dot{\zeta}(\tau)$ of a rosette, reaches its maximum when $\nu = 1$, and it is equal to 0 for $\nu = 0$, exactly as in the case in in the original geomodel (Fig. 5.14b). However, in this case, the axial velocity is also defined for values of $\nu > 1$, and decreases again to 0 for $\nu = 2$. The introduction of this new density-dependent velocity $w[\nu(\tau)]$ makes the model stable with respect to overcrowding of particles, provided that the fluctuations beyond the value $\nu = 1$ are relatively small.

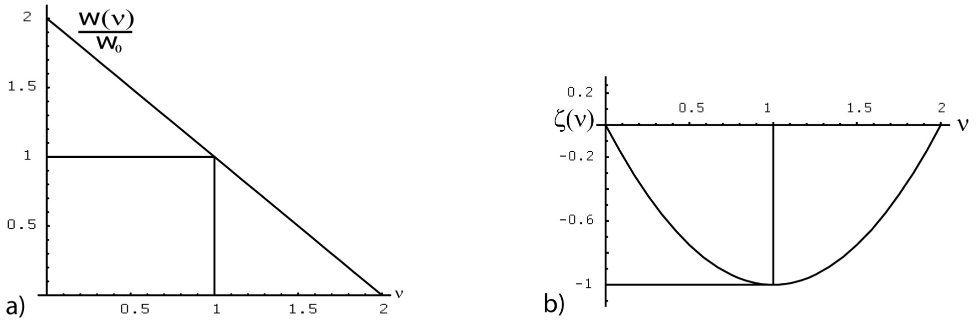

Figure 5.14: $w(\nu)$ and $\dot{\zeta}(\nu)$

From a biological point of view, the fact that the speed of the particles decrease as soon as $\nu > 1$ can be interpreted as follows: when the system is already close packed, the room available for the deposition of a further CMF is very limited, and the overcrowding can cause the rosettes to slow down their motion until they find a suitable disposition to share the available space.

5.4.3.2 Deterministic case

First, to verify that the introduction of the new velocity $w[\nu(\tau)]$ doesn't affect the occurrence of the helicoidal solution, we need to repeat the same mathematical procedure discussed in the Geomodel, in order to determine the new trajectories of the rosettes along the cylinder. To do this we start considering the deterministic case, i.e. we neglect for the moment the presence of the noise term $\eta(t,z)$ in Eq. (5.104) and look for the conditions that have to be satisfied for the helicoidal pattern to be achieved. We choose as our birth rate function the one examined in Eq. (5.7). Solving the equation of motion with the usual method of characteristics, after some trivial calculations we find that the relations that have to be satisfied among the various parameters of the system to obtain the helicoidal solution are:

$$\tau_* = \tau^\dagger \qquad\qquad \lambda = \beta + 2/3 \tag{5.106}$$

where, as usual, $\tau^\dagger$ represents the rescaled life time of a rosette. Here we note that, while the first relation corresponds exactly to the one found both in the Geomodel (88) and in the triangular ID case (Eq. (5.42)), the second one is slightly different from the one obtained in case of a constant w (Eq. (5.41)).

Plots of the behaviour of $\zeta(\tau)$ and $\nu(\tau)$ obtained solving the evolution equation are shown in Fig. 5.15. We can see from the pictures that the helicoidal solution can be achieved also in the density-dependent velocity case: $\zeta(\tau)$ is continuously decreasing, while the density $\nu(\tau)$, starting from 0, reaches its maximum value $\nu = 1$ and then decreases again.

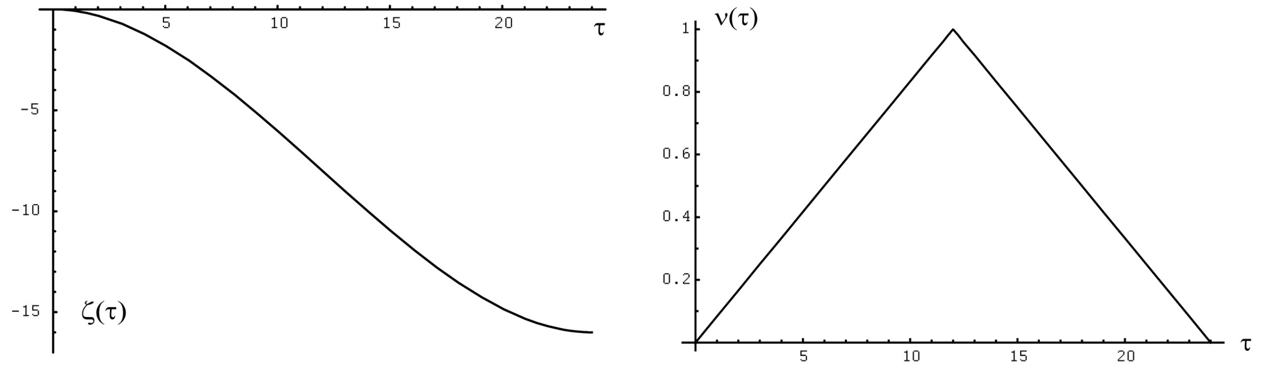

Figure 5.15: Theoretical behaviour for $\zeta(\tau)$ and $\nu(\tau)$ in the velocity-dependent case

5.4.3.3 Simulating the fluctuations

We now want to test this new geometrical rule in presence of fluctuations of the birth rate. To do so, we build a simple many-body simulation that reproduces the spatio-temporal dynamics of the co-moving rosettes. The simulation is two-dimensional and it is limited to the surface of a cylinder, so that the position of a particle is identified by its coordinate $z(t)$ along the axis of the cylinder and its azimuthal angle $\psi(t)$. The rosettes are represented as point particles with an effective range of interaction d. However, we have to keep in mind that this interaction range is defined only on the z direction, i.e. particles at the same quote z_R are always interacting independently from their azimuthal angle $\psi(t)$ and from the radius R of the cylinder. The rosettes have a fixed life-time $t^\dagger$, and once they are created they start moving downward along the cylinder with an axial speed that depends on the local number of neighbouring particles present in that moment within their range of interaction. When the rosettes reach their maximum life time, they die and are automatically removed from the system. The ID is a region of length l that moves in the "plus" direction (positive direction of z-axis) with a velocity v. Once l, v, and $t^\dagger$ are fixed, the parameter w_0 is chosen in such a way to satisfy the second relation shown in Eq. 5.106. The ID is discretized in m small sections of size Δz, so that $l = m\Delta z$. For sake of simplicity we set also $\Delta z = d$, in such a way that all the particles present in a single slice Δz become automatically interacting particles.

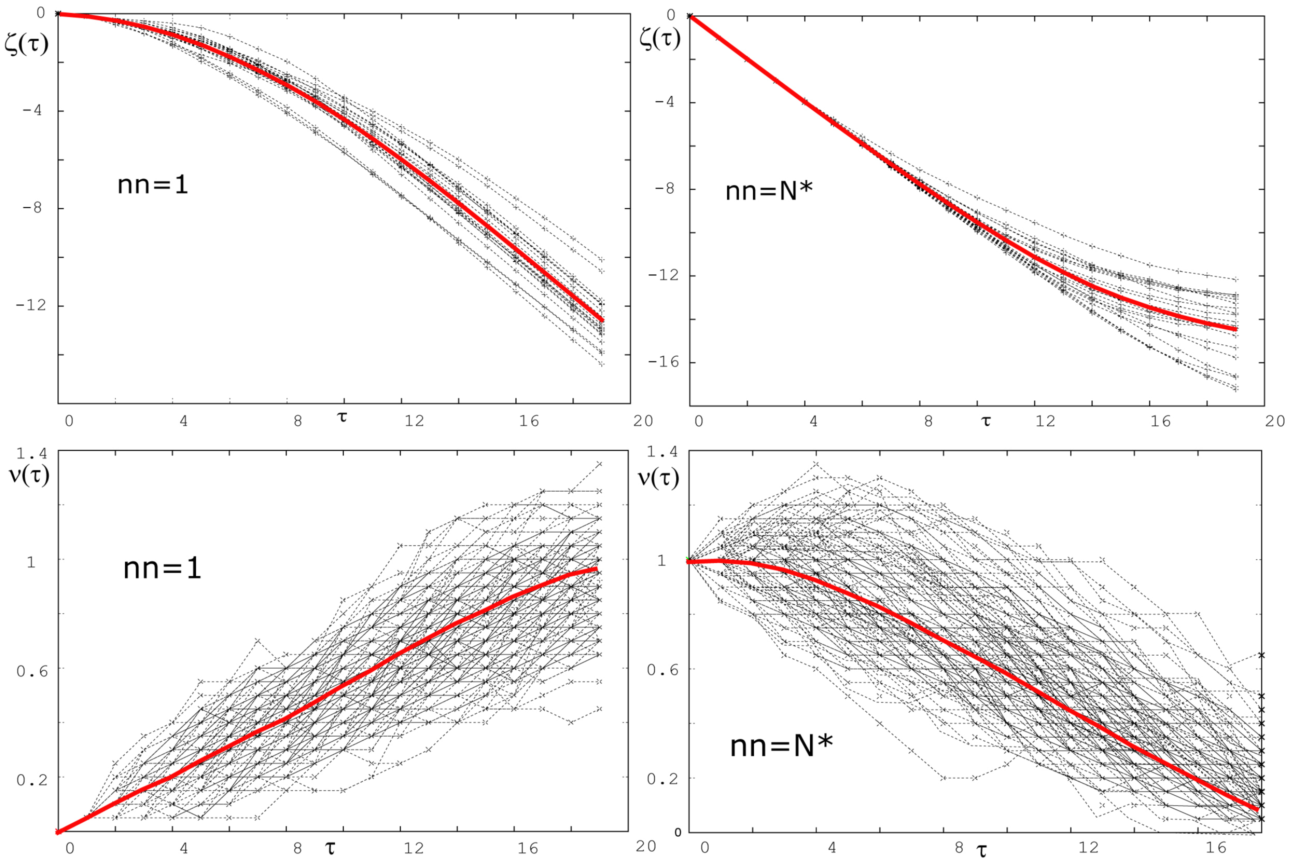

Figure 5.16: $\zeta(\tau)$ and $\nu(\tau)$ in the fluctuating case: the characteristic (red line) in each picture is the average of the 20 different curves (black lines) in the same plot

At each time step of the simulation two different events happen one after the other:

1. First creation of new rosettes occurs: a number G of new particles in inserted in each of the m sections of the domain (provided that the maximum number N_* is not reached within that section). Note that, in this case, the number G is no more a constant, but

can vary between $G_m = h - \eta$ and $G_M = h + \eta$ randomly, where h is a fixed number of particles and η is an integer that represents the amplitude of the noise. During this "birth phase" the motion of all the particles is frozen

2. After the birth's event, the number of local neighbours of each of the particles is counted, and all the rosettes (still alive) are moved with an axial speed that satisfies the Eq. (5.105). To compute the number of neighbouring rosettes, only the particles that are within a range Δz are counted.

5.4.3.4 Plotting the results

Since the simulation explicitly implements the dynamics of the particles, the information provided by its output is limited to the real trajectories of the rosettes along the cylinder. Thus, in order to compare the data provided by the the simulation with the theoretical behaviour found in the previous section, we need to translate these trajectories into a more appropriate quantity. As already said, any arc of length $\tau^{\dagger}$ along the characteristic defined in Eq. (5.16) can be identified with the trajectory of a rosette. Thus, it should be possible to construct the characteristic plotting one after the other the temporal evolution of the z-coordinate of the rosettes along the cylinder.

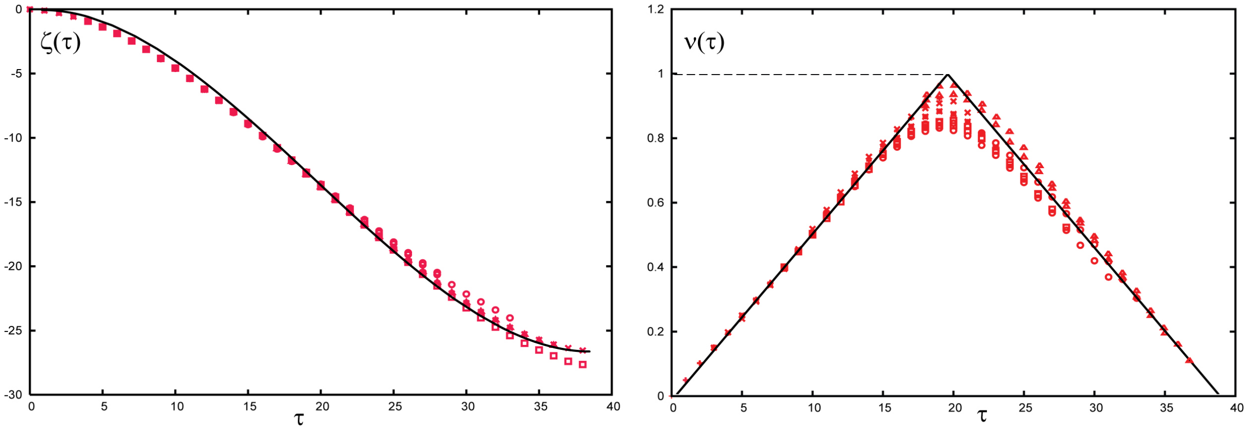

Figure 5.17: Comparison between $\zeta(\tau)$ and $\nu(\tau)$ in the fluctuating and deterministic case: the red dots represent the simulation, the solid line is the deterministic theoretical curve.

To do so, we need to divide the trajectories of all the rosettes in categories, each of them being identified by the different number of neighbouring particles at the moment of the birth of the rosette itself. As an example, Fig. 5.16 shows a typical output of the simulation: here, in Fig. 5.16a you can see the rescaled trajectories of $N = 20$ particles which, at the moment of their birth, had no other particles in their interaction range. As you can see, the coordinate $\zeta(\tau)$ starts slowly decreasing (the rosettes were alone at the beginning, so that $\nu(0) \simeq 0$) and bends more and more as time goes by. Averaging over these 20 trajectories brings us to the red line shown in the same figure: for what has been said before, this average corresponds to the first part of the theoretical characteristic. Let's now consider the case of rosettes that were born with a number N_* of neighbouring particles in their interaction range. In this case, as you can see from Fig. 5.16b ,the trajectories start very bent (the maximum number N_* in fact corresponds to a value $\nu(0) = 1$) and slowly decrease in time.

The same procedure can be applied for $\nu(\tau)$: in this case, to plot the temporal behaviour of this quantity, it is sufficient to count the number of particles that a rosette encounters along this trajectory. As an example, Fig. 5.16c-d show the temporal evolution of the number of particles encountered by $N = 20$ different rosettes, in case in which they had 0 (Fig. 5.16c) or N_* (Fig. 5.16d) neighbouring particles in their interaction range at the moment of their birth.

Plotting these averages (conveniently rescaled) for all the categories one after the other, it is then possible to construct the theoretical characteristics, both for $\nu(\tau)$ and for $\zeta(\tau)$. Fig. 5.17 shows the comparison between the theoretical results and the output of the simulation: as you can see there is a good agreement between the data: the presence of fluctuations doesn't prevent the helicoidal pattern of CMFs from occurring.

5.5 Conclusions

In this chapter we have illustrated and improved the model for cell wall deposition, proposed by Mulder *et al.* (88), aimed at understanding the regularity of the cellulose pattern in the wall of plant cells. This dynamical geometrical model is based on a phenomenological equation of motion of the rosettes on the cell surface, and takes into account the global geometrical and packing constraints imposed on the deposited CMFs. In this chapter we were able to validate the robustness of this model against a number of different perturbations and noise effects (different shapes of production waves, generic life-time distribution of rosettes, fluctuations of local birth events), demonstrating that the described mechanism can be considered a strong and successful tool in explaining and predicting the occurring of helicoidal textures in the cell wall of a wide variety of plant species and cell types.

6 Acetobacter: a case study

Acetobacter is a bacterium commonly found in alcoholic beverages, vinegar, cider, fruits, flowers, and even soil. It is an organism of particular importance because it is used in the commercial production of vinegar, having the ability to convert alcohol (ethanol) to acetic acid in the presence of air. More familiarly, cultures of this bacterium (Fig. 6.1a) correspond to the substance known as “vinegar plant” or “mother” (Fig. 6.2b), used for vinegar brewing in the old days in Europe. Cultured in pure conditions, the "vinegar mother" has been identified for the first time by Brown (92; 93) to be mainly composed of cell-wall cellulose from its chemical composition and reactivity. This revelation has made *Acetobacter* one of the most prolific cellulose-producing organisms.

In this Chapter we will investigate the cellulose deposition process of a particular species of *Acetobacter*, *A. Xylinum*. We will show how the peculiar motion this bacterium exhibits during the polymerization process can be correlated to an hydrodynamic effect between the cellulose chains and the fluid in which they are immersed. Moreover, in the final part of the Chapter, we implement a Brownian Dynamic Simulation that reproduces the main features of this bacterial motion.

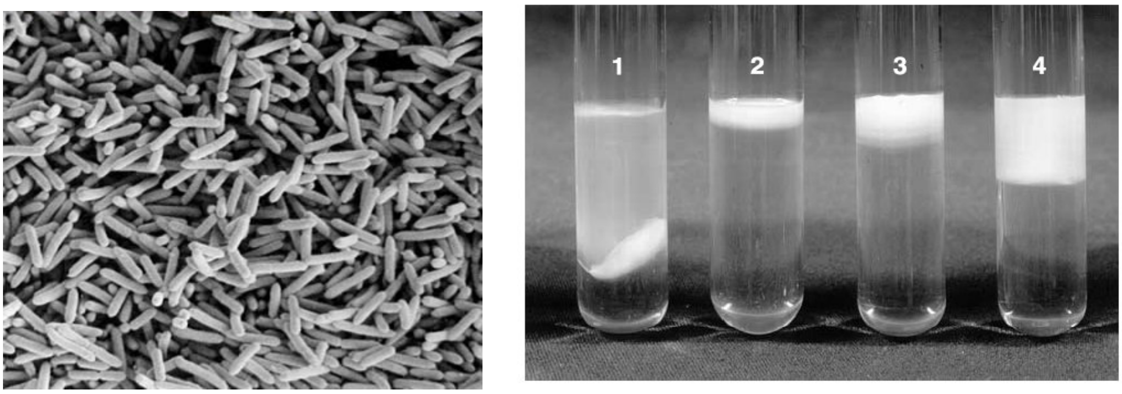

Figure 6.1: a) Bacterial cultures and b) Cellulose pellicle forming at the air-liquid interface of the culture medium

6.1 Making cellulose from vinegar?

The cellulose mat associated with the production of vinegar, as well as of the fermented tea “Kombucha Tea” (94), and of the food product “Nata de Coco” (95), has been observed and used for centuries, before being isolated and formerly recognized as secondary metabolite of the bacterium *Acetobacter*. Described by Louis Pasteur as *"a sort of moist skin, swollen, gelatinous and slippery"* substance, this cellulose product has started drawing a scientific interest only when microscopic observations disclosed bacteria distributed throughout the matrix.

Although the solid portion in the gel-like substance is less than one percent by weight, it is almost pure cellulose free of lignin, pectin and hemicellulose as well as other biogenic products, which are associated with plant-derived cellulose. This pure cellulose mat can be cleaned and dried, and the product used for many applications. One of the unique features of the bacterial cellulose membrane is that it is very strong in the dried state, and it can hold hundreds of times its own weight in water. This great absorptivity and mechanical strength, together with the high crystallinity, constitute three of the main features of microbial cellulose.

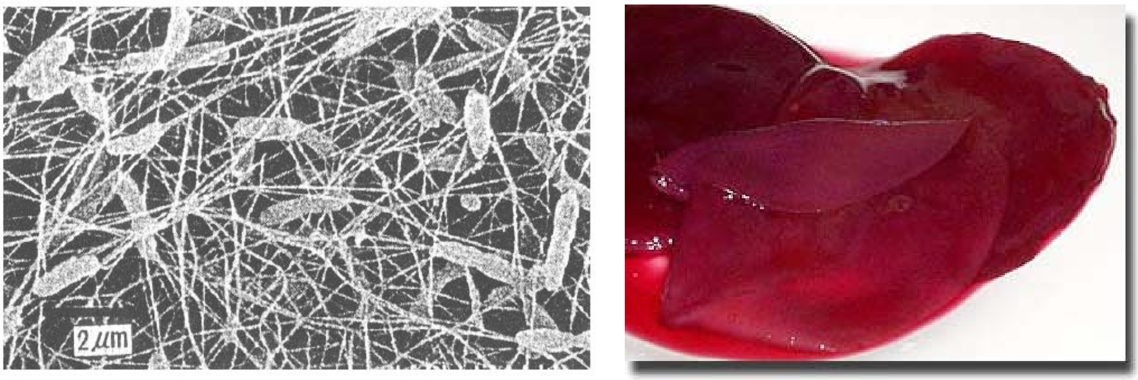

Figure 6.2: a) Matrix of interwoven ribbons and b) Vinegar mother

The reason why *Acetobacter* generate cellulose has long been a puzzle for biologists. One hypothesis is that these aerobic bacteria produce a pellicle to maintain their position close to the oxygen-rich surface of the culture solution (96; 97). Another theory assumes that the bacteria generate cellulose to guard themselves from ultraviolet radiation (98). Another opinion is that they use it to construct a "cage" in which they confine themselves to protect themselves from enemies, whereas nutrients can be still supplied by diffusion (99).

6.2 Acetobacter Xylinum

Acetobacter Xylinum is a particular species of *Acetobacter*. This rod-shaped, motile, non-photosynthetic organism, can be simply grown in a shallow tray with a culture medium such as coconut juice, sugarcane juice, vinegar, and fermented beverage (100; 101). Starting from these materials, it can procure glucose, sugar and other organic substrates and convert them into pure cellulose. *A. Xylinum* is nature's most prolific cellulose-producing bacterium: a typical single cell can convert up to 108 glucose molecules per hour into cellulose. Since about a million cells can be packed into a large liquid droplet, the amount of cellulose produced by a culture of these bacteria during few hours can be substantial.

Under the classic cultivation conditions, *A. Xylinum* produces cellulose in form of a flat ribbon that is deposited parallel to the longitudinal axis of the bacterium (Fig. 6.3 and Fig. 6.4). The matrix of the bacterial interwoven ribbons (Fig. 6.2a) constitutes the gelatinous cellulose pellicle previously discussed. The cellulose network forms as a sheet floating on the the air-liquid interface of the culture medium (Fig. 6.1b). As the pellicle grows, it is pushed down the medium, since new cellulose crystallizes predominantly on the top surface of the pellicle. For this reason, while the kinetics is initially limited by oxygen, as the pellicle thickens the kinetics become limited by substrate diffusion through the pellicle.

Trying to elucidate the biosynthetic pathway of cellulose in plants has motivated most early microbial cellulose research. As an extra-cellular, over producer of this polysaccharide, *A. Xylinum* has been a useful tool in clarifying the mechanism of cellulose production. Cellulose biogenesis in *A. Xylinum* occurs between the outer lipopolysaccharide membrane and the inner cytoplasm membrane. Freeze fracture EM images show that the cellulose-synthesizing complexes are linearly arranged along the longitudinal axis of the bacterial rods, over most of the length of the bacteria (Fig.6.3). We will refer to this array as a linear Cellulose Synthase Complex (linear CSC), and each particle that composes it will be named a CSC subunit (Fig. 3.3a, Chap. 3). The particular arrangement of the enzyme complexes in the cell body serves to determine the native hierarchical aggregation of the polymer chains into the final crystalline product, as will be shown in the next section.

The subunits, within the bacterial envelope, have an average diameter of 10-12 nm, and associate with pores of smaller size (3.5 nm) on the surface of the bacterium, to spin out glucan chains from the cell. The number of particles and pores per unit length is almost constant (average 3.8 pores/particles per 100 nm), and their absolute number varies between 12 in dividing cells and 70 in elongating non-dividing cells.

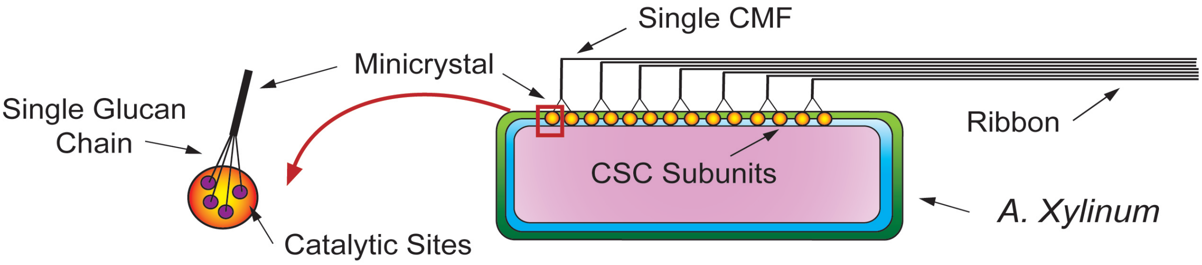

Figure 6.3: Cartoon representing the hierarchical assembly of the ribbon

6.2.1 The Ribbon assembly

The mechanism of formation as well as the structure of the bacterial cellulose product has been studied extensively in recent decades. The top of the hierarchy is represented by a long ribbon of cellulose (>10 μm) which extends parallel to the longitudinal axis of the cell (Fig. 6.4). The ribbon has an average width of 40-60nm (71) , and it is made up of cellulose microfibrils (CMFs) forming bundles that lie side by side organized in layers. The CMFs have a diameter of about 3.5 nm, and are believed to be the result of the aggregation of several mini-crystals, each being the product of a single CSC subunit. The 6-15 glucan chains that form a mini-crystal are polymerized by an equal number of catalytic sites within the CSC subunit.

In an attempt to determine the relationship between polymerization and crystallization of β-(1,4) glucan chains into cellulose CMFs, and subsequently into the ribbon, Calcofluor White ST and Carboxymethylcellulose (CMC) were added to active cultures of *A. Xylinum* (12; 102). The additives affected ribbon formation at different stages, but in all cases they stopped the assembly of the final ribbon product. In the presence of CMC, normal fasciation of microfibril bundles was prevented. Instead of forming the typical flat ribbon, glucan chains aggregated in intertwining, separate bundles of cellulose microfibrils. On the other hand, Calcofluor White ST, an industrial brightener, inhibited the crystallization of individual CMFs , while accelerating the polymerization process up to 4 times the control rate. The conclusion of these experiments was that the cellulose ribbon in *A. Xylinum* is formed by a cell directed, self-assembly process. In addition, these results demonstrate that polymerization and crystallization are coupled, consecutive processes, and that the rate of crystallization determines the rate at which polymerization proceeds.

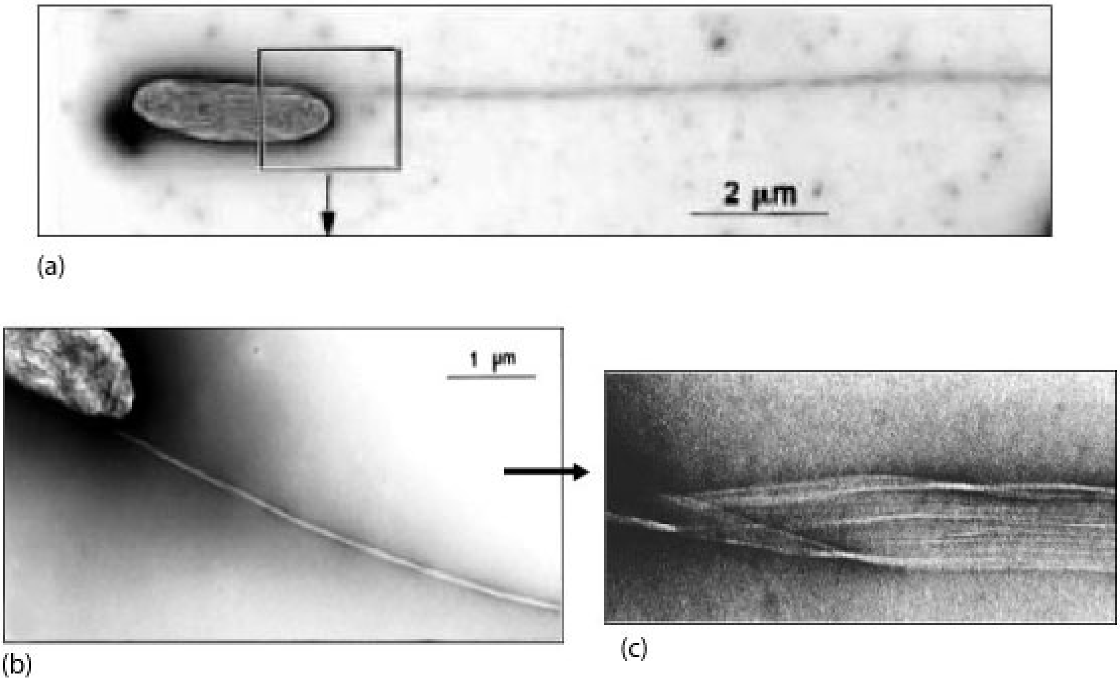

Figure 6.4: (a) and (b): the cellulose ribbon produced by *A. Xylinum*. c) Enlargement showing the twisting of the ribbon

6.2.2 The Band structure

In contrast to the ribbon assembly, under some particular cultivation conditions (103; 104) *A. Xylinum* is able to generate another crystalline structure, the so called “band” (Fig. 6.5a).

Differently from the ribbon, in which the CMF are oriented parallel to each other, the band-like assemblies are composed by crystallites of cellulose II type, which display an anti-parallel arrangement of the fibers. Diffraction studies have shown that the band consists of strand-like cellulose entities, each of which is extruded through a catalytic particle perpendicularly to the long axis of the bacterial cell. A putative folded-chain structure leading to antiparallel chain packing is the one displayed in Fig. 6.5b: a bundle composed of approximately 10-16 parallel glucan chains extruded from a single CSC subunit, self-organizes in a monomolecular sheet, and folds upon itself in an accordeon-like fashion to generate a cellulose strand.

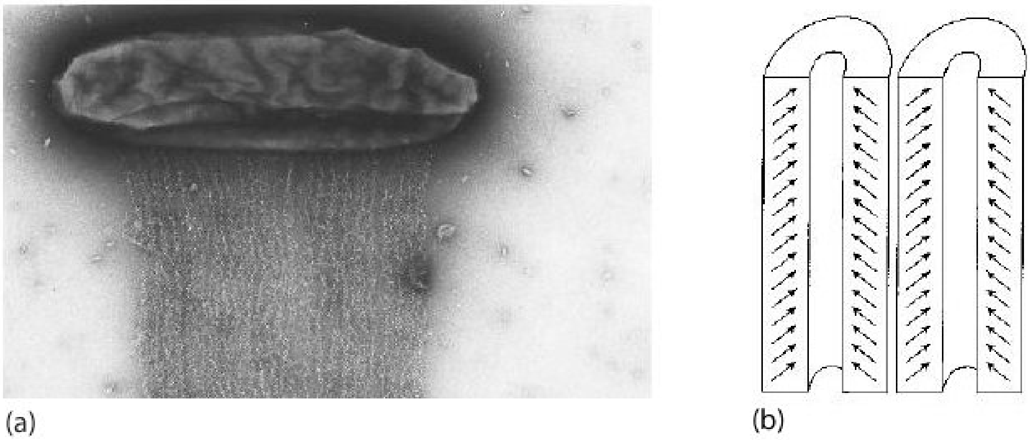

Figure 6.5: (a)The band structure produced by *A. Xylinum.* (b) Putative folding mechanism

The band structure can be obtained with several methods: some mutant strains exclusively produce the band assembly; on the other hand, wild-type strains of *A. Xylinum* can produce the band at high viscosity of the liquid medium, or when the temperature of incubation is dropped at 4°C. Presently the reason that makes the bacterium switch between these two types of cellulose structure is shrouded in mystery.

6.3 Motion of *A. Xylinum*

Brown and coworkers first described the movement of Acetobacter in relation to cellulose biosynthesis in 1976 (18). They found that the stationary cell movement rate of 2.0 *mm* per min at 25°C corresponds with the actual synthesis and extrusion of CMF. The motion is due to an inverse force derived from secretion of crystalline CMFs by the bacterium: when the bacterium moves in a certain direction, the flat ribbon generated by the CMFs crystallization is simultaneously oriented in the same direction of motion. This is not the first example of such a process: in Chapter 3 we have shown how a rosette CSC, the cellulose synthase in plants, exploits the energy derived from cellulose polymerization to travel along the plasma membrane of plant cells while producing the CMF.

During its movement, *A. Xylinum* performs a continuous rotation about its longitudinal axis. Electron Micrograph images show that the cellulose ribbon is twisted, with a constant pitch of about 700nm (Fig. 6.4c). This twisting is probably a consequence of the intrinsic chirality of the planar glucan chains, that constitute the building blocks of the cellulose CMFs. Such chains tend spontaneously to "twist", to relieve the strain built around the oxygen bridge that connects the successive glucan units together. The stress generated during the crystallization of the twisted glucan chains is released by the rotation of the bacterium during its movement.

Many questions arise on how actually the glucan chains extruded from the CSC subunits manage to hierarchically assemble so quickly into a cellulose ribbon, despite the big distance that separates their catalytic subunits on the cell surface. One single chain in fact has an average lateral size of 0.5 nm. A mini-crystal, the bundle of glucan strands extruded from a single CSC subunit, has a diameter of few nanometers. The CSC subunits on the longitudinal axis of the bacterial rod are separated by a distance of about 25-30nm. Given these numbers, it is reasonable to believe that the mini-crystals have to undergo some kind of brownian motion, while elongating, before having the possibility to "find" each other, and then coalesce crystallizing into a CMF. The same reasoning can be applied for the aggregation of CMFs to form the ribbon. Again, since the size of a CMF is about 3.5nm, these fibers have to explore the environment for quite a while before being able to meet and crystallize.

Even more interesting, is the issue of how the CMFs manage to collectively orient and bend in the same direction, to form a structure that runs parallel to the cell surface. To better understand this last point, let's suppose for a moment that after some initial transient, the CMFs have elongated enough to encounter each other and crystallize. The most natural way in which fibers expelled perpendicularly to the bacterium axis would aggregate, is the one showed in Fig. 6.6a . Yet, what *A. Xylinum* produces, is something completely different and counter-intuitive (Fig. 6.6b): at some point, in fact, during the aggregation process, the fibers coordinate and bend all together in the same direction, perpendicular to the row of the catalytic sites. This coordination phenomenon, as said previously, must occur before crystallization happens. As a consequence, the bacterium is pushed unidirectionally by the polymerizing fibers and propels parallel to the deposited ribbon.

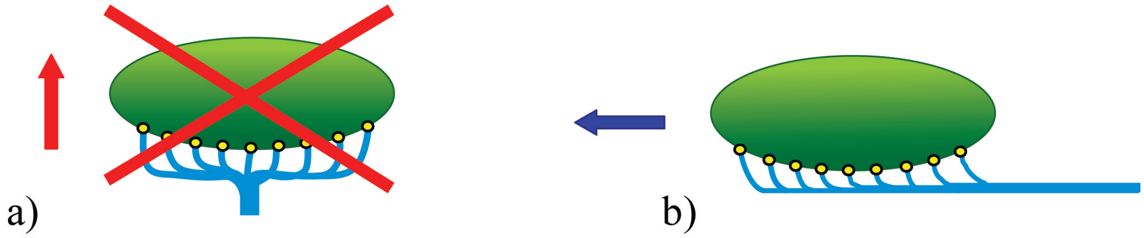

Figure 6.6: The motion mechanism of *A. Xylinum*: instead of moving perpendicularly with respect to his long axis (a), the bacterium prefers to walk parallel to the deposited cellulose ribbon (b)

An analogy to illustrate the uncommon nature of this motion is the following: imagine a raft which floats on the sea surface and which possesses a series of motors attached only to one of its sides. Now imagine to simultaneously turn on all the motors, and guess in which direction the raft will move. Perpendicular to the row of motors, simply. Maybe the raft won't go completely straight, but still it will tend, on average, to have a unidirectional velocity perpendicular to the row of motors.

What happens in *A. Xylinum* is exactly the opposite: once the bacterium starts producing the cellulose chains from the linear CSC, the polymerization force pushes it parallel, and not perpendicular, to the long axis of the cell.

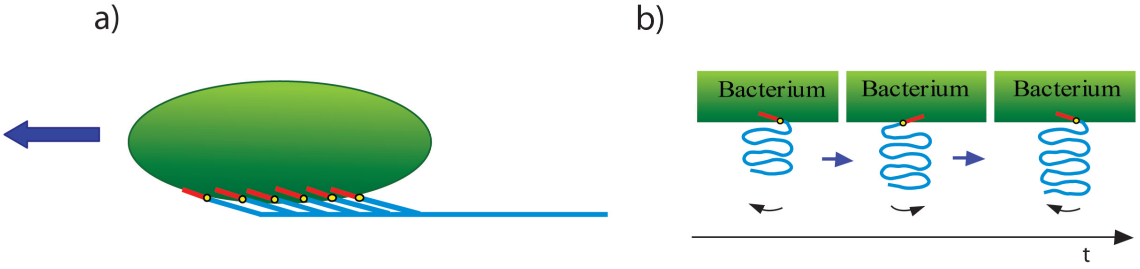

Figure 6.7: a) Possible arrangement of the catalytic sites within the bacterial envelope. b) Folding mechanism that generates the cellulose “bands”

In principle, this kind of motion could be explained if the CSC subunits behaved like internal channels with a fixed, non-perpendicular orientation with respect to the long axis of the bacterium, as showed in Fig. 6.7a. In this way the mini crystals would be extruded from the cell directly in the right orientation to form the ribbon, and the crystallization would proceed more easily. Nevertheless, as mentioned in section 2, it has been shown that *A. Xylinum*, under some particular cultivation conditions (103; 104), can produce another crystalline structure besides the ribbon, the so called “band”. In order to form the folded state that characterizes this structure, the site of extrusion can’t have a fixed orientation, but rather should be able to pivot, to guide and orient the deposition of the cellulose strand and make it fold on itself (Fig. 6.7b).

These data demonstrate that what governs the right assembly of the ribbon is a mechanism that must be independent from the orientation of the catalytic sites. Such mechanism should be capable of breaking the symmetry of the system, coordinating all the filaments extruded from the cell to bend in the right direction and form the final structure. In the following, we will show that this symmetry-breaking effect can be simply caused by “hydrodynamic buckling” of the elongating filaments themselves, a process similar to the Euler Buckling instability, which we will recall in the next section.

6.3.1 Euler Buckling: a simple explanation

The Euler Buckling instability was the first studied example of bifurcation phenomena, and in itself involves a spontaneous symmetry breaking. In 1744, the Swiss mathematician Leonhard Euler, derived a formula which shows that there is a critical load for the buckling of a slender column. With any smaller load, the column remains straight and supports it. With any larger load, the least disturbance causes the column to bend sideways with an indefinitely large displacement, i.e. it “buckles”. A column, of course, is simply a common example of a compressional element, like beams, rods, and also filaments.

To better understand this well known phenomenon, let’s consider the simple case sketched in Fig. 6.8. In this situation, a beam that would normally be straight, is hinged at one end (red

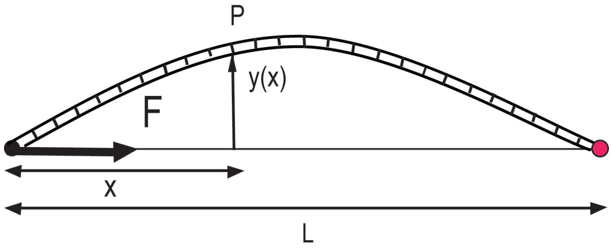

Figure 6.8: Euler buckling instability

dot in the figure), and is held in its bent shape by a force of magnitude F, that pushes on the other end of the rod. Let the deflection of the rod from the straight line to be $y(x)$, where x is the distance from the end where the force is applied. The bending moment $M(x)$ at the point P in the figure, is simply the force F multiplied by the moment arm, i.e. $M(x) = Fy(x)$.

The bending moment is related to the curvature of the bent shape by the *"beam equation"*, which states that

$$\frac{YI}{R(x)} = M(x) = Fy(x)$$

Here Y is Young's modulus, I is the moment of inertia of area of the cross-section of the beam, and $R(x)$ is the radius of curvature of the bent rod. For small deflections, the second derivative is the reciprocal of the radius of curvature, so we can take $1/R(x) = -d^2y/d^2x$ (the minus sign because the curvature is downward), and we get

$$\frac{d^2y}{d^2x} = -\frac{F}{YI}y(x) \tag{6.1}$$

which is just the differential equation of a sine wave. The interpretation of this result is that, for small deflections, the curve of such a bent beam is a sine curve. Since the ends of the rod are nodes of the sine wave, the "wavelenght" λ must satisfies the relation

$$\lambda = \frac{2L}{n}$$

with $n = 1, 2, 3....$ If the bending is small, the distance L between the ends is just twice the unbent length of the rod. So the equation for the curve is

$$y(x) = A\sin(\pi nx/L)$$

Taking the second derivative, we get

$$\frac{d^2y}{d^2x} = -\frac{n^2\pi^2}{L^2}y \tag{6.2}$$

Comparing this to Eq. 6.1, and putting n=1, we can see that the minimal force to bend the rod is

$$F_c = \frac{\pi^2 YI}{L^2}$$

Note that for small bending the force is independent of the bending displacement $y(x)$.

We have, then, the following result physically: F_c, often called "Euler force", is the force above which the beam is unstable and suddenly bends a large amount, buckling. It is found from practice that this theory gives good results for columns and filaments that are more than 30 times longer than wide. As one can clearly see, F_c is proportional to $1/L^2$, so the supporting capacity of a column decreases rapidly with an increase in length. Moreover, looking at the equation for the bending moment $M(x)$, it is possible to see that $M(x)$ increases with the displacement $y(x)$, meaning that any buckling merely encourages further buckling. This explains why such failure is catastrophic.

6.4 Hydrodynamic Buckling

Of course, everything discussed above is valid only for small bending of the beam. When the displacement gets large the approximation $1/R(x) = -d^2y/d^2x$ is no more valid. To find the force necessary to bend the rod for a large deformation of the beam, we should proceed in a more detailed and correct way, taking into account the complete energy functional of the rod. This more general description is also useful because it allows us to derive the buckling phenomenon for different systems, for example for a filament immersed in a viscous liquid like in the case of *Acetobacter* cellulose chains.

Our aim in this section is to derive the mathematical conditions that determine the buckling transition for a semiflexible filament which is moving in a fluid with a velocity $\mathbf{v}$. Our idea is that the elongation of the cellulose chain from the bacterial catalytic site is able to generate, when the chain approaches a critical length L_c, an instability similar to the one described by Euler for the bending of columns. However, in this case, differently from Euler buckling, there is no constant force pushing the end of the filament. Rather, what determines the buckling instability, is the viscous drag that the fluid exerts on the elongating filament itself.

To understand this concept more easily, remember that to make a rod of length L move in a fluid of viscosity η with a tangential velocity $v_{\parallel}$, it is necessary to apply a pushing force equal to:

$$F = v_{\parallel}\xi_{\parallel}L$$

where, according to the slender-body theory (105), the tangential friction coefficient, $\xi_{\parallel} = 2\pi\eta/[\ln(2L) - 0.5]$. As you can see from this formula, the greater the length of the rod L, bigger the force you have to apply to maintain the velocity $v_{\parallel}$. Imagine now a filament that is elongating in a viscous medium with a constant velocity, like, for example, a cellulose chain being polymerized by *A. Xylinum*. At the beginning the filament is very short, and the resisting friction force it experiences is very small. However, when the length reaches a certain critical value L_c, the viscous force is so big to hydrodynamically "buckle" the filament, in the same way as was discussed previously for the Euler instability.

In the following paragraphs we mathematically derive this critical length, and we demonstrate that the hydrodynamic buckling can serve as an explanation for the breaking of symmetry that occurs during the polymerization process of *A. Xylinum*, and also as a basic phenomenon to understand the longitudinal motion of this bacterium .

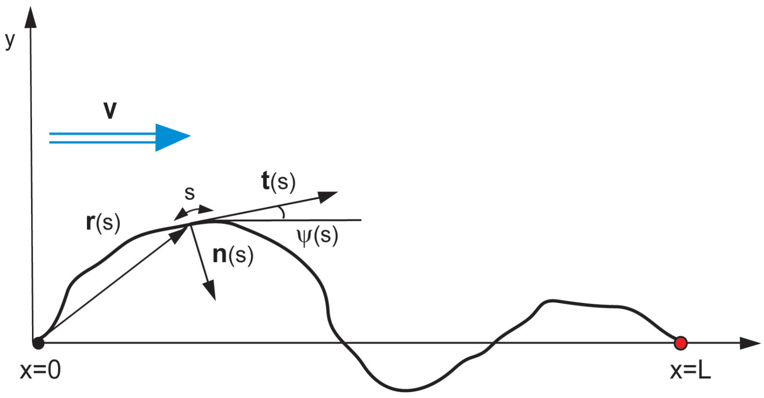

Figure 6.9: Hydrodynamic buckling

6.4.1 Energy functional

The functional governing the internal energy of a semiflexible filament of fixed length L has the following expression:

$$G = \int_0^L \left[\frac{k}{2}\dot{\psi}^2 + \frac{\Lambda(s)}{2}\dot{\mathbf{r}}^2\right] ds \tag{6.3}$$

where we have indicated with k its bending modulus. In this picture the shape of the filament is described by the coordinates $\mathbf{r}(s)$ and $\psi(s)$ as functions of the arc length s, where $\mathbf{r}(s)$ is the vector that points to s and $\psi(s)$ is the angle between the filament tangent $\mathbf{t}(s)$ and the x-axis (Fig. 6.9). The first term in the functional corresponds to the usual elastic energy of the filament, while in the second term $\Lambda(s)$ is a Lagrange multiplier used to enforce the incompressibility constraint $\dot{\mathbf{r}}^2 = 1$, which ensures that s is the arc length. For simplicity in the following we will consider only planar deformations.

In order to derive the buckling dynamics for a semiflexible filament immersed in a fluid, we have to determine the variation δG with respect to $\delta\mathbf{r}$. Recalling the following relations:

$$\begin{aligned} \dot{\mathbf{r}} &= \mathbf{t} && (6.4)\\ \dot{\mathbf{t}} &= \dot{\psi}\,\mathbf{n} && (6.5)\\ \dot{\mathbf{n}} &= -\dot{\psi}\,\mathbf{t} && (6.6) \end{aligned}$$

where $\mathbf{n}$ is the filament normal (Fig. 6.9), we finally arrive at the expression (106):

$$\frac{\delta G}{\delta \mathbf{r}} = \partial_s[k\,\ddot{\psi}\,\mathbf{n} - \tau\,\mathbf{t}] \tag{6.7}$$

where $\tau = (\Lambda + k\,\ddot{\psi}^2)$ plays the role of a physical tension. The variation δG has contributions at the boundaries (that come from the integrations by parts) that can be interpreted as externally applied forces $\mathbf{F}$ and torques T acting at the ends.

In $s = 0$

$$\begin{aligned} \mathbf{F}(0) &= k\ddot{\psi}\,\mathbf{n} - \tau\,\mathbf{t}\\ T(0) &= -k\dot{\psi} \end{aligned}$$

while in $s = L$

$$\begin{aligned} \mathbf{F}(L) &= -k\ddot{\psi}\,\mathbf{n} + \tau\,\mathbf{t} \\ T(L) &= k\dot{\psi}. \end{aligned}$$

These value will be fixed by the initial conditions of the problem.

6.4.2 Dynamic equations

Now that we have the expression for the functional derivative $\frac{\delta G}{\delta \mathbf{r}}$, we can focus on the dynamics of an elastic filament immersed in a low Reynolds number fluid. In fluid mechanics the Reynolds number Re=$\rho v l/\eta$, is the ratio of inertial forces ($v\rho$) to viscous forces (η/l) and is used to determine whether a flow is laminar or turbulent. Here v is the fluid velocity, ρ is the fluid density, η the fluid viscosity and l is a characteristic length of the system. Laminar flow occurs at low Reynolds numbers (Re < 2100), where viscous forces are dominant, and is characterized by smooth, constant fluid motion. Turbulent flow, on the other hand, occurs at high Reynolds numbers (Re> 4000) and is dominated by inertial forces, producing vertexes and other flow fluctuations.

If we are interested in studying the dynamics of biological filaments, we are concerned nearly always with the low Reynolds number regime. In fact, because of their size and typical velocities, inertia is essentially irrelevant for these kind of systems. It is thus possible to use a simplified description for the filament dynamics, namely through an over-damped (negligible mass) equation of motion, that can be written as:

$$(\partial_t \mathbf{r} - \mathbf{v}) = -\left(\frac{1}{\xi_\perp}\mathbf{nn} + \frac{1}{\xi_\parallel}\mathbf{tt}\right) \cdot \frac{\delta G}{\delta \mathbf{r}}. \tag{6.8}$$

Here, $\partial_t \mathbf{r}$ is the local velocity of the polymer, and $\mathbf{v}$ is any background velocity that may be present in the problem. Following slender-body theory, the effect of the surrounding fluid is taken as a drag force that is proportional and opposite to the local velocity. This is anisotropic due to the elongated shape of the filament. We therefore require two different local friction coefficients, $\xi_\parallel$ and $\xi_\perp$, for tangential and normal motion, respectively: $\xi_\parallel$ is associated with the projector **tt** along the tangent vector **t**, while $\xi_\perp$ corresponds to the projector **nn** and acts along the normal vector **n**. Each of these coefficients (*per unit length*) is intended to be constant, i.e. in the following we will neglect their weak logarithmic dependence on the length L of the filament.

In order to study the hydrodynamic buckling for a semiflexible filament of fixed length L, we start by focusing on an initially straight polymer that is anchored with one end in $x = L$. We then may consider either forcing the filament by longitudinally moving the anchor with a negative velocity $\mathbf{v} = -v\,\hat{\mathbf{e}}_x$), or moving the fluid relative to the polymer with a positive velocity, $\mathbf{v} = v\,\hat{\mathbf{e}}_x$. In the following, for sake of simplicity, we are going to solve the Eq. 6.8 with the boundary conditions referred to the latter case. However, the equivalence of the two systems will be provided by the comparison of the theoretical results with the simulations that will be presented later on.

Substituting the expression for $\delta G/\delta \mathbf{r}$ found in the previous section we have:

$$\partial_t \mathbf{r} = \frac{\mathbf{n}}{\xi_\perp}(-k\dddot{\psi} + \dot{\psi}\tau) + \frac{\mathbf{t}}{\xi_\parallel}(k\ddot{\psi}\dot{\psi} + \dot{\tau}) + \mathbf{v}. \tag{6.9}$$

The tension τ is determined by the constraint of incompressibility $\partial_t \mathbf{t}^2 = 2\mathbf{t}\cdot\partial_t \mathbf{t} = 0$. This condition leads to a differential equation for the tension profile (106):

$$\ddot{\tau} - \frac{\xi_\parallel}{\xi_\perp}\dot{\psi}^2\tau = -k\partial_s(\dot{\psi}\ddot{\psi}) - k\frac{\xi_\parallel}{\xi_\perp}\dot{\psi}\dddot{\psi} + \dot{\psi}v_\perp - \dot{v}_\parallel. \tag{6.10}$$

where $v_\parallel$ and $v_\perp$ are the component of the fluid velocity along the tangential and normal direction, respectively.

6.4.3 Linearized equation

Let's consider the case of a filament of length L initially lying along the horizontal axis and hinged in $x = L$. Let's assume that the velocity of the fluid runs along the x-axis too, i.e. $\mathbf{v} = v\,\hat{\mathbf{e}}_x$, as depicted in Fig. 6.9. At the linear order, for small deviation from a horizontal line, $s \simeq x$, $\hat{\mathbf{t}} \simeq \hat{\mathbf{e}}_x$, $\hat{\mathbf{n}} \simeq -\hat{\mathbf{e}}_y$, $\dot{\psi} = \ddot{y}$, and we can rewrite the Eqs. 6.9 and 6.10 as:

$$\begin{aligned} \xi_\perp \partial_t y &= (-k\ddddot{y} + \tau\,\ddot{y}) \\ \xi_\parallel \partial_t x &= (\dot{\tau} + v\,\xi_\parallel) \end{aligned}$$

and

$$\ddot{\tau} = 0 \tag{6.11}$$

Since the filament is hinged in $x = L$ we have $\partial_t y(L) = \partial_t x(L) = 0$, from which it follows that $\dot{\tau}(L) = -v\,\xi_\parallel$. This result, together with eq.(6.11), leads to $\dot{\tau}(x) = -v\,\xi_\parallel$. Now we look at the boundary conditions at the free end. Since there are no external forces acting in $x = 0$, we find from eq. (6.8) that $(\mathbf{F}(0)\cdot\hat{\mathbf{e}}_x) = -\tau(0) = 0$, that leads us to the expression for the tension behaviour along the filament, $\tau(x) = -v\,\xi_\parallel\,x$. Substituting this result in eq. (6.11) we finally obtain:

$$\xi_\perp \partial_t y = (-k\ddddot{y} - v\,\xi_\parallel\,x\,\ddot{y}) \tag{6.12}$$

This is the simplest linearized expression we will work on. As we intuitively expect, $y(x,t) \equiv 0\ \forall x,t$ is clearly a trivial solution of this equation, corresponding to the completely stiff horizontal configuration of the filament. This solution is however stable only for small values of v. In fact, as in normal buckling phenomena, when the critical force acting on the free end of the filament exceeds a critical values F_c, the filament buckles. In our case, as already said, the force is due to the viscous drag, and consequently it increases as the length L of the filament or the fluid velocity v increase. For a filament of fixed length L, at a certain critical velocity v_c the viscous force becomes so strong to buckle the rod. This case corresponds to a non-trivial solution for $y(x,t)$.

6.4.3.1 Stationary solution

It is possible to compute the exact buckling length searching for a stationary solution of equation (6.12). Setting the *lhs* equal to zero and introducing the new coordinate $z = (\frac{v\xi_\parallel}{k})^{1/3}x$, equation (6.12) reads simply as:

$$-\ddddot{y} - z\,\ddot{y} = 0 \tag{6.13}$$

We are going to solve this fourth order derivative equation with the following boundary conditions:

$$y(0) = y(l) = \ddot{y}(0) = \ddot{y}(l) = 0 \tag{6.14}$$

where $l = (\frac{v\xi_\parallel}{k})^{1/3}L$. The first two conditions set the positions of the first and last point of the filament: basically, requiring no vertical displacement to occur at both ends, we are constraining the first and last point of the rod to slide onto a horizontal guard-rail. Therefore the buckling transition will change the shape of the filaments as shown in Fig. 6.8. On the other hand, the third and the fourth boundary conditions assure that there are no torques acting on the ends of the rod, i.e. the filament is free to pivot around them. With the change of coordinates the velocity v has disappeared, so from now on, instead of focusing on the critical velocity v_c, we shift our attention to the critical buckling length l_c. Our aim is to search for those values of l_c that, for a constant velocity v of the surrounding fluid, bring to a non-trivial solution of equation (6.13). In order to do that, we first solve with Mathematica eq. (6.13) with only two boundary conditions, the first and the third. We are then left with a solution that looks like:

$$y(z) = c_1\, f(z) + c_2\, g(z) \tag{6.15}$$

where c_1 and c_2 are constants to be determined by mean of the other two boundary conditions. In this way we obtain a linear system in c_1 and c_2 that can be solved exactly. The first non-trivial solution is obtained for a value of $l_c = 2.66$. Our estimate for the critical hydrodynamic buckling length L_c for a filament subjected to a tangential low Reynolds number fluid, with velocity v, is thus:

$$L_c = 2.66 \left(\frac{k}{v\xi_\parallel}\right)^{1/3} \tag{6.16}$$

.

6.4.3.2 Linear stability

Another approach to study the hydrodynamic buckling transition, is to look at the linear stability of eq. (6.12). To do so, we assume the solution to be an oscillatory function $y(x,t) = A(t)\; e^{iqx}$ and we search for those values of the wave number q that yields to an unstable solution. A more rigorous argument would be to consider a perturbation which is not a sinusoidal wave but an eigen function of the linear operator. However, this is beyond the aim of this section and we will not delve into unnecessary details.

With the substitution we obtain:

$$\partial_t A\, e^{iqx} = \frac{1}{\xi_\perp}(-k\, q^4 A\, e^{iqx} + v\, \xi_\parallel\, x\, q^2 A\, e^{iqx}) \tag{6.17}$$

Setting $\omega(q) = -kq^4 + v\xi_{\|}xq^2$ and cancelling the exponential we are left with the expression:

$$\partial_t A = \omega(q)\, A \tag{6.18}$$

which has a solution

$$A(t) = A(0)\, e^{\omega(q)t} \tag{6.19}$$

This solution in stable and converges to zero only for negative values of $\omega(q)$ Therefore, we can say that the filament buckles whenever $\omega(q) > 0$, i.e. $q^2 < \frac{v\,\xi_{\|}\,x}{k}$. For a filament of length L with both ends fixed in $y = 0$, the allowed wave numbers are only the ones that satisfy the relation $q = n\pi/L$, with n being an integer. This means that the filament buckles whenever

$$L^2 > \frac{\pi^2 k}{v\,\xi_{\|}\,x} \tag{6.20}$$

where since we are interested in the first non-trivial solution we have put $n = 1$. The expression (6.20) is a bit nasty since it depends on the unknown quantity x. To get rid of it we repeat the same procedure described at the beginning of this section, for the symmetric case of our problem, the one in which we have the filament hinged in $x = 0$ and subjected to a fluid velocity $\mathbf{v} = -v\,\hat{\mathbf{e}}_x$. For symmetry considerations we have to find the same buckling length L_c.

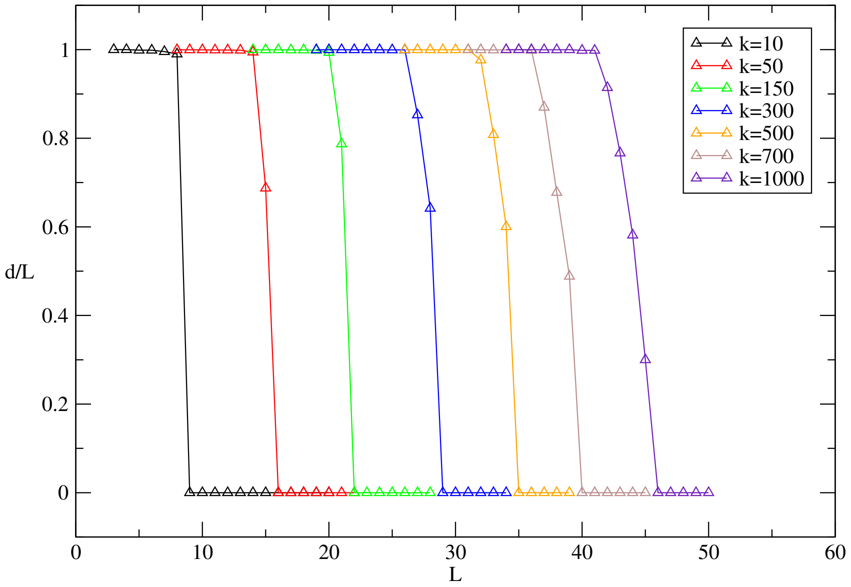

Figure 6.10: Buckling transitions for different values of the bending parameter k

Doing all the calculations for the symmetric case we finally arrive at a similar expression, except for the fact that instead of x we have now $(L-x)$. This implies that in this case $\omega(q) > 0$ whenever $L^2 > \frac{\pi^2 k}{v\,\xi_{\|}\,(L-x)}$.

Since the two expression have to be satisfied at the same time, the only possibility is to take $x = (L-x) = L/2$. This bring us to the final result:

$$L_c = (2\pi^2)^{1/3}\left(\frac{k}{v\xi_{\|}}\right)^{\frac{1}{3}} = 2.7\left(\frac{k}{v\xi_{\|}}\right)^{\frac{1}{3}} \tag{6.21}$$

which is consistent with the result (6.16) obtained in the previous section.

6.4.4 Simulating the hydrodynamic buckling

To further check the correctness of our theoretic results, we have implemented a numerical simulation that reproduces the hydrodynamic buckling of a semiflexible filament which moves in a low Reynolds number fluid with a tangential velocity v. Besides confirming the expected values for the buckling lengths found previously , this simple numerical scheme serves also as a basis for the more complex many-body simulation, which will be presented in the next section.

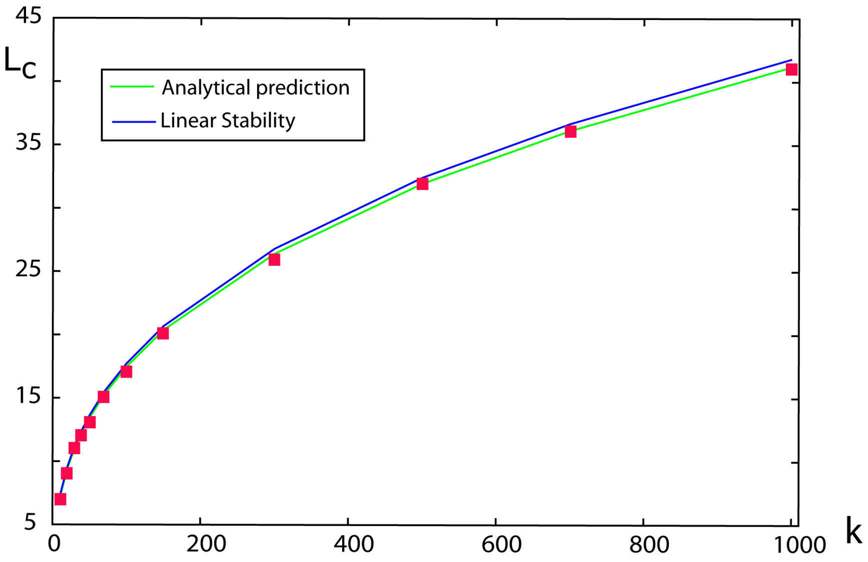

Figure 6.11: Theoretical (Eqs. 6.16 and 6.21) versus simulations results

In the simulation we have used a particle model to solve Eq. (6.8) numerically, using an approach similar to Molecular Dynamics (MD), the so called "Brownian Dynamics" (BD) technique. The BD simulation technique is a mesoscopic method in which explicit solvent molecules are replaced by a stochastic force. The technique takes advantage of the fact that there is a large separation in time scales between the rapid motion of solvent molecules and the more sluggish motion of polymers or colloids. At the core of a BD simulation is a stochastic differential equation which is integrated forward in time to create trajectories of molecules. The details of the algorithm are described in Appendix B.

In our model, time is discretized and the filament is described as a set of n particles of diameter σ rigidly connected by $n-1$ links. The stochastic force, that depends on the temperature T, is the source of fluctuations that makes the buckling transition possible. In fact, in absence of any noise ($T=0$), a straight filament pushed along its longitudinal direction won't buckle at all in a numerical simulation, because there would be no transversal components of the force to bend it. The role of the stochastic force is thus to introduce the small fluctuations necessary to break the symmetry. However, in order to compare the numerical results to the theory, we have performed the simulations with $T \to 0$. This also makes an accurate evaluation of the buckling lengths easier, because the data are less noisy and the transitions more pronounced.

We consider a filament of fixed length $L = n\sigma$, initially lying along the horizontal direction, that is longitudinally moving with a constant velocity v in a low Reynolds number fluid. Following the boundary conditions given by Eq. (6.14), both ends of the filament are constrained to slide on a horizontal guide rail and they can't experience any vertical displacement. In addition, the ends of the filaments are not clamped, i.e. there are no torques acting on them.

We define our order parameter $\psi = d/L$, as the ratio of the distance $0 < d < L$ between the ends, and the contour length L of the filament. At the beginning of the simulation the rod is straight, i.e. $\psi = 1$. Then the filament is pushed in the fluid with a velocity v for a time t until it reaches a stationary configuration. If the filament is very short, or very stiff, then the order parameter of the stationary configuration remains always around the value $\psi \simeq 1$. For greater filament lengths L, or a smaller bending constant k, the rod buckles, and the order parameter $\psi \to 0$. In Fig. 6.10, each curve shows the result of a single run of simulations, in which we have measured the value of the order parameter ψ as a function of the filament length L, with the stiffness k, the velocity v and the viscosity η of the fluid kept constant. The critical buckling length L_c is identified as the last value of L for which $\psi = 1$. Repeating the same run of simulations for different values of the bending parameter k, we obtain all the curves displayed in Fig. 6.10.

The buckling transition is very pronounced: the value of the order parameter drops very sharply form 1 to 0. If we plot the critical lengths versus the bending parameter k, we can compare the simulation with the theoretically predicted behaviour of the previous sections (Fig. 6.11). As one can clearly see, the agreement is excellent.

6.4.5 Discussion on results

The persistence length L_p of a single cellulose chain in aqueous solution has been estimated by MD simulations (107), which provide an upper limit of $L_p = 14.5 \pm 1$nm. The persistence length is related to the bending modulus k by the relation $L_p = k/K_B T$, and at room temperature this corresponds to a value of $k = 5.6\ 10^{-29}$Nm^2. The parallel drag coefficient of a filament, neglecting the weak logarithmic dependence on its length, is $\xi_{\|} \simeq 2\pi\eta$, where η is the viscosity of the medium in which the filament is dipped. In our case we have $\eta = 1$cP (viscosity of water) so that $\xi_{\|} \simeq 6.2\ 10^{-3}$cP. We put the velocity at which the filament is dipped into the medium equal to the polymerization velocity of cellulose, $v = 12\ 10^{-8}$m/s. Substituting these values in the Eq. 6.16, we find that the buckling length at which a polymerizing cellulose chain is bent is $L_c \simeq 1.1\ 10^{-6}$m. If we repeat the same procedure for the non-crystallized bundle of $n = 10$ glucan chains extruded form a single CSC subunit, we find a critical length of $L_c^{bundle} = 2.66\ [(10k)/(v\xi_{\|})]^{1/3} = 2.4\ 10^{-6}$m.

According to these results, an elongating cellulose chain extruded from the bacterium buckles when its length is already of the order of microns. If this was true, it should be possible to observe a terminal structure (of the order of μm) pending at the end of each ribbon structure. This band-structure would correspond to the part of fibers expelled perpendicularly from the bacterium before the buckling transition had taken place (Fig. 6.17). Interestingly enough, some experiments show that this is actually the case: as noted by Brown (18), and as shown in Fig. 6.12, in some case it is possible to see "lateral projections" attached at the end of the ribbon. However, these projections have an extension of the order of hundreds of nanometers, i.e. much smaller than our expected buckling length.

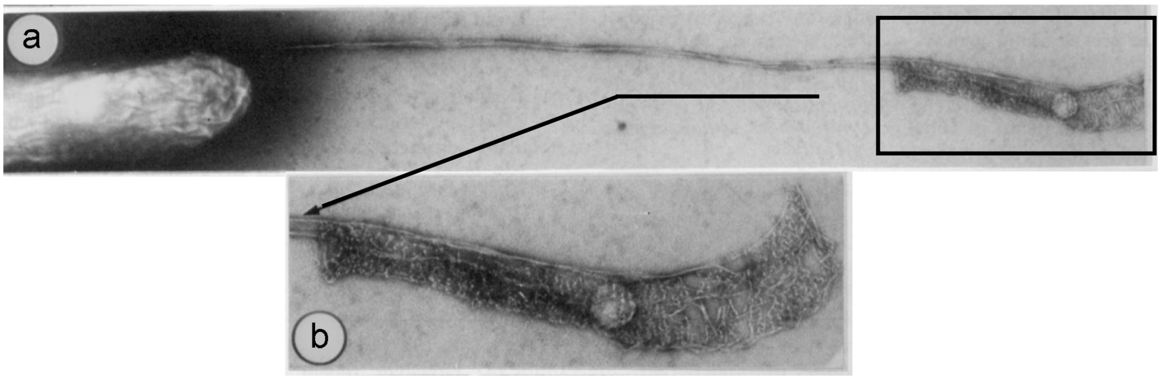

Figure 6.12: Lateral projection at the end of the cellulose ribbon

A possible explanation for this inconsistency is that we have carried out our theory for a single filament, while we know that Acetobacter polymerizes many cellulose strands. As we will learn form the next sections, the influence caused by the presence of many filaments on the "real" buckling length could be crucial. Moreover, it is also probable that the size of the band documented by Brown is smaller than the theoretical one, because of the crystallization effects. In fact, once the ribbon starts to form, it is possible that the crystallization process creates a sort of "zipping" effect, that manages in transforming part of the already deposited band structure into the ribbon one. Last, we have to keep in mind that the theoretical buckling length strictly depends on the polymerization velocity of the cellulose strands. It is reasonable to believe that at the moment of extrusion, the elongation velocity would be much higher than the final "stationary": this would imply that the time necessary for the chains to associate and crystallize could limit the rate of polymerization.

6.4.6 Is this enough?

Now that we have identified a possible mechanism capable of breaking the symmetry in the polymerization process of *A. Xylinum*, we have to face another problem. Let's recall, in fact, that the bacterium produces tens of CMFs, i.e. hundreds of cellulose chains. Each of these chains, according to our results, experiences hydrodynamic buckling, and after a certain critical length bends in a particular direction. If the chains were completely independent, the bending directions would be different from chain to chain, since there is no preferred orientation for the buckling transition. In a 3-dimensional environment, this means that the probability that the filaments encounter each other and then crystallize forming the ordered ribbon, would be almost zero.

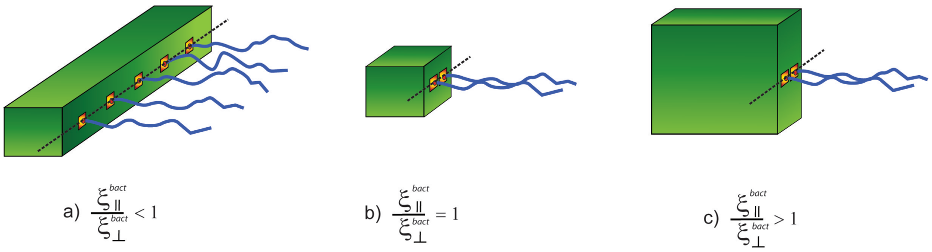
a) $\frac{\xi_{\parallel}^{bact}}{\xi_{\perp}^{bact}} < 1$ b) $\frac{\xi_{\parallel}^{bact}}{\xi_{\perp}^{bact}} = 1$ c) $\frac{\xi_{\parallel}^{bact}}{\xi_{\perp}^{bact}} > 1$

Figure 6.13: Possible shapes of the 3d-cuboidal body depending on the ratio on the drag coefficients

This consideration brings us to the conclusion that the simple buckling instability it is not enough to explain the formation of the ribbon and the longitudinal motion of the bacterium. What we are still missing, is a mechanism which is able to coordinate the bending transition of all the filaments, in order to orient them in the same direction for the correct assembly of the ribbon to be achieved.

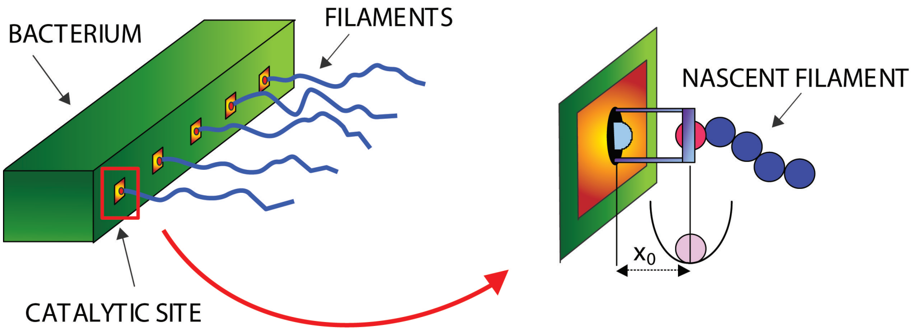

Figure 6.14: Model for the catalytic sites on the bacterial surface

In the next part of this chapter, we would like to demonstrate, through the results of a BD simulation, that this role is automatically performed in the system by what are called the “hydrodynamic interactions” (HI) among filaments. HI are a general effect concerning objects immersed in a solvent. They are due to the perturbation of the fluid motion induced by the presence of bodies in the solvent. This perturbation depends only on the distance between the objects in the fluid, and has big repercussions on the motion of the bodies themselves. In the next section we will examine this effect in detail, through the building of a many-body BD simulation, which clearly elucidates how the hydrodynamic coupling is able to coordinate the buckling transitions of the elongating filaments.

6.5 Coupling filaments by hydrodynamics: a BD simulation

To fully explore the motion mechanism of *A. Xylinum*, together with the coordination process of the elongating strands, we need to simultaneously take into account: 1) the dynamics of many filaments; 2) the presence of the bacterium itself. We do this with a rather complex BD simulation. The details of this computational method are discussed in Appendix B.

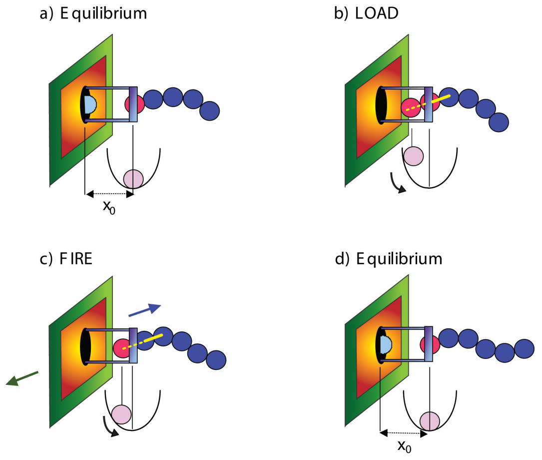

Figure 6.15: The Load and Fire mechanism

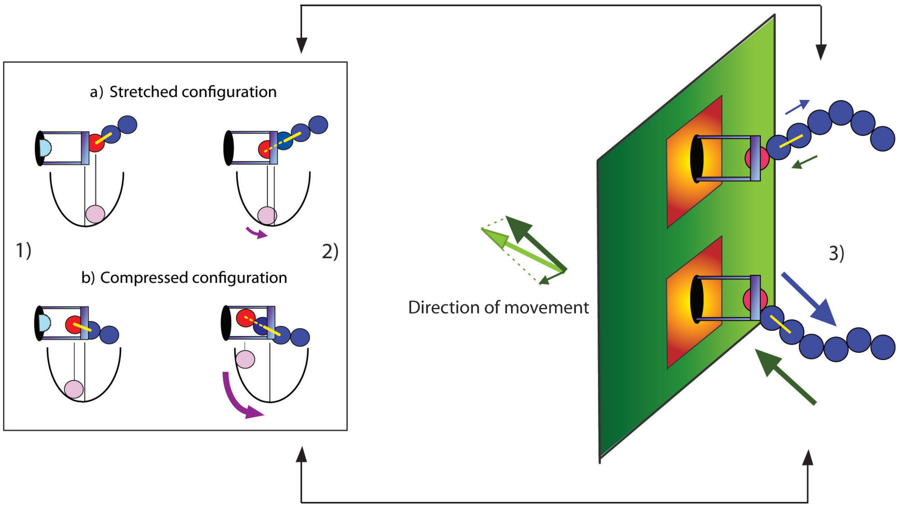

Figure 6.16: The final direction of motion of the bacterium depends on the magnitude and the direction of the pushing forces exerted by the filaments

The simulation is focused on two main objects: the elongating filaments and the bacterium. The bacterium is modeled as a 3d-cuboidal body, endowed with a linear array of catalytic sites anchored along the middle-line of one of its lateral surfaces (Fig. 6.14a). The catalytic sites are surface-bound, non-motile objects, and correspond to the *loci* where the polymerization and elongation of filaments occur. The number of catalytic subunits coincides with the number of filaments. We model these polymers as inextensible semiflexible chains of beads, which are connected to the bacterium through the catalytic sites (Fig. 6.14b).

In the simulation, what determines the shape of the 3d-cuboidal body are the drag coefficients $\xi_{\parallel}^{bact}$ and $\xi_{\perp}^{bact}$, respectively along the directions that run parallel and perpendicular to the line which joints the catalytic sites. In our treatment we assume that the drag coefficients corresponding to the two perpendicular directions are equal, and we will refer to them as $\xi_{\perp}^{bact}$. Depending on the value of the ratio $\xi_{\parallel}^{bact}/\xi_{\perp}^{bact}$, one can have the three different situations shown in Fig. 6.13. Given the elongated shape of *A. Xylinum*, in the next sections will mainly focus on the case in which $\xi_{\parallel}^{bact} < \xi_{\perp}^{bact}$.

Another clarification we need to make is that the bacterium is modeled as a “passive” body. This means that the bacterial movement can occur only as a reaction to the motion and elongation of the filaments, as will be explained in the next section. On the other hand, the polymers are “active” objects: the Brownian Dynamics algorithm governing their motion, in fact, takes into account the thermal fluctuations of the environment as well as the interaction effects due to their reciprocal presence in the fluid. The dynamics of the polymers, coupled to the elongation process, is thus the only motor of the bacterium.

Before focusing on the mechanism involved in the filament-elongation process, we need to better understand the role of the catalytic sites: as already said, their main purpose is to connect the filaments with the bacterium. However, the catalytic units are not modeled as real complex objects, but rather they accomplish their task simply by fixing the equilibrium position of the tips of the filaments. In particular, in the simulation, the catalytic sites are surface bound clamps, whose extremity is separated from the bacterial surface by a distance x_0 (Fig. 6.14b). The clamps are connected with the polymers via harmonic forces: the first bead of each filament lies in a potential well centered at the extremity of the corresponding catalytic site. As shown in Fig. 6.15, this implies that the system (filaments+bacterium) is in equilibrium only when the position of the tip of each polymer exactly coincides with the location of its complementary catalytic site.

Our simulation is able to consistently model the motion of a body immersed in a fluid and pushed by the polymerization forces of elongating polymers. To explain how filaments can elongate while remaining strongly tethered to the motile surface, and how their growth is able to generate a motile force, we have used a minimal version of the mechanochemical model *Lock, Load and Fire* proposed by Dickinson *et al.* for actin polymerization. Since in our simulation we neglect, for sake of simplicity, the chemical details of the original model, we will refer to our elongation mechanism as the “Load and Fire”.

6.5.1 Load and Fire

The *Load and Fire* model entails two main steps: 1) loading of a new polymer bead in the back of the catalytic site; 2) subsequent firing of the loaded bead outside of the catalytic site and shifting of the filament’s tip. For a better comprehension of the *Load and Fire* model it is sufficient to look at Fig. 6.15. In the following we will focus on the dynamics of one single filament, since the same reasoning can be done for all of the N bacterial strands. We assume the polymerization event to occur with a fixed rate k_{on}.

The reaction begins with the filament in its equilibrium configuration (Fig. 6.15a), with its first bead at a distance x_0 from the bacterial surface. As soon as the polymer starts feeling the thermal fluctuations, the brownian motion that it experiences changes its position, thus displacing the filament from the straight horizontal configuration. After a time $1/k_{on}$ the first step of the polymerization process happens: a new bead, schematically represented in the cartoon by the additional light-blue monomer, is moved to the back of the catalytic unit and it is subsequently attached to the tip of the filament (Fig. 6.15b). The new bead is always added at the growing tip along the direction defined by the second and third bead of the polymer, as shown in Fig. 6.15b/c. Once the attachment event is carried out, the second elongation's step occurs: due to the harmonic constraint between filament and clamp, the new polymer's tip is suddenly strongly attracted (fired) to its natural equilibrium position, i.e. the location of the catalytic site (Fig. 6.15c). This firing process has two main consequences: on one side it causes the filament to elongate and move onward; on the other one, by the action-reaction principle, it provokes the displacement of the catalytic site itself, thus pushing the bacterium backward (remember that the catalytic unit is bacterium-bound). As a result, the reciprocal movement of the bacterium and the filament, occurring as a consequence of the harmonic constraint, happens in the direction defined by the orientation of the filament's tip in that particular moment. When the first bead reaches the location of the catalytic site, equilibrium is finally restored, and the elongation process can start again (Fig. 6.15d).

One thing we should comment on, is the magnitude of the pushing force. The presence of the harmonic coupling makes it depend only upon the distance between polymer's tip and clamp. Therefore, both the direction and the magnitude of the force are related to the instantaneous configurations of the polymers. If the elongation event occurs when the filament is in a "stretched" configuration (Fig. 6.16b), i.e. with its first bead external with respect to the clamp, the attachment event will place the new bead very close to its equilibrium position, and the magnitude of the restoring force will be small. On the other hand, if the polymerization event happens when the filament is in a "compressed" configuration (Fig. 6.16a), i.e. with its first bead internal with respect to the catalytic extremity, then the new monomer will find itself far away from its equilibrium position. The magnitude of the restoring force, consequently, will be very big.

Moreover, we have to keep in mind that we are dealing with N different filaments, and this makes the full-scale situation a bit more complicated than the one depicted in Fig. 6.15. Each of the polymers in fact will push the bacterium along the direction defined, in that moment, by the orientation of its tip. The total force, acting on the center of mass of the body, will thus be an average of the N different orientation of the pushing filaments. Fig. 6.16 shows the very simple case of a body propelled by two polymerizing filaments: each elongation event makes the body move in the direction defined by the vectorial sum of the two polymerization forces.

6.5.2 Brownian motion and Hydrodynamic interactions

So far we have treated the N filaments like independent entities. However, this is not completely correct. Even if there are no external fields or potential to couple the motion of the filaments, this doesn't mean that the polymers are completely independent. In fact, the fluid in which the polymer are immersed, works silently as a coupling factor to correlate their movement.

Imagine to have a body pushed by one single polymerizing filament. The thermal fluctuations that this filament experiences, make it explore the phase space isotropically. This means that the probability to find the polymer's tip oriented in a certain direction is exactly equal to the probability to find it oriented in the opposite direction. Given that, it is reasonable to believe that on average, one single filament will push the bacterium along the direction perpendicular to the catalytic surface.

How do things change when there are more than one polymerizing chain? Well, in absence of interactions among filaments, the situation wouldn't change a lot. Again, on average each of the filaments will push the body perpendicular to the longitudinal axis of the cell. The total force acting on the center of mass of the bacterium will then be the sum of N horizontal forces, and will be horizontal itself. This means that in absence of interactions among filaments, the motion of a body propelled by polymerizing forces is always perpendicular to the longitudinal axis of the cell, just like intuition suggests (Fig. 6.6).

How then do we explain the motion of *A. Xylinum*? Well, what really happens in this case, is that even in absence of external interactions, like Coulomb or Van der Waals, the polymers can strongly influence each other just with their presence, through what are called the "Hydrodynamic interactions". Particles, or polymers, immersed in a fluid, excite long-ranged flows as they move, and similarly move in response to fluid motion. By generating and reacting to a fluid's local velocity, the particles experience hydrodynamic interactions with each other, that can strongly influence their motion even at relatively large separations.

In this particular case, hydrodynamic interactions couple the elongation process of the N filaments. As a result, after an initial transient, the arrangement and the motion of the N polymers begins to be synchronous, and the directions of the N polymerization forces become parallel to each other. Interestingly, this correlation process is so strong that it can coordinate the buckling transition of the filaments, to break the symmetry of the system and make the bacterium propel in the longitudinal direction. We will describe in detail this phenomenon in the next section.

6.5.3 Results

Fig. 6.17 shows 6 frames of our Brownian Dynamics simulation. The simulation starts with $N = 10$ newborn filaments normal to the catalytic surface of the bacterium (Fig.6.17a). Initially, all the strands have the same very short length, and the line that connects the tips of the polymers exactly coincides with the row of the catalytic sites. The system is therefore in equilibrium.

When the simulation is turned on, the filaments start to experience the brownian motion caused by thermal fluctuations, thus shifting from their original equilibrium position. Since the first bead of each polymer is harmonically constrained to the catalytic sites, and hence to the bacterium, the motion of the polymers will have repercussion on the bacterial configuration (Fig.6.17b). With a rate k_{on}, each polymer elongates according to the *Load and Fire* model, and while elongating it pushes the bacterium in the direction identified by the instantaneous orientation of its tip. As you can see from Fig. 6.17, as long as the polymers are very short, they remain all perpendicular to the catalytic surface, pushing the bacterium in the

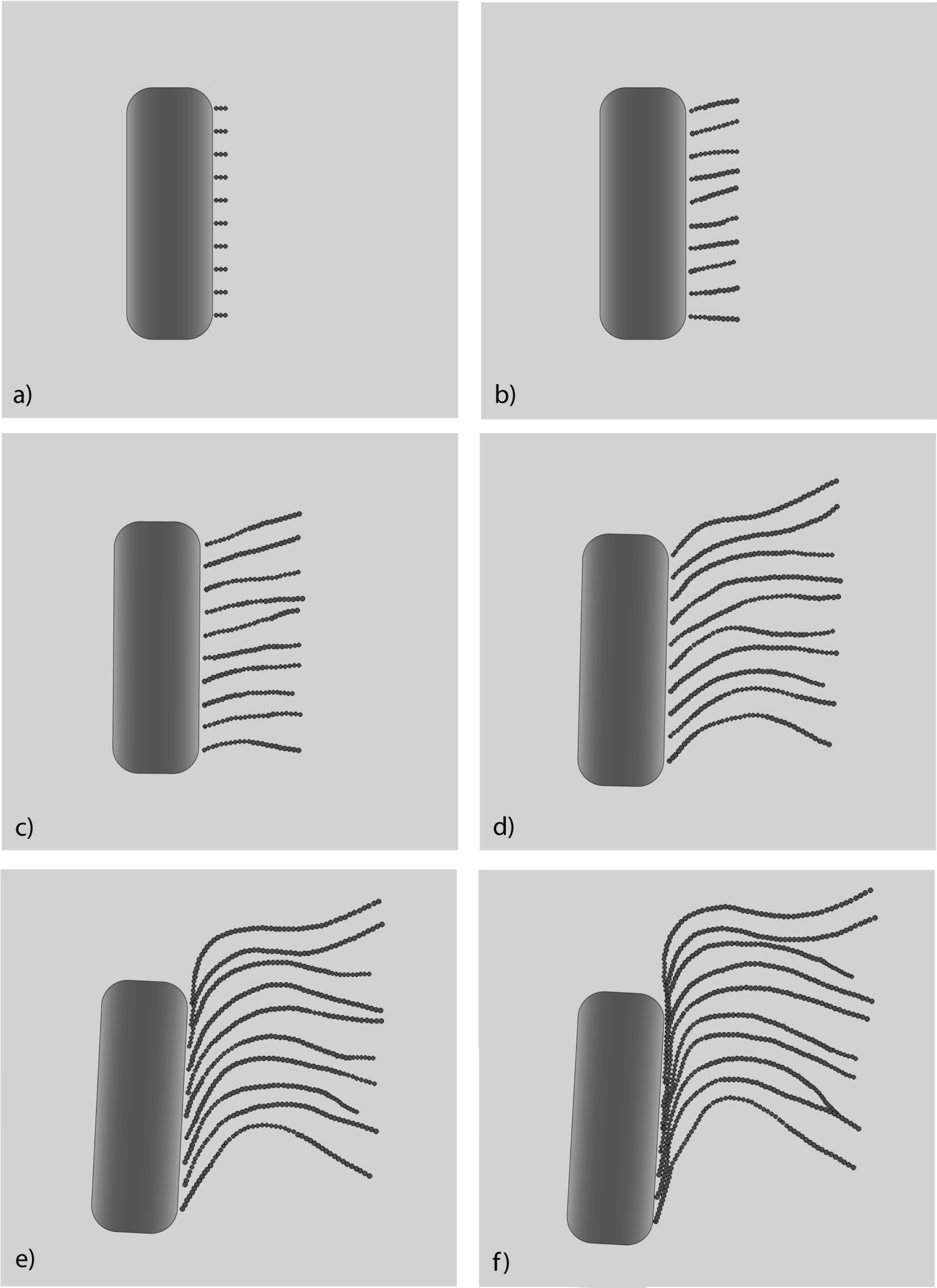

Figure 6.17: Six frames of our simulation: after an initial directed motion, the polymerizing fibers bend due to the hydrodynamic buckling and push the bacterium parallel with respect to his long axis

transversal direction. However, as soon as they reach the critical buckling length, they start bending, deviating from the perpendicular direction (Fig.6.17c/d) . Surprisingly, the Hydrodynamic Interactions among the filaments are so strong to coordinate the buckling transition of all the strands. As a result, the filaments start bending in the same direction, pushing the bacterium cooperatively (Fig.6.17e/f). Because of the constraint of impenetrability between the bacterium and the chains, the filaments end up with their tip parallel to the long axis of the bacterial body. In this configuration, the bacterium is unidirectionally pushed parallel to his long axis, exactly like in Fig. 6.6b.

In particular, if we indicate by M the mass of the bacterium, by m the mass of the polymer's bead, by n_i the number of beads of the i-th polymer and by N the total number of polymers, for the action-reaction principle we have that:

$$F_{bact} = M \cdot a_b = F_{fil} = \sum_{i=1}^{N} F_i = m \sum_{i=1}^{N} n_i a_i \tag{6.22}$$

At the beginning the polymers are very short, i.e. $M >> m\sum_{i=1}^{N} n_i$, and the movement of the bacterium is very limited compared to the motion of the filaments. However, when the fibers become long enough, then $M \simeq m\sum_{i=1}^{N} n_i$, and the movement of the bacterium becomes appreciable.

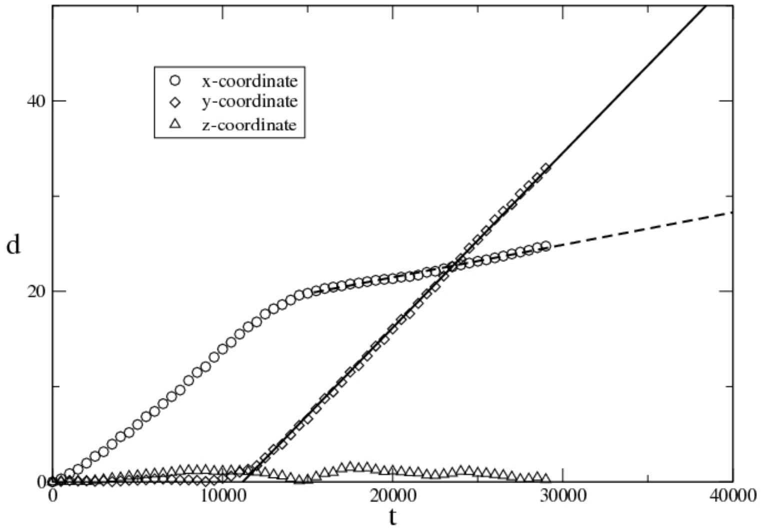

Figure 6.18: Distances covered by the three coordinated (x,y and z) of the center of mass of the bacterium. The lines (solid and dashed) are the linear fit.

6.5.4 Measuring the velocity of the bacterium

In the previous section we have shown how the hydrodynamic effect can make the filaments cooperate to push the bacterium along its longitudinal axis. Now we want to investigate to which extent the number of the polymerized strands influences the velocity of the bacterium. At first, let's focus on a simple case, only 2 elongating filaments. Fig. 6.18 shows the distances covered by the center of mass of the bacterium along the three main directions, x, y and z: here x and y define the plane of movement of the bacterium, y corresponding to the direction parallel to the long axis of the cell. As you can see from the figure, at the beginning of the simulation the bacterium moves mainly transversely, remaining in the same $y-$ and $z-$ position. However, after a certain time, suddenly it begins to turn, the slope of the $x-$curve starts diminishing while the one related to the $y-$coordinate increases. For symmetry reasons, on average the distances covered along the z-directions remains always very small.

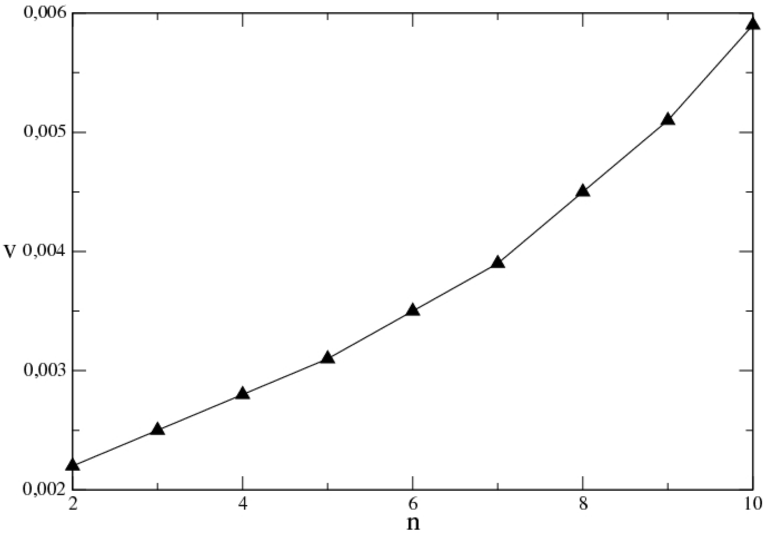

Figure 6.19: Longitudinal velocity of the bacterium for different numbers of polymerized filaments

To measure the velocity of the bacterium along these three directions it is sufficient to calculate the derivative of the curves. As you can see from Fig. 6.18, the bacterium seems to move linearly, with a well defined velocity. However, we expect that at larger times its velocity is no longer constant: as it can be seen from Eq. 6.22, the force acting on the bacterium increases with the total filament's mass, and so its velocity.

Measuring the longitudinal velocities for various simulations each with a different number of filaments, we obtain the plot shown in Fig. 6.19. As intuition expects, the velocity of the bacterium increases if the number of the polymerizing filaments rises up.

6.6 Conclusions

In this Chapter we have focused our attention on the bacterium *A. Xylinum*, a cellulose producing organism that lives in the air-liquid interface and that exhibits a very peculiar motion during the cellulose deposition process. We have shown how the symmetry breaking effect occurring during the bacterial movement is caused by a hydrodynamic coupling between the polymerized cellulose filaments and the liquid in which they are immersed. To further prove our theory, in the second part of the Chapter we have implemented a Brownian Dynamics simulation that is able to consistently model the motion of a body immersed in a fluid and pushed by the polymerization forces of elongating polymers. Our numerical simulation has proved the existence of a symmetry-breaking transition happening during the bacterial motion, and the correlation between the velocity of the bacterium and the number and length of the polymerized filaments. This suggests the possibility of a quantitative comparison with future experiments.

7 Appendices

7.1 Appendix A: The Method of Characteristics

The method of characteristics allows to solve the initial value problem for general linear and quasi-linear first order partial differential equations (PDEs). Consider the first order PDE

$$a(x,t,u)\frac{\partial u(x,t)}{\partial x}+b(x,t,u)\frac{\partial u(x,t)}{\partial t}+c(x,t,u)=0 \tag{7.1}$$

in the two variables (x,t), along with the initial condition

$$u(x,0)=f(x). \tag{7.2}$$

The goal of the method of characteristics is to solve the given PDE by finding curves in the $x-t$ plane that reduce the equation to a simple ODE.
In general, any curve in the $x-t$ plane can be expressed in parametric form as:

$$\begin{cases} x=x(s) \\ t=t(s) \end{cases} \tag{7.3}$$

where the variable s gives a measure of the distance along the curve. In order to label different curves in the $x-t$ plane we need to introduce the parameter p such that

$$\begin{cases} x(s=0)=p \\ t(s=0)=0. \end{cases} \tag{7.4}$$

The variable p thus identifies the initial point of the curve and it is constant along it. This procedure allows us to change the coordinates from (x,t) to (p,s). In this new coordinate system the PDE becomes an ordinary differential equation (ODE) along the generic curve $\{[x(s),t(s)]:0<s<\infty\}$, that is called the *characteristic curve* or just the characteristic.

How do we find the characteristic curves given a generic PDE? Notice that if we choose

$$\begin{cases} \dfrac{dx}{ds}=a(x,t,u) \\ \dfrac{dt}{ds}=b(x,t,u) \end{cases} \tag{7.5}$$

then we have

$$\frac{du}{ds}=\frac{dx}{ds}\frac{\partial u}{\partial x}+\frac{dt}{ds}\frac{\partial u}{\partial t}=a(x,t,u)\frac{\partial u}{\partial x}+b(x,t,u)\frac{\partial u}{\partial t} \tag{7.6}$$

and along the characteristic curves, the PDE transforms into the ODE

$$\frac{du}{ds} + c(x(s),t(s),u(x(s),t(s))) = 0. \tag{7.7}$$

with initial condition

$$u(s=0) = u(x(s=0),t(s=0)) = u(p,0) = f(p). \tag{7.8}$$

Eq. 7.5 will be referred to as the characteristic equations. Assuming that we can solve the ODE 7.7, means that $u(x(s),t(s))$ is known everywhere along this curve, i.e. along the curve $(x(s),t(s))$ defined by a specific choice of the parameter p. Another choice of p gives another curve and therefore another solution of u. In this manner, u can be evaluated at any point P in the $x-t$ plane by choosing the curve, identified by p, that passes through this point, and taking the correct value of s, the distance along the curve. Hence, we can evaluate $u(x,t)$.

7.1.1 General Strategy

The general strategy for applying the method of characteristics to a PDE of the form 7.1 is:

1. Solve the three coupled ODEs:

$$\begin{cases} \dfrac{dx}{ds} = a(x,t,u) \\ \dfrac{dt}{ds} = b(x,t,u) \\ \dfrac{du}{ds} = c(x,t,u) \end{cases} \tag{7.9}$$

   finding the constants of integration by setting

$$\begin{cases} x(0) = p \\ t(0) = 0 \\ u(0) = f(p) \end{cases} \tag{7.10}$$

2. This provides us with the transformation from (x,t) to (p,s)

$$\begin{cases} x = x(p,s) \\ t = t(p,s) \end{cases} \tag{7.11}$$

   and yields a solution for $u(x,t)$ in terms of (s,p). Now that we have a solution $u(p,s)$ we solve for s and p in terms of x and t (using the results of step 1) and substitute these values in $u(p,s)$ to get the solution to the original PDE as $u(x,t)$.

7.2 Appendix B: Brownian Dynamics

The Brownian Dynamics (BD) simulation technique (108; 109) is a mesoscopic method in which explicit solvent molecules are replaced instead by a stochastic force. The technique takes advantage of the fact that there is a large separation in time scales between the rapid motion of solvent molecules and the more sluggish motion of polymers or colloids. The ability to coarse-grain out these fast modes of the solvent allows one to simulate much larger time scales than in a molecular dynamics simulation. At the core of a BD simulation is a stochastic differential equation which is integrated forward in time to create trajectories of molecules. Time enters naturally into the scheme allowing for the study of the temporal evolution and dynamics of complex fluids (e.g. polymers, large proteins, DNA molecules and colloidal solutions). Hydrodynamic and body forces, such as magnetic or electric fields, can be added in a straightforward way. BD simulations are particularly well suited to studying the structure and rheology of complex fluids in hydrodynamic flows and other non-equilibrium situations. In the next sections we begin by recovering the theoretical governing stochastic equation, and subsequently we discretize it and implement it in a BD algorithm.

7.2.1 The Langevin Equation

The BD method is used to describe the dynamics of particles, usually colloids or macromolecules, that undergo Brownian motion in a viscous solvent. Because of their small mass, inertia is essentially irrelevant for these particles, and it is often neglected in the equation of motion. From Newton's Second Law, $\mathbf{F}^{tot} = m\mathbf{a}$, we see that the neglect of inertia means that the total force acting on the particle is always approximately zero. This force is generally composed of three terms: a drag force $\mathbf{F}^{d}$, representing the effect of the viscous solvent through which the particle is moving; a Brownian force $\mathbf{F}^{B}$ due to the random collisions of the solvent with the particle; and a last contribution $\mathbf{F}^{nh}$ that includes all the other non-hydrodynamic forces that can be present in the system, such as external body forces, spring forces, and excluded volume interactions.

For what has just been said, we therefore have that for the particle i:

$$\mathbf{F}_i^{tot} = \mathbf{F}_i^{d} + \mathbf{F}_i^{B} + \mathbf{F}_i^{nh} \simeq 0. \tag{7.12}$$

Let's start considering the case of N *non*-interacting particles in a fluid. In creeping flows (flows with no inertia) and in *absence* of hydrodynamic interactions (free-draining case), the drag force is taken as the Stokes drag on a sphere

$$\mathbf{F}_i^{d} = -\zeta\left(\frac{d\mathbf{r}_i}{dt}\right) \tag{7.13}$$

where $\zeta = (6\pi\eta a)$, being a the radius of the particle and η the viscosity of the fluid, is the drag coefficient. The differential equation governing the motion of the particle then becomes

$$\frac{d\mathbf{r}_i}{dt} = \frac{1}{\zeta}(\mathbf{F}_i^{nh}(\{\mathbf{r}_j\}) + \mathbf{F}_i^{B}(t)) \tag{7.14}$$

and is commonly called the *Langevin equation*. Note that in this relation the non-hydrodynamic force depends on the set of all particle positions $\{\mathbf{r}_j\}$, while the hydrodynamic drag is taken as a constant for all the particles. Eq. (7.14) is a stochastic differential equation, because the Brownian force that act on the particle is extracted from a random distribution. In order for the dynamics to satisfy the fluctuation-dissipation theorem, the expectation values of the Brownian force must be

$$\begin{aligned} < \mathbf{F}_i^B(t) > &= 0 & (7.15) \\ < \mathbf{F}_i^B(t)\mathbf{F}_j^B(t') > &= 2k_BT\zeta\delta_{ij}\delta(t-t')\mathbf{I} & (7.16) \end{aligned}$$

where k_B is the Boltzmann's constant, T is the absolute temperature, δ_{ij} is the Kronecker delta, $\delta(t-t')$ is the Dirac delta function, and $\mathbf{I}$ is the unit second-order tensor. Recalling now the Einstein relation

$$D = \frac{k_bT}{\zeta} \tag{7.17}$$

that relates the thermal motion of the particle, characterized by the diffusion coefficient D, with its response to an external force, we can rewrite the Langevin Equation Eq. (7.14) in the more convenient form:

$$\frac{d\mathbf{r}_i}{dt} = \frac{D}{k_bT}\mathbf{F}_i^{nh}(\{\mathbf{r}_j\}) + \sqrt{2D}\,\xi_i(t) \tag{7.18}$$

where $\xi_i(t)$ is a vector with components extracted from a Gaussian distribution, with average and variance

$$\begin{aligned} < \xi_i(t) > &= 0 & (7.19) \\ < \xi_i(t)\xi_j(t') > &= \delta_{ij}\delta(t-t')\mathbf{I}. & (7.20) \end{aligned}$$

Eqs. (7.14), (7.15) and (7.16) are equivalent to the Fokker-Plank equation description, which is a diffusion equation for the phase-space probability density (110).

7.2.2 Adding Hydrodynamic Interactions

Although the Langevin dynamics correctly describes the behaviour of a single particle (or equivalently of N *non*-interacting particles) immersed in a fluid, it doesn't take into account the effect caused in the solvent by the presence of other molecules. As a particle moves along its trajectory, in fact, it exerts a force on the fluid which changes the velocity field from its undisturbed value. The disturbance velocity changes in its turn the viscous drag force exerted on the other particles. These interaction effects, mediated by the solvent, are called hydrodynamic interactions (HI). As a result, the diffusion coefficient of the particles is no longer a constant (Eq. 7.17), but becomes a configuration-dependent tensor, which will be denoted by $\mathbf{D}_{ij}(\mathbf{r}_i,\mathbf{r}_j)$ (110).

The HI are included in the BD through the use of an interaction tensor $\mathbf{T}_{ij}$, related to the diffusion tensor $\mathbf{D}_{ij}$ by the expression

$$\mathbf{D}_{ij}(\mathbf{r}_i,\mathbf{r}_j) = k_BT\ \mathbf{T}_{ij}(\mathbf{r}_i,\mathbf{r}_j) \tag{7.21}$$

where the indexes refer to particles i and j. Two interaction tensors are generally used to describe the hydrodynamic interactions between particles: the Oseen Tensor (111) and the Rotne-Prager-Yamakawa tensor (RPY) (112). The first one, whose expression reads like

$$\mathbf{T}_{ij}^{Oseen} = \begin{cases} \frac{\delta_{ij}}{\zeta} & \text{if } i = j \\ \frac{1}{8\pi\eta\mathbf{r}_{ij}}\left(\mathbf{I} + \frac{\mathbf{r}_{ij}\mathbf{r}_{ij}}{r_{ij}^2}\right) & \text{if } i \neq j. \end{cases}$$

is the most known and used. However, it results in a non-positive-definite diffusion tensor if particle separations are comparable to the particle radius a. To regularize the singularity in $\mathbf{r}_{ij} = 0$, it is possible to use the RPY tensor,

$$\mathbf{T}_{ij}^{RPY} = \begin{cases} \frac{\delta_{ij}}{\zeta} & \text{if } i = j \\ \frac{1}{8\pi\eta\mathbf{r}_{ij}}\left[\left(\mathbf{I} + \frac{\mathbf{r}_{ij}\mathbf{r}_{ij}}{r_{ij}^2}\right) + \frac{2a^2}{r_{ij}^2}\left(\frac{\mathbf{I}}{3} - \frac{\mathbf{r}_{ij}\mathbf{r}_{ij}}{r_{ij}^2}\right)\right] & \text{if } i \neq j. \end{cases}$$

which modifies the small separation behaviour such that the diffusion tensor is always positive-definite. In analogy with Eq. (7.18), the stochastic differential equation including HI then becomes

$$\frac{d\mathbf{r}_i}{dt} = \frac{1}{k_B T}\sum_{j=1}^{N} \mathbf{D}_{ij}(\mathbf{r}_i, \mathbf{r}_j) \cdot \mathbf{F}_j^{nh}(\{\mathbf{r}_k\}) + \sqrt{2}\sum_{j=1}^{N} \mathbf{B}_{ij}(\{\mathbf{r}_k\}) \cdot \xi_j(t) \tag{7.22}$$

where, again, the ξ_j are random vectors with expectation values given by Eqs. (7.19) and (7.20). The weighting factors $\mathbf{B}_{ij}$ that appear in Eq. (7.22) must be calculated from the diffusion tensor in order to satisfy the fluctuation-dissipation theorem

$$\mathbf{D}_{ij}(\mathbf{r}_i, \mathbf{r}_j) = \sum_{p=1}^{N} \mathbf{B}_{ip}(\{\mathbf{r}_k\}) \cdot \mathbf{B}_{jp}^T(\{\mathbf{r}_k\}). \tag{7.23}$$

This relation can be inverted to calculate the $\mathbf{B}_{ij}$ by Cholesky decomposition. However, a more efficient method has been developed and implemented in BD simulations (108; 109), and will be shown in the next section.

7.2.3 Simulation technique

A BD simulation is performed by integrating the governing stochastic differential equation, (Eq. 7.22), forward in time: the trajectories of the particles in the configuration space are calculated numerically, and are composed of successive displacements each taken over a short time step Δt. Numerical accuracy limits the maximum size of the time step, requiring it to be sufficiently short so that the force on the particles and the gradient of the diffusion tensor are essentially constant during Δt. The stochastic nature of Eq. (7.22) implies that one has to produce many independent trajectories, that will be subsequently averaged together, to obtain the time-evolution of an ensemble-averaged observable.

To simulate the diffusion of N identical interacting Brownian particles, we have to rewrite the displacement equation (7.22) in its discretized form as

$$\mathbf{r}_i = \mathbf{r}_i^0 + \frac{1}{k_b T} \sum_{j=1}^{N} \mathbf{D}_{ij}^0 \cdot \mathbf{F}_j^0 \, \Delta t + \mathbf{R}_i(\Delta t) \tag{7.24}$$

where the subscript $_0$ indicates that the variable has to be evaluated at the beginning of the time-step, the term $\mathbf{F}_j^0$ includes all the *non*-hydrodynamic forces acting on the particle j (for convenience we have dropped the superscript ^{nh}), and $\mathbf{R}_i(\Delta t)$ represents the effect of the Brownian force. The $\mathbf{R}_i$ vectors are configuration-dependent, and are composed of Gaussian random numbers such that their average and variance are given by

$$< \mathbf{R}_i(\Delta t) > \;=\; 0 \tag{7.25}$$

$$< \mathbf{R}_i(\Delta t)\mathbf{R}_j(\Delta t) > \;=\; 2\mathbf{D}_{ij}^0 \Delta t. \tag{7.26}$$

To determine the components of these vectors without inverting Eq. (7.23), we should proceed in the following way (108; 109): let $\mathbf{R}$ denote the $3N \times 1$ column vector obtained by stacking the N $\mathbf{R}_i$ column vectors (3×1) on top of each other. Then we can write

$$\mathbf{R} = \sigma \cdot \mathbf{X} \tag{7.27}$$

where σ is a configuration dependent $3N \times 3N$ matrix and $\mathbf{X}$ is a $3N \times 1$ column vector of normally distributed Gaussian random numbers

$$< X_m > \;=\; 0 \tag{7.28}$$

$$< X_m X_n > \;=\; 2\delta_{mn}\Delta t \tag{7.29}$$

obtained from a random number generator. If we let $\mathbf{Q}$ denote the symmetric $3N \times 3N$ supermatrix constructed form the $\mathbf{D}_{ij}$ matrices in the following manner

$$\mathbf{Q} = \begin{pmatrix} \mathbf{D}_{11} & \mathbf{D}_{12} & \ldots & \mathbf{D}_{1N} \\ \mathbf{D}_{21} & \mathbf{D}_{22} & \ldots & \mathbf{D}_{2N} \\ \ldots & \ldots & \ldots & \ldots \\ \mathbf{D}_{N1} & \mathbf{D}_{N2} & \ldots & \mathbf{D}_{NN} \end{pmatrix}$$

then the elements of σ are simply given by

$$\sigma_{mm} \;=\; \left(Q_{mm} - \sum_{k=1}^{m-1} \sigma_{mk}^2 \right)^{1/2} \tag{7.30}$$

$$\sigma_{mn} \;=\; \frac{\left(Q_{mn} - \sum_{k=1}^{n-1} \sigma_{mk}\sigma_{nk} \right)}{\sigma_{nn}}. \tag{7.31}$$

7.3 Appendix C: Feynman's Brownian Ratchet

Feynman imagined a box full of gas that encloses an axle with vanes on it. Thermal motion of the gas molecules results in random bombardment of the vanes, causing the axle to turn in a jiggly way in both directions. Next, he imagined to hook the axle up to a toothed wheel, a ratchet, that can turn freely in one direction but whose backward rotation is prevented by a pawl on a spring that catches on the asymmetric teeth (Fig. 7.1). Now, when the axle tries to jiggle in one direction, the direction permitted by the ratchet, it turns freely, but when it tries to jiggle in the other direction, it is stopped. Step by step, the axle turns only one way, even though the thermal motion of the gas is random and undirected. In this way, thermal motion of the gas molecules in the box could be used to generate useful work such as lifting a weight attached to the axle, a clear violation of the second law of thermodynamics.

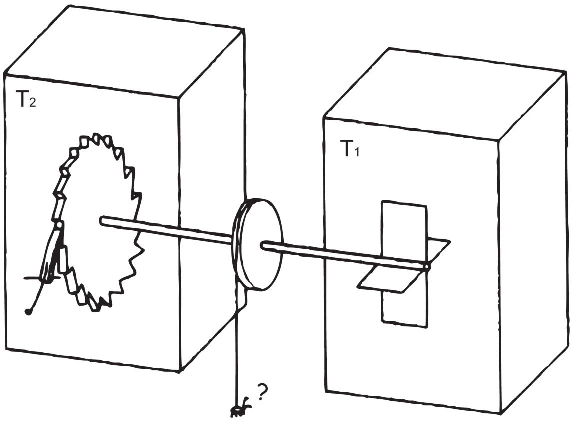

Figure 7.1: The Feynman's Brownian Ratchet

Of course the machine does not actually work under these conditions. The trick lies in ignoring the fact that thermal motion affects all parts of the system, the ratchet and pawl as well as the vanes. At a temperature where collisions with the vanes are sufficiently energetic to turn the ratchet step by step, the pawl is also jiggling around, and every so often the pawl will bounce out of its nook, allowing the ratchet to rotate backwards. If everything is at the same temperature, the number of forward steps will be balanced on average by the number of backward slips. But, Feynman's machine will work to turn primarily in one direction if the vanes and the ratchet are at different temperatures. If the vanes are hotter than the ratchet and pawl, the machine will turn forward and could indeed lift a weight, transducing the energy stored in the temperature gradient into mechanical force. If the ratchet and pawl are hotter than the vanes, the machine will turn backwards, but can still generate force. Feynman's example was designed to demonstrate that geometrical asymmetry, no matter how cleverly devised, cannot be used to generate force from thermal motion in the absence of an external source of energy (here, the external energy source is used to maintain the temperature gradient). But if such an external energy source is available, random thermal motion can be harnessed for unidirectional motion.

Bibliography

[1] M. R. Brown, Jr. *Journal of Plymer Science*, 42:487–495, 2004.

[2] B. G. Ranby. *Acta Chem. Scand.*, 6:128, 1952.

[3] S. Kuga and Jr. M. R. Brown. *Carbohydrate Res.*, 180:345, 1988.

[4] Helbert W. Amai T. Sugiyama J. Koyama, M. and B. Henrissat. *Proc. Natl. Acad. Sci. USA*, 94:9091, 1997.

[5] R. Atalla and D. L. VanderHart. *Science*, 223:283–285, 1984.

[6] Sugiyama J. Wada, M. and T. Okano. *J. App. Polymer Sci.*, 49:1491, 1993.

[7] Persson J. Sugiyama, J. and H. Chanzy. *Macromolecules*, 24:2461–2466, 1991.

[8] S. Kimura and T. Itoh. *Protoplasma*, 194:151, 1996.

[9] Takagi S. Kuga, S. and M. R. Brown Jr. *Polymer*, 34:3293–3297, 1993.

[10] Togawa E. Kondo, T. and Jr. M. B. Brown. *Biomacromolecules*, 2:1324–1330, 2001.

[11] M. Benziman, C. H. Haigler, R. M. Brown Jr., A. R. White, and K. M. Cooper. *Proc. Natl. Acad. Sci. USA*, 77:6678–6682, 1980.

[12] Brown R. M. Jr. Haigler, C. H. and M. Benziman. *Science*, 210:903, 1980.

[13] S. K. Cousins and R. M. Brown Jr. *Polymer*, 36:3885–3888, 1995.

[14] S. Cousins and Jr. M. R. Brown. *Polymer*, 38:903, 1997.

[15] R. D. Preston. *In Zimmerman M.H., ed. Formation of Wood in Forest Trees*, New York, Academic Press:169–188, 1964.

[16] S. C. Mueller and R. M. Brown Jr. *J. Cell Biol.*, 84:315–326, 1980.

[17] S. Kimura, W. Laosinchai, T. Itoh, K. Cui, C. R. Linder, and R. M. Brown Jr. *The Plant Cell*, 11:2075–2085, 1999.

[18] R. M. Brown Jr., J. H. M. Willison, and C. L. Richardson. *Proc. Natl. Acad. Sci. USA*, 73(12):4565–4569, 1976.

[19] Ohshima C . Hirose E . Nishikawa J . Itoh T . Kimura, S . *Protoplasma*, 216:71–74, 2001.

[20] H. Peng and L. Jaffe. *Planta*, 133:57–71, 1976.

[21] M. R. Jr. Brown. *Pure Appl. Chem.*, 10:1345–1373, 1996.

[22] D. P. Delmer. *Annu. Rev. Plant. Physiol. Plant. Mol. Biol.*, 50:245–276, 1999.

[23] I. Tsekos. *J.Phycol*, 35:635–655, 1999.

[24] J. H. M. Willison and Jr. M. R. Brown. *Planta*, 141:51–58, 1978.

[25] I. Tsekos and H. Reiss. *Protoplasma*, 169:57–67, 1992.

[26] R. M. Jr. Itoh, T. Brown. *Planta*, 160:372–381, 1984.

[27] S. Mizuta and R. M. Jr. Brown. *Protoplasma*, 166:187–199, 1992.

[28] Roberts E. M. Mizuta, S. and R. M. Jr. Brown. *Cellulose and wood: Chemistry and Technology, Wiley, New York*, ed. C. Schuerch:659–676, 1989.

[29] Brower D. L. Giddings, T. H. Jr. and L. A. Staehelin. *J. Cell. Biol.*, 84(2):327–339, 1980.

[30] C. R. Woese. *Microbiol. Rev.*, 51:221–271, 1987.

[31] Oyaizu Y. Oyaizu H. Olsen G. J. Yang, D. and C. R. Woese. *Proc. Natl. Acad. Sci. USA*, 82:4443, 1985.

[32] M. H. Deinema and L. P. T. M. Zevenhuizen. *Arch. Mikrobiol.*, 78:42–57, 1971.

[33] Mayer R. Ross, P. and M. Benziman. *Microbiol. Mol. Biol. Rev.*, 55:35–58, 1991.

[34] Rohde M. Bokranz W.and Ro Zogaj X., Nimtz M. *Mol. Microbiol.*, 39:1452–1463, 2001.

[35] E. Roberts. *Biosynthesis of cellulose II and related carbohydrates. PhD thesis.*, pages University of Texas, Austin, 1991.

[36] Fuller D. Iranfar N. Grimson M. J. Blanton, R. L. and W. F. Loomis. *Proc.Natl.Acad.Sci.USA*, 97:2391–2396, 2000.

[37] Haigler C. H. Grimson, M. J. and R. Blanton. *J. Cell. Science*, 109:3079–3087, 1996.

[38] S. Kimura and T. Itoh. *Cellulose*, 11:377–383, 2004.

[39] Jr. R. M. Brown. *Journal of Cell Science Suppl.*, 2:13–32, 1985.

[40] Kawagoe Y. Schreckengost W. E. Delmer D. P. Stalker D. M. Pear, J. R. *Proc. Natl. Acad. Sci. USA*, 93:12637–12642, 1996.

[41] T. Arioli, L. Peng, A.S. Betzner, J. Burn, W. Wittke, W. Herth, C. Camilleri, H. Höfte, J. Plazinski, R. Birch, A. Cork, J. Glover, J. Redmond, and R. E. Williamson. *Science*, 279:717–720, 1998.

[42] T.A. Richmond and C.R. Somerville. *Plant Physiol.*, 124:445–448, 2000.

[43] Somerville C. R. Turner, S. R. *Plant Cell*, 9:689–701, 1997.

[44] Scheible W. R. Cutler S. Somerville C. R. Taylor, N. G. and S. R. Turner. *Plant Cell*, 11:769–780, 1999.

[45] Howells R. M. Huttly A. K. Vickers K . Turner S. R. Taylor, N. G. *Proc. NAtl. Acad. Sci. USA*, 100:1450–1455, 2003.

[46] Mouille G. Robert, S. and H. Hofte. *Cellulose*, 11:351–364, 2004.

[47] Taylor N.G. Gardiner, J.C. and S.R. Turner. *Plant Cell*, 15:1740–1748, 2003.

[48] Eshed R. Richmond T. Delmer D. Scheible, W. R. and Somerville C. *Proc. Natl. Acad. Sci. USA*, 98:10079–10084, 2001.

[49] Kurek I. Jacob-Wilk D. Doblin, M. S. and D.P. Delmer. *Plant Cell Physiol.*, 43:1407–1420, 2002.

[50] A. M. C. Emons and A. M. C. Wolters-Arts. *Protoplasma*, 117:68–81, 1983.

[51] N. C. Carpita and D. M. Gibeaut. *Plant J.*, 3:1–30, 1993.

[52] M. C. McCann and K. Roberts. *J. Plant Sci.*, 96:323–334, 1990.

[53] A. Mogilner and G. Oster. *Curr. Biology*, 13:R721–R733, 2003.

[54] C. C. Peskin, G. M. Odell, and G. Oster. *Biophys. J.*, 65:316–324, 1993.

[55] A. Bowling and R. M. Brown Jr. 2005. http://www.botany.utexas.edu/facstaff/-facpages/mbrown/bowling/default2.html.

[56] A. M. C. Emons. *Planta*, 163:350–359, 1985.

[57] R. M. Brown Jr. *Pure Appl. Chem.*, 71:765–775, 1999.

[58] R. M. Brown Jr. and D. Montezinos. *Proc. Natl. Acad. Sci. USA*, 80:773–777, 1976.

[59] A. R. Paredez, C. R. Somerville, and D. W. Erhardt. *Science*, 312:1491, 2006.

[60] F. Jülicher, A. Ajadari, and J. Prost. *RPM Colloquia*, 69:1269–1281, 1997.

[61] I. B. Heath. *J. Theor. Biol.*, 48:445–449, 1974.

[62] P. K. Hepler and B. A. Palevitz. *Annu. Rev. Plant. Physiol.*, 25:309–362, 1974.

[63] W. Herth. *J. Cell Biol.*, 87:442–450, 1980.

[64] A. Mogliner and G. Oster. *Biophys. J.*, 71:3030, 1996.

[65] Leighton R. B. Feynman, R. P. and M. Sands. *The Feynman lectures on Physics, 1. USA*, Addison-Wesley:46.1–46.9, 1963.

[66] R.D. Astumian. *Science*, 276:917–922, 1997.

[67] T. L. Hill and M.W. Kirschner. *Int. Rev Cytol*, 78:1–125, 1982.

[68] A. M. C. Emons. In C. H. eds. Haigler and P. J. Weimer, editors, *Biosynthesis and Biodegradation of Cellulose*, pages 71–98. Marcel Dekker, New York, 1991.

[69] D. R. Daniels and M. S. Turner. *J. Chem. Phys*, 121:7401–7407, 2004.

[70] S. J. Eichhorn and R. J. Young. *Cellulose*, 8:197–207, 2001.

[71] C. H. Haigler and M. Benziman. *Cellulose and Other Natural Polymer Systems*, R.M.Brown Jr. ed., New York, Plenum Press:273–297, 1982.

[72] N. Hirai, S. Senobe, and T. Hayashi. *Proc. Natl. Acad. Sci. USA*, 95:15102–15106, 1998.

[73] S. A. Safran. *Statistical Thermodynamics of Surfaces, Interfaces, and Membranes*. Addison-Wesley, Reading MA, 1994.

[74] I. Derenyi, F. Jülicher, and J. Prost. *PRL*, 88:238101, 2002.

[75] G. C. Ruben and G. H. Bokelman. *Carbohydate Research*, 160:434–443, 1986.

[76] S. J. Hanley, J. F. Revol, L. Godbout, and D. G. Gray. *Cellulose*, 4:209–220, 1997.

[77] P. H. Raven, R. F. Evert, and S. E. Eichhorn. *Biology of Plants*. W. H. Freeman, New York, 6th edition, 1999. pp. 66-67.

[78] A. M. C. Emons and B. M. Mulder. *Proc. Natl. Acad. Sci. USA*, 95:7215–7219, 1997.

[79] T.I. Baskin. *Protoplasma*, 215:150–171, 2001.

[80] K. Roberts. The plant extracellular matrix. *Curr. Opinion Cell Biol.*, 5:1020–1027, 1989.

[81] A. M. C. Emons and B. M. Mulder. Plant cell wall architecture. *Comm. Theor. Biol.*, 4: 115–131, 1997.

[82] D. Reis, J. C. Roland, and B. Vian. Morphogenesis of twisted cell wall: chronology following an osmotic shock. *Protoplasma*, 126:36–46, 1985.

[83] A.C. Neville. *Biology of fibrous composites: Development beyond the cell membrane*. Cambridge University Press, 1993.

[84] Saxena I. M. Brown, Jr. R. M. and K. Kudlicka. *Trends in Plant Science*, 1:149–156, 1996.

[85] C Wymer and C Lloyd. Dynamic microtubules: implications for cell wall patterns. *Trends Plant Sci.*, 1:222–228, 1996.

[86] A. M. C. Emons, J. Derksen, and M. M. A. Sassen. *Physiol. Plant*, 84:486–493, 1992.

[87] A.M.C. Emons. Winding threads around plant cells: a geometrical model for microfibril deposition. *Plant Cell and Environment*, 17:3–14, 1994.

[88] B. M. Mulder and A. M. C. Emons. A dynamical model for plant cell wall deposition. *J. Math. Biol.*, 42:261–289, 2001.

[89] N. C. A. De Ruijter, M. B. Rook, T. Bisseling, and A. M. C. Emons. Lipochito-oligosaccharides re-initiate root hair tip growth in *vicia sativa* with high calcium and spectrin-like antigen at the tip. *Plant J.*, 13:341–350, 1999.

[90] H. R. Petty, R. G. Worth, and A. L. Kindzelskii. Imaging sustained dissipative patterns in the metabolism of individual living cells. *Phys. Rev. Lett.*, 84:2754–2757, 2000.

[91] A. M. C. Emons. *Acta Bot. Neerl.*, 37:31–38, 1988.

[92] A. J. Brown. *J. Chem. soc.*, 49:432–439, 1886.

[93] A. J. Brown. *J. Chem. soc.*, 51:643, 1887.

[94] Dutta D. and R. Gachhui. *Int J Syst Evol Microbiol*, 56:1899–1903, 2006.

[95] COUPERWHITE I. BERNARDO E. B., NEILAN B. A. *Syst. appl. microbiol.*, 21: 599–608, 1998.

[96] S. Schramm, M. Hestrin. *J. Gen. Microbiol.*, 11:123, 1954.

[97] Kjosbakken J. Valla, S. *ibid.*, 128:1401–1408, 1982.

[98] Cannon R. E. William W., S. *Appl. Env. Microbiol.*, 55:2448, 1989.

[99] Yamanaka S. Budhiono A. Iguchi, M. *J. Material Science*, 34:261–270, 2000.

[100] M. Benziman and H. Burger-Rachamimov. *J Bacteriol.*, 84:625–630, 1962.

[101] H. Weinhouse and M. Beriman. *Biochem. J.*, 138:537–542, 1974.

[102] White A. R. Brown M. B. Jr. Haigler, C. H. and K. M. Cooper. *J. Cell Biology*, 94: 64–69, 1982.

[103] Saito M. Kuga S. Shibazaki, H. and T. Okano. *Cellulose*.

[104] Tsuji M Hirai, A. and F. Horii. *Cellulose*, 9:105–113, 2002.

[105] G. K. Batchelor. *J. Fluid. Mech.*, 44:410, 1970.

[106] Julicher F. Camalet, S. *New Journal of Physics*, 24:1–23, 2000.

[107] Kruiskamp P. H. Vliegenthart J. F. G. Kroon Kroon-Batemburg, L. M. J. *J. Phys. Chem B*, 101:8454–8459, 1997.

[108] D. L. Ermak and J. A.. McAmmon. *J. Chem. Phys.*, 69(4):1352–1360, 1978.

[109] S.A. Allison and J. A. McAmmon. *Biopolymers*, 23:167–187, 1984.

[110] H. C. Ottinger. Stochastic processes in polymeric fluids. *Springler-Verlag*, New-York, 1996.

[111] M. Doi and S. F. Edwards. The theory of polymer dynamics. *Oxford Science Publications*, New-York, 1986.

[112] S. Rotne, J.and Prager. *J. Stat. Phys.*, 14:153, 1976.

Summary

This thesis deals with many different biological problems concerning cellulose biosynthesis. Cellulose is made by all plants, and therefore it is probably the most abundant organic compound on Earth. Aside from being the primary building material for plants, this biopolymer is of great economic importance globally because it is the major constituent of cotton (over 94%) and wood (over 50%). Moreover, according to how it is treated, cellulose can be used to make paper, film, explosives, and plastics, in addition to having many other industrial uses. The paper in this book, for example, contains cellulose, as do some of the clothes we are wearing.

In addition to higher plants, cellulose is synthesized by a number of bacterial species, algae, lower eukaryotes (tunicates), and the slime mold *Dictyostelium*. The function of cellulose in these different groups of organisms reflects the diverse role associated with this simple structural polysaccharide. Whereas it is possible for some organisms, specifically bacteria, to survive in absence of cellulose synthesis, it may not be true for most vascular plant cells. As such, the importance of cellulose in the life of a plant cannot be overemphasized since it not only provides the necessary strength to resist the turgor pressure in plant cells, but also has a distinct role in maintaining the size, shape and differentiation of most plant cells.

The aim of this thesis is to investigate, by mean of theoretical methods, coupled to simulation techniques, the polymerization, crystallization, and self-organization mechanism of this universal distributed polysaccharide, in different biological systems.

We start in Chapter 2 with a general description of the chemical and mechanical features of the cellulose microfibrils (CMFs), the crystalline form of cellulose in nature. After a brief overview on the biogenesis of the CMFs in the plant cells we proceed focusing on two of the most important cellulose producer entities: the plant cells and the Acetobacter cells.

The first part of the thesis, therefore, is concerned with all the aspects related to cellulose biosynthesis in the cell-wall of plant cells. We begin in Chapter 3 with a detailed investigation on the self-assembly mechanism of the Cellulose Synthase Complex (CSC) in higher plants, the hexagonal Rosette CSC: based on the known experimental evidences regarding the internal structure of this protein, we are able to build a theoretical scheme to characterize the interactions among the CSC subunits; then, by mean of a Monte Carlo algorithm, we implement this interaction scheme in a simulation that document step by step the formation of the hexagonal enzyme. Our model is able to explain the assembly of many types of CSCs, like the hexagonal Rosettes of plants as well as the linear CSCs present in bacteria and the clusters that form in the cell wall of some algae.

After having clarified the formation of the Rosette CSC structure, we shift our attention to its motion in the plasma membrane of plant cell. In Chapter 4 we present a biophysical model that unravels the force generating mechanism underlying the propulsion of the Rosette CSC: the model identifies polymerization and crystallization as driving forces, and elucidates the role of polymer flexibility and membrane elasticity as force transducers. On the basis of

our model and appropriate values for the relevant physical constants, we obtain a theoretical estimate for the velocity of the CSC that is in agreement with the experimental value. To have a proof a principle of the proposed mechanism, we have also developed a stochastic simulation that reproduces the movement of the Rosette CSC in the fluid membrane of the plant cell.

The last issue related to plant cells cellulose is the formulation of a mathematical model to analyze the building of cell wall architecture (Chapter 5). The highly regular textures observed in cell walls reflect the spatial organization of the cellulose CMFs. Based on a geometrical hypothesis proposed earlier, we formulate a model that describes the space-time evolution of the density of Rosette CSCs in the plasma membrane of plant cell. The trajectories of the Rosettes are assumed to be governed by an optimal packing constraint of the CMFs that couples the direction of motion to the density of the CSCs. Our model is based on a relatively small numbers of variables that can be tuned to obtain most of the cell wall textures that have been found experimentally. Moreover, we demonstrate that it is also robust against a number of perturbations and noise effects.

The second part of the thesis is focused on the cellulose-producing Acetobacter cells, which live at the air-liquid interface and which exhibit a peculiar motion during the cellulose polymerization process. The mechanism of formation as well as the structure of the bacterial cellulose has been studied extensively in recent decades. The cellulose product appears as a long ribbon, composed of many CMFs, which extends parallel to the longitudinal axis of the cell, and which is synthesized by a linear array of particles placed along the axis of the bacterial rod. Goal of this chapter (Chapter 6) is to correlate the peculiar motion of Acetobacter with an hydrodynamic effect caused by the interactions between the cellulose CMFs and the fluid in which they are immersed. To further assess the correctness of our model, in the last part of the thesis we implement a Brownian Dynamics simulation that is able to reproduce the main features of this particular bacterial motion.

Samenvatting

Dit proefschrift behandelt verschillende biologische aspecten van de biosynthese van cellulose. Cellulose wordt door alle planten gemaakt en is daardoor waarschijnlijk het meest voorkomende organische polymeer op aarde. Naast een van de belangrijkste bouwstoffen van planten, is dit polymeer ook wereldwijd van groot economisch belang omdat het een belangrijke component van katoen (meer dan 94%) en van hout (meer dan 50%) is. Bovendien kan cellulose, afhankelijk van hoe het behandeld wordt, gebruikt worden voor het maken van papier, film, explosieven en plastics, naast nog veel andere industriÃ«le toepassingen. Het papier waarop dit boek gedrukt is, en veel van de kleren die wij dragen, bevatten dan ook veel cellulose.

Naast de hogere planten, produceren ook enkele bacteriesoorten, algen, lagere eukaryoten zoals tunicaten en de slijmschimmel Dictyostelium cellulose. De uiteenlopende functies van cellulose in deze verschillende groepen van organismen, geeft de de heel verschillende rollen aan die dit simpele structurele polysaccheride kan spelen. Daar waar sommige organismen echter kunnen overleven zonder cellulose te produceren, geldt dit niet voor de vaatplanten. Als zodanig kan de rol van cellulose voor het leven van planten dan ook niet overschat worden, aangezien het de benodigde mechanische sterkte levert, die het mogelijk maakt dat plantencellen de turgordruk weerstaan, en bovendien een belangrijke rol speelt bij het bepalen van de vorm, de omvang en de differentiatie van van de meeste plantencellen.

Het doel van dit proefschrift is om met behulp van theoretische beschouwingen gekoppeld aan computersimulaties de polymerisatie, de kristallisatie en de zelforganisatie principes van dit zo universeel verbreide polysacchride te onderzoeken in verschillende biologische systemen.

We starten in hoofdstuk 2 met een algemene beschrijving van de chemische en mechanische eigenschappen van Cellulose Microfibrillen (CMFs), de kristallijne vorm waarin het in de natuur voorkomt. Na een kort overzicht van de biogenese van de CMFs, richten wij ons op de twee meest prominente cellulose producerende organismen, planten en Acetobacter bacteriÃ«n.

Het eerste deel van het proefschrift gaat daarom over alle aspecten van de biosynthese van cellulose in de celwanden van planten. We starten in hoofdstuk 3 met een gedetailleerde beschrijving van het zelfassemblage proces van het Cellulose Synthase Complex (CSC) in hogere planten, het hexagonale eiwitcomplex dat ook wel “Rosette” wordt genoemd. Gebaseerd op de bestaande experimentele aanwijzingen omtrent de interne structuur van dit eiwitcomplex, zijn we in staat een theoretisch model op te stellen voor de interacties tussen de subeenheden van het CSC. Vervolgens implementeren we deze interacties in een Monte Carlo simulatie, die de stap voor stap assemblage van het hexagonale enzymcomplex in beeld brengt. Ons model is in staat om de constructie van veel verschillende types van CSCs te beschrijven, niet alleen de hexagonale Rosettes zoals die in planten worden gevonden, maar ook the lineaire CSCs van sommige bacteriesoorten en de clusters zoals die in de celwand van sommige algen voorkomen.

Na de vorming van de structuur van het Rosette CSC te hebben opgehelderd, richten wij ons op zijn beweging in het plasmamembraan van de cel. In hoofdstuk 4 presenteren wij een biofysisch model dat het krachten productie mechanisme dat ten grondslag ligt aan de voortstuwing van het Rosette CSC ontrafelt. Het model identificeert de polymerisatie en de kristallisatie van de cellulose as drijvende krachten, en geeft opheldering over de rol van polymeerflexibiliteit en membraan elasticiteit in het overbrengen van deze krachten. Op basis van ons model en de waarden van de relevante fysische constanten geven wij een schatting van de snelheid van het CSC die in goede overeenstemming is met de experimentele waarde. Om het principe achter ons model verder te testen, ontwikkelden we een stochastische simulatie die de beweging van het CSC in het membraan van de plantencel reproduceert.

Het laatste thema rond cellulose in planten cellen, is een mathematisch model voor het beschrijven van de bouw van de architectuur van planten celwanden (hoofdstuk 5). De zeer regelmatige texturen van planten celwanden, reflecteert de ruimtelijke organisatie van de CMFs. Gebaseerd op een eerder geformuleerde geometrische hypothese, stellen wij een model op dat de ruimte-tijd evolutie van de dichtheid van Rosette CSCs in het plasmamembraan beschrijft. De baenen van de CSCs worden bepaald door een optimale pakkingvoorwaarde die de bewegingsrichting koppelt aan de dichtheid van de CSCs. Het model heeft slechts een beperkt aantal parameters, die zo gekozen kunnen worden dat de meest van de experimenteel gevonden celwand texturen gereproduceerd worden. We laten bovendien zien dat het model robuust is tegen een aantal verstoringen en de effecten van ruis.

Het tweede deel van het proefschrift richt zich op de cellulose producerende Acebacter cellen, bacteriÃ«n die leven aan het lucht-water grensvlak en die een merkwaardige beweging vertonen gedurende het cellulose polymerisatieproces. Het vormingsproces en de structuur van is intensief bestudeerd de afgelopen decennia. Het cellulose product verschijnt als een langgerekt lint, samengesteld uit vele CMFs, dat zich strekt in de richting parallel aan de lange as van de cel, en dat gesynthetiseerd wordt door een lineaire reeks van deeltjes langs de as van de staafvormige bacterie. Het doel van hoofdstuk 6 is om het bewegingsmechanisme van Acetobacter in verband te brengen met een hydrodynamisch effect dat ontstaat door de wisselwerking van de CMFs en het vloeibare medium waarin zij ondergedompeld zijn. Om de juistheid van dit principe te testen, implementeren wij in het laatste deel van het proefschrift een Brownse Dynamica simulatie, die in staat blijkt de voornaamste kenmerken van deze aparte vorm van bacteriÃ«le voortbeweging te reproduceren.

List of Publications

The work in this thesis covers the following pubblications:

Chapter 5:
The Cellulose Synthase Complex: a polymerization driven supramolecular motor
(Biophys J. 2007 Apr 15;92(8):2666-73.)
Diotallevi F., Mulder, B.

Chapter 4:
The dynamics of interacting comoving CMF synthases,
(in preparation)
Diotallevi F., Mulder, B.

Chapter 6:
Hydrodynamic buckling drives the motion of A. Xylinum,
(in preparation)
Diotallevi F., Mulder, B., Joanny, J.F.

Chapter 3:
A model for the assembly of the CSC in plant cells,
(in preparation)
Diotallevi F., Mulder, B.

Other pubblications:

Capillary filling using Lattice Boltzmann Equations: the case of multi-phase flows ,
(submitted to EPJ)
F. Diotallevi, L. Biferale, S. Chibbaro, A. Lamura G. Pontrelli, M. Sbragaglia, S. Succi, F. Toschi

Fluid-like behavior of a one-dimensional granular gas,
(J. Chem. Phys. 120(1) 35 (2004))
F. Diotallevi, U. Marini Bettolo Marconi, A. Puglisi, F. Cecconi

Inelastic hard-rods in a periodic potential,
(J. Chem. Phys. 121, 5125 (2004))
F. Diotallevi, U. Marini Bettolo Marconi, A. Puglisi, F. Cecconi

Note added in proof

We are grateful to a member of the reading committee,prof. dr. R. M. Brown Jr, an acknowledged world expert on cellulose, who has alerted us to a number of omissions of literature citations in the text as well as references to figures used from the literature in the thesis. Unfortunately, for technical reasons we were not able to redress these in time for submission. We apologize to any readers that justifiably feel that we have not been comprehensive enough in our referencing and figure attributions, and we assure them that we will address these issues as fully as possible in future publications.

Acknowledgments

This work would not have been possible without the help and support of a number of people, whom I wish to thank.

First and most of all I want to thank my promotor Bela Mulder, who introduced me to the rich and surprising world of cellulose. Besides being a careful and helpful supervisor, Bela has always been patient and tolerant, giving me the possibility to enrich my knowledge on this research subject by mean of various collaborations with different groups and people in many countries.

I also want to express my thanks to Anne Mie Emons, with whom I had the pleasure to work especially during the initial stage of my PhD. I am grateful to Anne Mie for her helpful advices and suggestions, and for her kind answers to my numerous questions regarding plant biology.

Together with Bela, Daan Frenkel has been my other guiding light: with his deep knowledge and brilliant ideas Daan was able to find solutions to the most tricky problems, offering me his support on innumerable circumstances.

I thank Jean Francois Joanny for allowing me to stay for three months in his lab in Paris: the collaboration with Jean Francois was very useful, and decisive for the work on Acetobacter presented in Chapter 6.

My thanks also go to Giovanni Ciccotti, that hosted me in Rome and taught me all I know about MD simulations of polymers in solvent. I hope that the fruit of our collaboration will see the light in a very soon future.

I thank all the Amolfers, especially the "Overloopers", for the interesting discussions that have been a continuous source of ideas and enthusiasm.

I also give my thanks to Sauro Succi and Luca Biferale, who kindly allowed me to work on this thesis during the first months of my new job.

Finally, I would like to thank a number of other people that were not directly involved in the work presented in this Thesis.

First, all my friends spread around the world: Netherlands and Italy, England and France, Spain and US and many more countries... It would be impossible to mention all of you (I'm sorry for that!), but I'm sure that you know how much you mean and have meant to me, especially during these years abroad, and how important your presence has been in my dark days.

Un grazie enorme va alla mia famiglia, che ha (da sempre...) accettato e supportato ogni mia decisione, per quanto folle la potesse trovare. Un grazie particolare va ai miei nonni e alle mie nonne, a cui non smetto mai di pensare e a cui questa tesi è dedicata.

Much more than a thank you goes to Andrea, who has always been by my side despite thousands of kilometres were keeping us apart: mi hai lasciato partire senza mai lasciarmi sola, non lo dimentichero' mai.

The work described in this thesis was performed at the FOM Institute for Atomic and Molecular Physics, Kruislaan 407, 1098 SJ, Amsterdam, The Netherlands. The work is part of the research program of the Stichting voor Fundamenteel Onderzoek der Materie (FOM) and was made possible by financial support from the Nederlandse Organisatie voor Wetenschappelijk Onderzoek (NWO).

Cover: Revised Ernst Haeckel's interpretation of several Tunicates (Ascidians), the only animals able to synthesize cellulose. From Kunstformen der Natur (Artforms of Nature), 1904.

“In Olanda... non capisco
non mi sento soddisfatto
sara’ che e’ tutto cosi’ dritto
cosi’ spietatamente piatto...”

Banalita’, Daniele Silvestri

Education Statement of the Graduate School
Experimental Plant Sciences

The Graduate School
EXPERIMENTAL
PLANT
SCIENCES

Issued to: **Fabiana Diotallevi**
Date: **26 October 2007**
Group: **Theory of Biomolecular Matter (AMOLF Institute) &**
Plant Cell Biology, Wageningen University

1) Start-up phase	*date*
► **First presentation of your project**	
Oral presentation: “Understanding Cellulose Biosynthesis”, AMOLF institute	Sep 2003
► **Writing or rewriting a project proposal**	
► **Writing a review or book chapter**	
► **MSc courses**	
Molsim- Simulation Course (Amsterdam)	Jun 2003
► **Laboratory use of isotopes**	
Subtotal Start-up Phase	*5.5 credits**

2) Scientific Exposure	*date*
► **EPS PhD student days**	
EPS PhD Student Day, Wageningen University	19 Sep 2006
► **EPS theme symposia**	
EPS Theme 1 sympsium 'Developmental Biology of Plants' , Wageningen University	26 Apr 2005
EPS Theme 1 sympsium 'Developmental Biology of Plants' , Leiden University	12 May 2006
► **NWO Lunteren days and other National Platforms**	
NWO meetings Lunteren Biophysics (4x2 days)	2003-2006
Lunteren Statistical Mechanics (2x2 days)	2003-2005
KNAW and NWO Biophysics Meetings (4x1 day)	2003-2006
► **Seminars (series), workshops and symposia**	
Biolateral Triangle Meeting, Dresden, Germany (2 days)	18-19 Nov 2004
Biolateral Triangle Meeting, Amsterdam, Netherlands (2 days)	1-2 Dec 2005
Biolateral Triangle Meeting, Paris, France (2 days)	Jan 2007
► **Seminar plus**	
► **International symposia and congresses**	
Soft Condensed Matter Physics- NATO, Edinburgh, UK (9 days)	29 Mar-8 Apr 2004
Julich Soft Matter Days, Bonn, Germany (4 days)	1-4 Nov 2005
Sitges Conference, Barcelona, Spain (5 days)	5-9 Jun 2006
StatPhys Conference, Genova, Italy (5 days)	9-13 Jul 2007
► **Presentations**	
Biolateral Triangle Meeting, Dresden, Germany	2004
EPS- Theme Symposia	2005
Lunteren Poster Session (3x)	2003-2005
Sitges Conference, Poster session	2006
► **IAB interview**	19 Sep 2006
► **Excursions**	
Subtotal Scientific Exposure	*19.3 credits**

3) In-Depth Studies	*date*
► **EPS courses or other PhD courses**	
VU-Amolf Complex System Summerschool (4x4days)	2003-2006
► **Journal club**	
Journal Club “Life Inspired Physics Group”	2003-2007
► **Individual research training**	
Subtotal In-Depth Studies	*7.8 credits**

4) Personal development	*date*
► **Skill training courses**	
Writing structural English	2004
Writing Scientific English	2006
► **Organisation of PhD students day, course or conference**	
► **Membership of Board, Committee or PhD council**	
Subtotal Personal Development	*1.8 credits**

TOTAL NUMBER OF CREDIT POINTS*	**34.4**

Herewith the Graduate School declares that the PhD candidate has complied with the educational requirements set by the Educational Committee of EPS which comprises of a minimum total of 30 credits

** A credit represents a normative study load of 28 hours of study*